Quantum Metrology for Enhanced Gravitational-Wave Detection

Thesis by
Rajashik Tarafder

In Partial Fulfillment of the Requirements for the
Degree of
Doctor of Philosophy

CALIFORNIA INSTITUTE OF TECHNOLOGY
Pasadena, California

2025
Defended May 27, 2025

Rajashik Tarafder
ORCID: 0000-0002-5994-3105

ACKNOWLEDGEMENTS

While it's hard to gauge the impact of everyone who played a role during my PhD, none would be greater than that of my advisor, Yanbei Chen. I would like to thank him for providing support and having faith in me during the toughest periods of the program, and for creating a space that allowed me to grow. Along with Yanbei, I would also like to thank my collaborators Tuvia Gefen and Rana Adhikari, whose understanding of physics shaped my own and provided me with a benchmark to aim for.

Additionally, mentors like Bedabrata Pain not only helped me develop a scientific approach but also offered a home away from home. Also, I am grateful to Graeme Smith for his guidance during crucial periods of the program. Further, I am grateful to my committee members, Lee McCuller and Nick Hutzler, who provided insight that shaped my research. I want to acknowledge the support I have received from the Mirmira Dwarkanath Fellowship, LIGO Laboratory, and Theoretical AstroPhysics Including Relativity (TAPIR) at various stages of the program.

I would also like to thank my fellow doctoral students, James Gardner and Su Direkci, who inspire me with their passion and intellect every day. I also want to thank my friends Leo Borell and Adriano Testa, who helped me explore the fun side of things during my time at Caltech.

Aside from academics, my most cherished moments at Caltech were with my students for the courses I TA-ed. This is what I will miss most. In particular, I would like to thank Tal Einav and Ashmeet Singh, who taught me how to teach and continue to amaze me with their abilities. Additionally, I would like to thank David Hsieh for all his support in this process. I am inspired by how the students benefited from his style of teaching and thoroughly enjoyed acting as his TA.

During my time in SoCal, I also gained a surrogate family — Prerna, Benny, Rahila, and Rumela, whose faith and camaraderies beyond academics I will always cherish.

I would also like to thank my parents, who started this story with an obstinate attempt to create a life of intellect and thought for me. They knew it long before I did that I would be on this path someday. This faith was more than resonated by Rita Agrawal, Stuti, and Yogyam, whose belief I strive to meet daily.

But most of all, I am eternally grateful to my wife Sristy, who witnessed my most difficult moments and stood by me in all of them. Her advice, encouragement, and love have defined every moment of the last eleven years I have known her. But even more than that, she is an inspiration and the paragon of my aspirations.

ABSTRACT

Current ground-based gravitational wave detectors are reaching sensitivity limits imposed by quantum, thermal, seismic, and Newtonian noise, motivating the development of novel techniques to surpass these fundamental barriers. This thesis investigates two complementary approaches to enhance interferometric gravitational wave astronomy: displacement-noise-free interferometry (DFI) and real-time waveform estimation via Kalman filtering.

First, we introduce a resonant triangular-cavity topology that, by exploiting redundant readout channels, isolates phase shifts induced by gravitational waves from mirror displacement noise. Within an input–output formalism, we define the displacement-free subspace as the null space of the mirror-noise transfer matrix and demonstrate that this configuration retains finite quantum Fisher information even in the limit of arbitrarily large mirror motion. Incorporating realistic thermal and radiation-pressure noise models, we derive optimal homodyne detection angles, characterize pseudo-displacement-free modes over finite bandwidths, and quantify the effect of injected squeezing. Extensions to n-gon cavity networks further establish the versatility and practical feasibility of the DFI paradigm.

Second, we cast the readout of detuned interferometers as a multi-parameter estimation problem, where gravitational-wave signals couple amplitude and phase quadratures. To recover the quantum Cramér–Rao bound for a chosen quadrature, we design Bayesian filters-specifically Extended and Unscented Kalman Filters-that treat the orthogonal quadrature as an effective disturbance. Numerical simulations under realistic signal-to-noise conditions reveal that these filters attain the optimal bound for amplitude estimation while providing reliable uncertainty quantification, matching the performance of particle-filter approaches at a fraction of the computational cost.

By combining architectural immunity to displacement noise with algorithmic optimality in waveform extraction, this work lays a foundation for quantum-enhanced, broadband gravitational wave observatories. The results inform near-term upgrades and guide the conceptual design of third-generation detectors (e.g., Einstein Telescope, Cosmic Explorer), where mitigating low-frequency environmental noise and delivering real-time signal processing are critical.

PUBLISHED CONTENT AND CONTRIBUTIONS

Chapters in this thesis reproduce results and content from the publications listed below.

[1] Tuvia Gefen, Rajashik Tarafder, Rana X. Adhikari, and Yanbei Chen. Quantum precision limits of displacement noise-free interferometers. *Phys. Rev. Lett.*, 132:020801, Jan 2024. doi: 10.1103/PhysRevLett.132.020801. URL https://link.aps.org/doi/10.1103/PhysRevLett.132.020801. R.T. participated in formulating the theory, developing the code, and writing the manuscript.

TABLE OF CONTENTS

Acknowledgements . . . iii
Abstract . . . v
Published Content and Contributions . . . vi
Table of Contents . . . vi
List of Illustrations . . . ix
Chapter I: Introduction . . . 1
1.1 Gravitational Wave Detection: Historical Context . . . 2
1.2 Quantum Metrology and Gravitational-Wave Astronomy . . . 3
1.3 Noise Sources in Gravitational-Wave Interferometers . . . 5
1.4 Displacement-Noise Free Interferometry (DFI) . . . 9
1.5 Signal Readout and Estimation in Interferometers . . . 11
1.6 Towards Quantum-Enhanced Broadband Detectors . . . 13
1.7 Thesis Outline . . . 14
Chapter II: Displacement-Noise Free Interferometers . . . 16
2.1 Introduction . . . 16
2.2 Formalism and Model . . . 17
2.3 Quantum Precision Limits . . . 19
2.4 Precision Limits of the Simplified Model . . . 20
2.5 Precision Limits with Realistic Noise Profiles . . . 21
2.6 Effect of Squeezing . . . 25
2.7 Extensions and Conclusions . . . 25
Chapter III: Linear Waveform Estimation Using Kalman Filters . . . 27
3.1 Introduction . . . 27
3.2 Theory . . . 28
3.3 Filtering Approach . . . 30
3.4 Numerical Simulations . . . 33
3.5 Conclusions . . . 34
Appendix A: Supplemental Material for Displacement-Noise Free Interferometers . . . 39
A.1 Two-Photon Formalism . . . 39
A.2 Quantum Fisher Information Matrix . . . 40
A.3 Fisher Information with Homodyne Measurement . . . 45
A.4 Optimal Measurement Basis . . . 46
A.5 QFI with Thermal Displacement Noise . . . 48
A.6 FI and QFI with Radiation Pressure . . . 50
A.7 FI and QFI with Radiation Pressure and Thermal Displacement Noise 55
A.8 Effect of Squeezing . . . 57
A.9 Extensions . . . 62
A.10Newtonian and Seismic Noise . . . 64

A.11Calculation Outline 64
A.12GW response: Analytical Expressions of Transfer Matrix $\mathcal{V}$ 67
A.13Displacement Response: Analytical Expression of Transfer Matrix A 70
A.14Sagnac Effect 71
A.15Comparison with Standard Sagnac Interferometers 73
Appendix B: Supplementary Material for Waveform Estimation Using Kalman Filters 75
B.1 Two-Photon Formalism for the Signal Susceptibility 75
B.2 Normalization of Quadrature Operators for Finite Integration Time . 76
B.3 Heterodyne Readout For Seeding Filters 78
B.4 Optimal Quadratures for Measuring $|h|$ 79
B.5 Construction of a Commutating Pair to the Optimal Measurement . . 81
B.6 Quantum Fisher Information and Ultimate QCRB 81
B.7 Extended Kalman Filter for Amplitude and Phase Estimation 82
B.8 Unscented Kalman Filter for Amplitude and Phase Estimation 88
B.9 Particle Filtering 90
Bibliography 93

LIST OF ILLUSTRATIONS

Number *Page*

2.1 Sketch of the DFI scheme: a symmetric triangular cavity is formed by three mirrors and six input laser fields. Six detectors are placed in the opposite direction of the input fields. The configuration leads to both a clockwise and an anti-clockwise circulating field within the cavity. We used the following parameters: Arm length: L = 4km, Laser wavelength: 1064 nm (same as advanced LIGO [1]). Mirrors mass: 5 kg, Intracavity Power: 3.5MW (to enhance RPN for illustrations). Power transmissivity of the mirrors: $T = 0.1$. 18

2.2 Quantum precision limits with varied noise sources. (a) Precision limits with the simplified model: The SD, σ, as a function of frequency for different levels of displacement noise (δ) (eq. (2.6)). The DFI property is manifested in the fact that σ is finite in the limit of infinite displacement noise (solid black curve). (b) Precision limits with realistic noise profiles. Given RPN alone, by measuring the optimal quadratures (eq. (2.10)) the QFI (black dashed line) coincides with the shot noise limit (solid yellow line). On the other hand, measuring the (non-optimal) phase quadratures, yields the solid blue (circles) line (eq. (2.11)). Similarly, given both RPN and thermal noise, measuring the phase quadratures yields the solid red (rectangles) line. Inset: Comparison between the phase quadratures FI (solid red line) and the QFI (black dashed line) in the presence of thermal noise and RPN. 22

2.3 Effect of squeezing. (a) Performance with squeezing in the simplified model: Dashed lines correspond to SD (σ) with squeezing and solid lines to unsqueezed. For white displacement noise, squeezing becomes not effective at lower frequencies as can be also observed from the plot of η in the inset. (b) Performance with squeezing given thermal noise and RPN: The solid (dashed) line corresponds to unsqueezed (optimally squeezed) SD with phase quadratures measurement. Inset: η_{gain} (red dots) and η (green line) as a function of frequency. (c) The SD with optimal squeezed input and optimal measurement (blue curve, circles) compared to the SD with the same squeezed input but a readout combination that maximizes the signal (red curve, squares). 23

3.1 Filter performance with varied time steps. Top row: Estimated uncertainty $\Delta|h|/|h|$ predicted by each filter as a function of measurement SNR (in dB) for the extended Kalman filter (EKF, left), unscented Kalman filter (UKF, center), and particle filter (PF, right). Colored curves correspond to integration intervals of T (blue), $10T$ (green), and $100T$ (magenta), while the black dotted line shows the optimal single-parameter homodyne limit and the grey dash–dotted line the heterodyne baseline.Bottom row: Empirical RMSE under the same conditions and for the same integration times and benchmarks. All filters approach the homodyne bound at high SNR; shorter integration times yield larger fluctuations around the optimal noise level but enable more rapid convergence to the ultimate sensitivity. Curves are averaged over 10^6 Monte Carlo samples. 35

3.2 Comparison of each filter's internal estimated uncertainty (solid colored lines) against its empirical RMSE (dashed colored lines) as a function of measurement SNR (in dB), shown separately for the extended Kalman filter (EKF, top panel) and unscented Kalman filter (UKF, bottom panel). Also plotted are the heterodyne readout baseline (grey dash–dotted), the single-parameter QCRB (solid black), and the particle-filter benchmark (gold dotted). The near-perfect overlap between estimated noise, empirical RMSE, and the PF benchmark demonstrates that both EKF and UKF not only accurately quantify their own error but also saturate the optimal performance of the particle filter across the entire SNR range. Results are averaged over 10^6 Monte Carlo trials. 36

3.3 Normalized RMSE in the amplitude $|h|$ (left) and phase ϕ (right) of the gravitational-wave signal as a function of measurement SNR (in dB). Curves show the performance of the extended Kalman filter (EKF, orange dash–dotted), unscented Kalman filter (UKF, blue dotted), particle filter (PF, yellow dashed), the heterodyne readout baseline (grey dash–dotted), and the single-parameter QCRB (solid black). Results are averaged over 10^6 Monte Carlo samples. All filters asymptotically attain the amplitude QCRB at high SNR, while phase estimation remains significantly above its QCRB across the entire SNR range. 37

A.1 Sensitivity profile with RPN for different measurement bases. The QFI corresponds to optimal measurement (solid orange line) and saturates the shot noise limit (black dashed line). The solid blue line corresponds to phase quadratures measurement (and thus optimal combination of phase quadratures) and the dashed red line to the max-signal combination of phase quadratures, i.e., a combination that is optimal given only shot noise. 54

A.2 Sensitivity profile that corresponds to phase quadratures measurement (F) along with $F_{\max}$ (blue dots), $F_{\min}$ (green triangles), and F_{DFS} (brown squares), as defined in the text. As shown in the text $F = F_{\max} + F_{\min} + F_{\mathrm{DFS}}$. 55

A.3 Sensitivity profile given thermal noise, with and without radiation pressure. (a) QFI: QFI with both thermal noise and RPN (red, solid line) coincides with QFI given only thermal noise (green diamonds). Blue dashed line corresponds to the shot noise limit. (b) FI with phase quadrature measurement: red solid line corresponds to both thermal and RPN, green diamonds to only thermal noise and blue, dashed line to shot noise limit. 56

A.4 Similar to fig. A.2 given thermal displacement noise and RPN with phase quadratures measurement. Three different regimes of the FI: the solid red line correspond to F, the blue dots to $F_{\max}$, green triangles to $F_{\min}$ and brown squares to F_{DFS}. The different FI's coincide with total FI in three different regimes. 58

A.5 SD with optimal measurement (brown) and phase quadratures measurement (green). The solid lines correspond to the unsqueezed case and the dashed to optimal squeezing. In this illustration $r = 1.5$. . . 62

A.6 Extensions of the DFI scheme. (a) Extensions of the DFI triangular scheme to an arbitrary n-gon. The vertices represent the mirrors and the blue edges represent the light trajectories. (b) Comparison between the sensitivities of the different n-gon schemes: dashed lines correspond to shot-noise only and solid lines to thermal displacement noise as well. The blue, red and gray lines correspond to $n = 3, 5, 9$, respectively. 63

A.7 Sagnac Effect. Left: sensitivity profiles with *white infinite* displacement and Sagnac noises. The bottom green (solid) line corresponds to the shot noise limit. The top yellow (solid) line corresponds to both infinite displacement and Sagnac noises. The dashed gray (top) and black (bottom) lines correspond to displacement and Sagnac noise only, respectively. Right: Comparison between thermal noise only (dashed, grey line) and thermal noise with infinite Sagnac noise (yellow, solid curve). The Sagnac noise almost does not change the sensitivity profile; its effect becomes non-negligible only in the limit of very poor sensitivity. 71

A.8 Comparison of DFI and Sagnac Interferometers. (a) Top: our symmetric DFI interferometer, bottom: standard triangular Sagnac interferometer, where only one port is open. (b) Sensitivity comparison between the standard triangular Sagnac and the symmetric DFI given phase quadratures measurement and realistic noise profile (RPN and thermal noise). (c) Sensitivity comparison, at low frequencies, between different transmissivity configurations, illustrating the optimality of the symmetric DFI. 74

Chapter 1

INTRODUCTION

Gravitational waves, ripples in the fabric of spacetime produced by accelerating massive objects, were first predicted by Albert Einstein in 1916 as a consequence of General Relativity. Detecting these waves directly, however, proved to be an immense scientific and technological challenge due to the incredibly small strain they induce on detectors (on the order of 10^{-21} or less) [2]. Early experimental efforts in the 1960s, notably the resonant bar detectors of Joseph Weber, claimed tentative detections but could not be confirmed. Indirect evidence for gravitational waves emerged in the 1970s with the observation of the Hulse-Taylor binary pulsar, whose orbital decay matched the energy loss expected from gravitational radiation [3]. It was not until the development of kilometer-scale interferometric detectors that direct detection became possible. After decades of effort, the first direct gravitational wave signal was observed in 2015 by the Advanced LIGO detectors, produced by the merger of two black holes [4]. This milestone, soon followed by detections of additional black hole mergers and even a binary neutron star inspiral, inaugurated the era of gravitational wave astronomy [5–9].

The key instruments enabling these discoveries are laser interferometers of extreme sensitivity. LIGO (Laser Interferometer Gravitational-Wave Observatory) in the United States, Virgo in Europe, and KAGRA (Kamioka Gravitational Wave Detector) in Japan are Michelson interferometers with arms kilometers in length, using highly stabilized lasers and advanced vibration isolation to measure tiny differences in arm length caused by passing gravitational waves [1, 10, 11]. These detectors, along with GEO 600 in Germany, form a network that can localize sources and improve confidence in detection.

The historical development of interferometric detectors has involved progressively more sophisticated techniques to reduce noise and increase sensitivity [12]. By the time of Advanced LIGO and Advanced Virgo, nearly all aspects of the interferometer design — from optics to suspensions — have been pushed to their limits by classical engineering. The current detectors operate at or near the fundamental noise floor set by nature, which means further improvements increasingly rely on *quantum* techniques and other innovative methods beyond classical physics.

This introduction will provide context on gravitational wave detection and then discuss several advanced concepts crucial to improving detector sensitivity: the field of quantum metrology as applied to gravitational wave instruments, the various fundamental noise sources that limit detectors, the idea of displacement-noise-free interferometry (DFI) to cancel certain noise channels, and modern signal estimation techniques like Kalman filtering for optimal real-time data analysis. We also highlight how these quantum-limited techniques can enhance the performance of current and future gravitational wave observatories. Finally, an outline of the thesis is given.

1.1 Gravitational Wave Detection: Historical Context

The quest to detect gravitational waves has driven significant innovation in experimental physics. Initial attempts employed massive solid aluminum bars cryogenically cooled and instrumented with resonant sensors (pioneered by Weber and others), aiming to register minute extensions caused by passing waves. While those resonant bar detectors set important early limits, they ultimately lacked the sensitivity for assured detection. The interferometric approach, first analyzed in detail by R. Weiss and others in the 1970s, promised greater sensitivity by measuring the phase difference of laser light in perpendicular long arms as a proxy for differential arm length changes. Prototypes such as the 40-meter interferometer at Caltech and the 10-meter Prototype in Glasgow demonstrated the feasibility of the concept [12].

This led to the construction of large-scale detectors: LIGO's two 4-km interferometers in Hanford and Livingston, Virgo's 3-km interferometer in Cascina, and later GEO600 (600 m) and the Japanese detector KAGRA (an underground 3-km interferometer with cryogenic mirrors). The first generation (Initial LIGO, Initial Virgo) reached unprecedented strain sensitivities ($\sim 10^{-21}/\sqrt{Hz}$) but observed no astrophysical signals during the late 2000s, consistent with expected low event rates at that sensitivity. These null results drove the upgrade to *Advanced* LIGO and Virgo, which began operation in 2015 with improved lasers, optics, and seismic isolation [1, 10].

In September 2015, during its first observing run, Advanced LIGO (aLIGO) detected GW150914 — the merger of a binary black-hole system [4]. This landmark detection was quickly followed by additional binary black hole events and, in August 2017, the binary neutron star inspiral GW170817, which was observed in both gravitational waves and across the electromagnetic spectrum. By the end of LIGO-Virgo's first

three observing runs, dozens of compact binary coalescences had been detected, firmly establishing gravitational wave astronomy as a new observational field [5–9].

These achievements were made possible by the extreme precision of interferometric measurements. The interferometers must measure changes in distance of order 10^{-19} m (about one ten-thousandth of a proton diameter) over multi-kilometer baselines. To reach this level, the detectors employ high-power (tens of watts) lasers, ultra-high vacuum tubes, near-perfect mirrors in Fabry-Perot arm cavities, and multi-stage pendulum suspensions to isolate mirrors from seismic noise. Advanced LIGO and Virgo also use active feedback control to keep the interferometer on its operating point, and multiple photodetectors with modulation/demodulation schemes to sense and control various degrees of freedom. Over the relevant frequency band (from $\sim$ 10 Hz up to a few kHz), the sensitivity is limited by different noise sources at different frequencies. As detectors improved, they began to be fundamentally limited by *quantum noise* (photon shot noise and radiation pressure noise) at the highest sensitivities, especially at frequencies above a few hundred Hz [1]. In essence, advanced gravitational wave detectors have reached the regime where quantum mechanics is crucial for their operation and sensitivity. This realization has led to the incorporation of quantum metrology techniques into detector design and a vigorous effort to explore new methods (both optical and analytical) to further push the sensitivity beyond classical limits.

1.2 Quantum Metrology and Gravitational-Wave Astronomy

Quantum-Limited Interferometry: Motivation and Techniques

Quantum metrology is the discipline of using quantum phenomena to enhance the precision of measurements beyond what is possible with classical techniques [13]. In the context of gravitational-wave detectors, quantum metrology has become essential because the detectors' precision is now limited by quantum effects of the light and the test masses.

The two main manifestations of quantum noise in an interferometer are *shot noise* and *radiation pressure noise*, which together set the so-called Standard Quantum Limit (SQL) for a given measurement device [14, 15]. Shot noise arises from quantum fluctuations in the number of photons detected (photon counting statistics) and dominates the interferometer noise spectrum at high frequencies (typically a few hundred Hz and above). It effectively imposes a limit on sensitivity at high frequency, where the signal is small and the integration time is limited. Radiation pressure noise, on

the other hand, is caused by quantum fluctuations in the radiation field imparting random momentum kicks to the mirrors; this noise is most significant at low frequencies, where such fluctuating force accumulates and can swamp low-frequency signals. In a simple Michelson interferometer with arm cavities, increasing the laser power can reduce shot noise (since more photons yield a better statistical averaging of photon counting) but at the cost of increasing radiation pressure noise (because the momentum kicks from the photons become stronger). This trade-off leads to an optimal power at which the combined effect of shot and radiation-pressure noise is minimized, and it defines the SQL for a given interferometer mass and optical power [15].

Pushing beyond the SQL requires the introduction of non-classical measurement schemes or altered test mass dynamics, which is precisely the realm of quantum metrology. A primary quantum metrology technique already in use in gravitational wave detectors is the injection of squeezed states of light to reduce quantum noise. The idea of squeezed light, first proposed for interferometers [14], is to prepare the vacuum field entering the unused port of the interferometer in a quantum state where the uncertainty in one quadrature (e.g., phase) is reduced below the vacuum level at the expense of increased uncertainty in the orthogonal quadrature (e.g., amplitude). By appropriately choosing the squeezed quadrature, one can reduce the dominant noise (shot noise at high frequency) while tolerating increased radiation pressure noise at low frequency, or vice versa. In practice, frequency-dependent squeezing can be realized by filtering the squeezed vacuum through a detuned cavity so that at high frequency the phase quadrature is squeezed (reducing shot noise), and at low frequency the amplitude quadrature is squeezed (reducing radiation-pressure noise). This technique was recently implemented in Advanced LIGO, resulting in improved high-frequency sensitivity and an overall increase in detection rate for certain astrophysical sources [16]. The use of 3–6 dB of squeezing has already become routine in the latest observing runs of LIGO and Virgo, marking one of the first real-world applications of quantum metrology to large-scale devices in physics.

Beyond squeezed light, other quantum metrology and quantum measurement ideas are being explored for future detectors. These include quantum non-demolition (QND) measurement schemes where the interferometer is tuned to measure a combination of variables that is unaffected by quantum back-action, for example using optical variational readout or introducing an optical spring to alter the mirror response [15]. There are proposals to entangle the test masses with light or use

exotic quantum states of the mirrors themselves to reduce sensing noise, though these remain at very early stages. In general, as gravitational wave detectors push for better sensitivity, especially at the low-frequency end (below 10 Hz) and high-frequency end (above a kHz), quantum metrology provides a toolkit of strategies to surpass classical noise limits. The relevance of these methods to gravitational-wave astronomy cannot be overstated: by lowering the noise floor, one can extend the observable volume of the universe and potentially enable detection of new sources (e.g., intermediate-mass black hole mergers at low frequencies, or high-frequency features of neutron star mergers). Thus, quantum metrology techniques are directly tied to the scientific reach of gravitational wave observatories. Indeed, the next generation of detectors plans to rely heavily on such techniques — for example, the envisioned Einstein Telescope and Cosmic Explorer aim to use 10 dB of squeezing, cryogenic mirrors, and other quantum enhancements to improve sensitivity by an order of magnitude across the band [17].

In summary, quantum metrology has transitioned from a theoretical curiosity to a practical necessity in gravitational wave detection, enabling current detectors to operate closer to the quantum limits and guiding the design of future instruments.

1.3 Noise Sources in Gravitational-Wave Interferometers

Even with perfect quantum measurement, gravitational wave detectors face numerous other noise sources that limit their sensitivity. A thorough understanding of these noise sources is crucial, since each one dominates in a particular frequency range and demands different mitigation strategies. Here we introduce the primary noise sources relevant to ground-based interferometric detectors: quantum noise (shot noise and radiation pressure), thermal noise, seismic noise, and Newtonian (gravity-gradient) noise.

Quantum Noise: Shot Noise and Radiation Pressure

As discussed, quantum noise originates from the fundamental quantum fluctuations of light and the quantum back-action on the test masses. *Shot noise* arises because the output photodetector measures an inherently discrete number of photons with Poissonian statistics. The spectral density of shot noise in strain measurement usually rises with frequency, meaning it is more severe at high frequencies. Shot noise currently limits Advanced LIGO and Virgo at frequencies above $\sim 200 - 300$ Hz [1]. The shot-noise-limited strain sensitivity h_n scales roughly as $h_n \propto \frac{1}{\sqrt{P}}$ (where P is the circulating power) and also depends on the detection scheme [18]. Shot

noise can be reduced by increasing laser power, but doing so exacerbates *radiation pressure noise*.

Radiation pressure is the fluctuating force on the mirrors due to momentum transfer from photons. Its effect is most pronounced at low frequencies, where the mirror pendulums (acting as free masses above their suspension resonance) are susceptible to being moved by these random force fluctuations, producing a displacement noise. The displacement noise from radiation pressure in an interferometer scales as $S_x^p \propto \frac{P}{m\Omega^4}$ (for a mirror of mass m, angular frequency Ω, and circulating power P), indicating a steep increase at low Ω. This is why very low frequencies (below $\sim$ 10 Hz) in ground-based detectors are practically unobservable — any potential gravitational wave signal is overwhelmed by mirror displacement noise from a combination of seismic and radiation-pressure effects. The competition between shot noise and radiation pressure noise leads to the Standard Quantum Limit as mentioned. Balancing these requires careful choices in interferometer design (mirror mass, optical power) and motivates the use of squeezed light or other quantum correlations to evade the trade-off. Indeed, with the application of frequency-dependent squeezed vacuum, the impact of quantum noise in Advanced LIGO's most recent run was reduced across the frequency band, yielding a broader and slightly flatter sensitivity spectrum [16]. In the longer term, increasing test mass (mirror) mass can also push the radiation-pressure effect to lower frequencies (since heavier masses are less affected by the same force), which is one reason future detectors plan to use 100–200 kg class mirrors instead of the 40 kg used in Advanced LIGO. In summary, quantum noise is a fundamental limitation that must be addressed by quantum metrology techniques as described, and it sets the ultimate high-frequency sensitivity of interferometers.

Thermal Noise

Thermal noise refers to fluctuations arising from the finite temperature of the detector's components, via the fluctuation-dissipation theorem [19]. In gravitational wave detectors, the most significant thermal noises are Brownian motion of the mirror substrates and coatings, and internal friction in the suspension fibers or wires holding the mirrors. Each mirror is suspended as a pendulum to isolate it from ground vibrations, but the pendulum itself has internal modes that can be thermally excited. The mirror's high-reflectivity coating (a multi-layer dielectric stack) also has mechanical loss, and its microscopic vibrations (driven by thermal energy) appear as surface position fluctuations, directly adding noise to the interferometer output.

Thermal noise typically dominates the *intermediate frequency band* of 50 – 200 Hz in current detectors. For example, in Advanced LIGO, the noise is limited by coating thermal noise — a manifestation of the mirror coating's mechanical loss [1]. The amplitude spectral density of thermal noise is often approximated as slowly rising in the central band and is independent of the laser power (unlike quantum noise). Mitigation of thermal noise is extremely challenging because it demands materials with extremely low mechanical loss and, potentially, operation at cryogenic temperatures to reduce thermal motion. The design choices for Advanced LIGO/Virgo already include high-quality fused silica test masses and low-loss coatings (e.g., doped tantala/silica layers) to minimize thermal noise. KAGRA has taken the approach of cooling its mirrors to 20 K to suppress thermal excitations [11], and future detectors like the Einstein Telescope plan to use both 10 K cryogenics and new crystalline coatings to drastically cut thermal noise [17]. The physics of thermal noise is an active research area; breakthroughs in materials science (for example, crystalline mirror coatings or optomechanical damping) could directly translate into improved sensitivity in the thermal-noise-limited band. Nonetheless, thermal noise is fundamentally tied to energy dissipation in materials, so it cannot be eliminated — only reduced.

Seismic Noise and Newtonian Gravity Noise

At the lowest frequencies (below a few tens of Hz), the dominant disturbances are related to the Earth itself. Seismic noise is the direct motion of the ground and thus of the interferometer's infrastructure and optics. Even with elaborate multi-stage seismic isolation platforms (active and passive), ground vibrations set a hard wall around 10 Hz for current interferometers. The seismic spectrum on Earth rises steeply at low frequencies (the ambient ground motion at 1 Hz is many orders of magnitude larger than the allowed mirror motion for detecting gravitational waves).

Advanced LIGO uses active feedback to subtract inertial sensor signals from platform motion and multiple pendulum stages to filter ground vibrations, achieving high suppression at some frequencies [1]. Yet, below about 5-10 Hz, seismic noise still leaks through and overwhelms potential signals. This is why the sensitive band of LIGO and Virgo is typically quoted as $\sim$ 10 Hz to a few kHz; signals below 10 Hz (such as those from very massive black hole binaries in early inspiral) cannot be detected on the ground. An important point is that seismic noise is *classical* and *technical* — in principle, one could imagine nearly perfect isolation or going to extremely quiet environments to improve it. Going underground (as done for Virgo

and KAGRA, and planned for Einstein Telescope) helps by reducing seismic noise (especially human-made cultural noise) at those frequencies.

However, even if seismic vibrations of the ground could be completely isolated, there is an even more inescapable low-frequency noise source: Newtonian noise, also known as gravity-gradient noise. Newtonian noise arises from time-varying gravitational forces on the test masses caused by density fluctuations in the environment. The primary contributors on Earth are seismic waves (compressional waves in the ground that change the local density and thus gravitational field) and atmospheric pressure fluctuations; human activity or moving objects can also contribute. Unlike seismic noise, Newtonian noise *cannot* be isolated by suspension systems, since it is not imparted through the instrument's structure but rather acts directly on the test mass via gravity. Saulson first estimated this effect in 1984 [20], showing that at low frequencies the gravitational pull from seismic density perturbations could rival the actual gravitational wave signal. Subsequent studies refined these calculations [21, 22], and Newtonian noise is predicted to be a limiting factor for future detectors below about 10 Hz.

For current detectors, Newtonian noise has not yet been observed directly in the noise spectrum because other technical noises dominate in the same band, but as seismic isolation improves and if detectors move underground, Newtonian noise will emerge as a new floor. Mitigation of Newtonian noise is extremely challenging; one approach is to deploy seismometer arrays around the test masses to measure the local ground motion field and then subtract the correlated gravitational effects from the detector output [23]. This is essentially a feed-forward cancellation strategy and has seen some experimental tests at observatories. Another approach is careful site selection (deep underground or near bedrock) to minimize the ambient seismic and acoustic fields. In summary, seismic and Newtonian noise define the low-frequency frontier of ground-based gravitational wave detection. Together, they impose a steep rise in the noise curve at tens of Hz and below, cutting off sensitivity to low-frequency gravitational waves. Tackling these sources requires both clever engineering (e.g., better isolation, underground facilities) and novel ideas such as sensor fusion for noise cancellation or new detector configurations that are intrinsically insensitive to common-mode environmental noise. One such conceptual idea is the topic of the next section: displacement-noise-free interferometry, which attempts to design the interferometer signal in a way that excludes seismic and other displacement noises from the measurement.

1.4 Displacement-Noise Free Interferometry (DFI)

The concept of Displacement-Noise-Free Interferometry (DFI) represents a radical approach to gravitational wave detection: arrange the detector signals in such a way that they respond to gravitational waves but are *insensitive* to certain displacement noises that normally plague measurements. In essence, a DFI configuration uses multiple interconnected interferometers or multiple measurement beams whose outputs are combined to cancel out the noise from platform motions, laser frequency noise, or other common disturbances, while preserving the gravitational wave signal. This idea was introduced by S. Kawamura and Y. Chen in 2004 [24], initially in the context of a thought experiment. Subsequent works expanded on the concept, describing specific interferometer topologies that could achieve DFI [25]. For example, one proposal uses four mirrors and multiple beamsplitters to form a network of four Mach-Zehnder interferometers arranged such that each mirror's displacement is sensed redundantly by more than one beam. By taking suitable linear combinations of the multiple interferometer output signals, the true gravitational wave signal (a differential strain) can be extracted while the spurious motions (e.g., all mirrors moving together due to a seismic shake) cancel out [25].

In theory, such an arrangement could greatly reduce low-frequency noise, potentially opening the sub-10 Hz band to gravitational wave observations on Earth. The motivation for DFI is clear: if one could cancel displacement noise (seismic, Newtonian, laser phase noise, etc.), the detector's sensitivity at low frequencies would improve dramatically, limited only by other sources like quantum noise. This would allow detection of signals that are currently inaccessible, such as gravitational waves from very massive binaries or early inspiral phases that radiate predominantly at frequencies of 0.1-10 Hz. DFI could be seen as analogous to forming a *null channel* for noise — a concept somewhat similar to the TDI (Time-Delay Interferometry) used in space-based detectors (like the future LISA) to cancel laser frequency noise by combining signals with appropriate delays [26].

However, implementing DFI on the ground is extraordinarily challenging. The interferometer configurations proposed are complex, requiring multiple perfectly balanced optical paths and extremely precise alignment and calibration. Any asymmetry between the nominally identical sub-interferometers would reintroduce the noise that one hoped to cancel. Furthermore, a significant finding was that while displacement noise can be canceled, the gravitational wave signal in a DFI scheme often comes in as a higher-order effect (for instance, proportional to the square

of frequency f^2 at low frequencies, instead of the flat response of a Michelson) [25]. This means that the gravitational wave signal itself is somewhat suppressed or appears in a form that makes the detector less sensitive to low-frequency waves than one might naively expect. In one study, it was concluded that a particular DFI configuration had a gravitational wave response at low frequency equivalent to a much shorter baseline detector, negating the sensitivity advantage [24]. Additionally, most DFI schemes require complex plumbing of multiple optical beams on potentially separated platforms, which introduces technical noise of its own.

To date, no displacement-noise-free interferometer has been built or demonstrated experimentally; the concept remains an area of theoretical investigation. However, the pursuit of DFI has led to deeper understanding of the fundamental coupling of gravitational waves to a network of test masses and has inspired related ideas. One offshoot concept is the use of tensor interferometers that measure multiple components of the tidal gravitational wave field (the "gravity gradient") rather than a single differential length [27]. Such a full-tensor measurement, if achievable, could in principle distinguish true spacetime strain from local acceleration noise by its tensorial signature, thus inherently canceling local Newtonian noise. The proposals by Paik and collaborators for a six-degree-of-freedom superconducting gravity gradiometer are an example of this approach, conceptually similar to DFI in spirit. While such futuristic designs may or may not be realizable, they underscore the importance of out-of-the-box ideas (like DFI) for tackling the low-frequency gravitational wave detection problem.

In summary, Displacement-Noise-Free Interferometry is an ambitious proposal aiming to circumvent what currently seems inevitable — the noise from moving mirrors and ground vibrations. The principles behind DFI highlight that if one has multiple readouts of the gravitational wave signal, one can form combinations that cancel noise. The challenges, however, are substantial: the reduced signal response and the complexity of implementation mean that DFI is not yet a practical solution for present detectors. In this thesis, we will revisit the concept of DFI to assess its potential and study its quantum precision limits. Even if fully noise-free detection remains elusive, understanding the limits of DFI helps clarify what improvements are fundamentally possible and what trade-offs are unavoidable.

1.5 Signal Readout and Estimation in Interferometers

The standard method of reading out the gravitational wave signal in interferometric detectors has historically been a form of linear measurement of the interferometer output power (or a related error signal) followed by filtering and analysis. For example, initial LIGO employed a heterodyne readout: the interferometer was operated at a dark fringe with a slight modulation, and the gravitational wave signal appeared as sidebands in the photodetector output that were extracted via demodulation. Advanced LIGO simplified this to a homodyne *DC readout*, holding the interferometer just off dark fringe so that the signal directly causes a DC power fluctuation at the antisymmetric port [1]. In both cases, the readout yields a time series (the strain $h(t)$) that contains the gravitational wave signal plus noise. Traditional approaches treat the interferometer as a static linear device and apply frequency-domain filtering (whitening, etc.) and matched filtering *offline* to extract signals from the noise. However, as detectors become more sensitive, especially near fundamental noise floors, there is interest in more sophisticated *real-time signal estimation* techniques that could enhance the detector's ability to discern signals or suppress noise in real time.

One such technique is the usage of Kalman filter, an approach from control theory and signal processing that provides an optimal recursive estimation of the state of a system given a time series of observations and a dynamic model. The Kalman filter (and its variants, like the Extended Kalman Filter and Unscented Kalman Filter for nonlinear systems) has seen growing interest in the gravitational wave community as a tool for noise cancellation and potentially signal tracking. The basic idea is to treat the interferometer and its dominant noise sources as a dynamic system with hidden variables (for example, the physical displacement due to a gravitational wave, the excitations of suspension resonances, etc.). By inputting the measured data (which is a superposition of these effects), the Kalman filter continuously updates its estimate of the system state in a way that statistically minimizes the estimation error, given models for the signal and noise dynamics.

A concrete application was demonstrated by [28], who designed a Kalman filter to track and subtract the *suspension violin mode* oscillations in a gravitational wave detector. These violin modes are narrow resonance peaks in the detector noise caused by the oscillation of the suspension fibers (holding the mirrors) at their harmonics (typically in the 300-700 Hz range). Because the frequency of these modes can vary slowly with environmental conditions and the modes can be excited by disturbances,

simple notch filters are not always optimal to remove them. Finn and Mukherjee showed that a Kalman filter can effectively "lock on" to these sinusoidal noise components, continually adjusting for any changes in their frequency or phase, and subtract them from the data stream. This is an early example of data conditioning using state-estimation techniques to improve the detector output in real time.

Similarly, related optimal estimation methods have been proposed to assist in sensing and control of the interferometer itself — for instance, tracking angular motions or isolating specific vibration modes. More recently, real-time optical sensing schemes have been combined with Kalman filtering to push the envelope of what can be measured. A notable example is an experiment by [29], where an adaptive optical phase tracking setup (involving a time-delayed local oscillator) was augmented with an extended Kalman filter to achieve optimal homodyne detection of fast varying phase signals. This setup was able to track a rapidly changing optical phase with higher accuracy than a traditional phase-locked loop, by using the Kalman filter's predictive ability to compensate for the delay in the loop. The success of such demonstrations highlights that advanced filtering can effectively increase the bandwidth of measurement and reduce latency, which is crucial for following fast signals (e.g., high-frequency gravitational wave bursts or ringdown signals).

In the context of gravitational wave astronomy, the emergence of real-time filtering techniques like the Kalman filter offers several potential benefits. First, they can be used to suppress known noise sources in real time, improving the duty cycle and livetime of high-sensitivity operation. For instance, environmental disturbances (like vibrations at specific frequencies from machinery) could be subtracted using an observer that fuses data from environmental sensors with the interferometer output, similar in spirit to feed-forward noise cancellation demonstrated for Newtonian noise [23]. Second, real-time signal tracking could allow the detector (or the data analysis pipeline at the observatory site) to respond dynamically to signals of interest. One could imagine, for example, a Kalman filter that is initialized with a coarse model of an expected gravitational waveform (such as a predicted signal from a neutron star spinning down or a supernova) and that updates the estimate as data comes in, effectively performing a continuously refined matched filtering. This is speculative, but it illustrates how moving some of the signal processing into the real-time domain could complement the more traditional offline searches, potentially reducing latency for multi-messenger follow-up or enabling detection of longer-duration signals that are difficult to handle in batch processing. It is important to note that any model-

based filtering approach, like Kalman filtering, relies on accurate models of the detector and noise. An improperly tuned Kalman filter could in fact introduce bias or instability. Thus, significant calibration and understanding of the detector's transfer functions are required.

In this thesis, we investigate the application of Kalman filtering to the gravitational wave interferometer readout for real-time gravitational wave signal tracking. We will show how one can construct a state-space model of signal parameters and apply a Kalman estimator, and we will discuss the advantages, limitations, and practical considerations (like computation speed and robustness) of deploying such techniques in current detector readouts.

1.6 Towards Quantum-Enhanced Broadband Detectors

Gravitational wave detectors are now operating in a regime where nearly all dominant noise sources are at or approaching their fundamental limits. For current observatories, incremental improvements in hardware and better noise subtraction have yielded some gains, but major sensitivity breakthroughs will come from implementing the kinds of advanced techniques discussed above — quantum metrology methods, sophisticated noise cancellation, and novel interferometer designs. By attacking the quantum noise at high frequencies (with squeezing and other QND techniques) and the environmental noise at low frequencies (with strategies like DFI-inspired configurations or sensor fusion cancellation), the goal is to achieve a broadband reduction in noise, thereby increasing the detector's astrophysical reach both in volume and in the range of source frequencies.

Already, the adoption of quantum squeezing in Advanced LIGO and Advanced Virgo has improved their high-frequency sensitivity, effectively enlarging the volume of space in which mergers can be observed. The use of a 300 m filter cavity to produce frequency-dependent squeezed light [30] is a prime example of quantum-enabled bandwidth improvement: it mitigated the high-frequency shot noise without paying the usual penalty in low-frequency radiation pressure noise, thus widening the bandwidth of quantum noise reduction. In the coming years, incremental upgrades (sometimes dubbed "Advanced LIGO+" and similar for Virgo) plan to increase the squeezing level, use even lower loss optics, and possibly introduce adaptive optics, all with the aim of approaching 10dB of effective quantum noise suppression across much of the band.

At low frequencies, the challenges of seismic and Newtonian noise are being met by proposals to build detectors underground and use longer baselines. The Einstein Telescope project, for instance, is a design for a future European detector that would be situated in a ~200 m deep underground facility to greatly reduce seismic and Newtonian noise [17]. Its triangular 10-km arm length design with multiple interferometers (including a pair of cryogenic low-frequency optimized interferometers and a pair of high-frequency optimized ones) can be viewed as an extension of some DFI principles — using multiple signals and orientations to maximize sensitivity and cancel noise where possible. Although ET does not explicitly implement a DFI scheme as in [24], the multi-detector approach and the use of a seismic array for Newtonian noise cancellation are in the same spirit. Likewise, Cosmic Explorer, a proposed U.S. 40-km single L-shaped interferometer, relies on sheer scale (longer arms, heavier masses) and advanced isolation to push down noise. Both designs count on heavy use of quantum metrology (e.g., squeezing) and also anticipate incorporating real-time noise removal where feasible. For instance, global sensor networks might monitor seismic and atmospheric conditions to subtract Newtonian noise in real time, much as Driggers et al. demonstrated at a small scale [23].

In summary, the trajectory of gravitational wave detector development is toward instruments that are simultaneously larger, quieter, and smarter: larger to reduce fundamental noise by averaging (longer arms, heavier masses), quieter by environmental isolation (underground sites, cryogenics, better materials), and smarter by leveraging quantum physics and advanced signal processing to circumvent classical limits. Quantum-limited techniques, whether it is squeezing the light or using optimal estimators to remove noise, are central to this vision. The work presented in this thesis aims to contribute to this ongoing effort by examining two fronts: (1) how quantum measurement strategies like DFI could inform improvements in isolating gravitational wave signals from noise, and (2) how modern estimation algorithms like Kalman filters can be applied to the detector data stream to enhance real-time signal extraction. These studies are timely as the community prepares for the next observing runs and looks ahead to third-generation detectors.

1.7 Thesis Outline

This thesis is organized into the following chapters and appendices:

- Chapter 2 focuses on Displacement-Noise Free Interferometers (DFI). The chapter details the theoretical formalism and models employed to analyze DFI

schemes, particularly emphasizing a proposed triangular cavity configuration. Key results from the analysis of quantum precision limits, including the impact of realistic noise profiles and quantum squeezing, are discussed. The supplemental material for this chapter can be found in Appendix A, which includes detailed derivations and analytical expressions related to Displacement-Noise Free Interferometers, such as the two-photon formalism, calculation of Quantum Fisher Information, optimal measurement bases, effects of squeezing, and noise analysis. Finally, extensions to more complex interferometric setups are also provided.

- Chapter 3 focuses on Linear Waveform Estimation Using Kalman Filters. This chapter introduces the motivation and fundamental theory behind waveform estimation techniques in gravitational-wave interferometers. A detailed explanation of the Kalman filtering approach is given, alongside the results from numerical simulations demonstrating the performance of Kalman filters in estimating gravitational-wave signals under various noise conditions. The supplemental material in Appendix B covers additional technical details related to waveform estimation using Kalman filters, including two-photon formalism for signal susceptibility, normalization procedures, optimal quadratures for measurement, advanced filtering techniques, and practical implementation considerations.

Chapter 2

DISPLACEMENT-NOISE FREE INTERFEROMETERS

Tuvia Gefen, Rajashik Tarafder, Rana X. Adhikari, and Yanbei Chen. Quantum precision limits of displacement noise-free interferometers. *Phys. Rev. Lett.*, 132: 020801, Jan 2024. doi: 10.1103/PhysRevLett.132.020801. URL `https://link.aps.org/doi/10.1103/PhysRevLett.132.020801`. R.T. participated in formulating the theory, developing the code, and writing the manuscript.

2.1 Introduction

Quantum metrology studies fundamental precision limits in physical measurements imposed by quantum physics. Recent progresses in this field have led to formulation of precision limits for a variety of sensing devices: gravitational wave (GW) detectors [14, 31–37], magnetometers [38, 39], atomic clocks [40–43], nano-NMR [44–48], etc.

We focus here on optomechanical sensors and laser interferometers. These platforms have emerged as the primary instruments for the detection of GWs, with successful observations conducted by several of these detectors [4, 5, 7, 9, 49]. They are, however, severely limited by noise sources that displace the mirror positions in the interferometer: thermal noise, Radiation Pressure Noise (RPN), seismic noise, and Newtonian gravity noise [20–23, 50]. These noises are in particular dominant in the low-frequency regime (< 10 Hz), thus limiting the sensitivity at this range and preventing detection of various signals such as intermediate-mass black holes, young Neutron Stars, extreme mass ratio in-spirals, etc. Circumventing displacement noise is thus an outstanding challenge for GW detection and optomechanical sensors in general.

Interestingly, the coupling of light fields to GW signals is different from their coupling to mirror displacement, i.e., GW information is accumulated along the optical path, unlike displacement noise which is only introduced at the mirrors. This observation has led to proposals of interferometers wherein displacement noise can be canceled while not losing the GW signal [24]. This approach is referred to as Displacement-noise Free Interferometry (DFI).

DFI for laser interferometry was originally proposed using a simplified system and later expanded to more complex systems such as speed meters and 3D-interferometers [25, 51–55]. A similar approach for laser phase noise cancellation has also been proposed for LISA using Time Delay Interferometry [26, 56, 57]. However, DFI systems with requisite sensitivities remain elusive. Furthermore, a rigorous study of the quantum precision limits of these interferometers has not been conducted.

In this chapter, we use quantum metrology techniques to derive general precision limits, optimal measurements, and optimal squeezing quadratures for DFI schemes. We develop a triangular cavity DFI scheme, which combines resonance power amplification and DFI, and apply our results to analyze it. In addition to the improved sensitivity at low frequencies, we observe interesting effects that motivate the use of DFI and multichannel interferometers. We identify pseudo displacement-free subspaces, i.e., subspaces that are displacement-free for a limited range of frequencies. These subspaces lead to unexpected sensitivity profiles and further noise suppression. Lastly, we study the effect of squeezing and show that DFI increases the sensitivity gain from squeezing in the high displacement noise regime.

2.2 Formalism and Model

Previous DFI schemes used several Mach-Zender interferometers [25, 51]. However, these interferometers did not incorporate cavity resonance to amplify the power and sensitivity. Here, we propose a scheme that combines DFI with cavity resonance gain: an equilateral triangular cavity with three mirrors, six input local-oscillator fields and six outputs. The six fields circulate inside the cavity — split between the clockwise and anti-clockwise directions. The scheme and suggested parameters are described in fig. 2.1. This triangular cavity yields power amplification: given identical mirrors transmissivities (T), the ratio between the intracavity power and the total input power is $T/[3\left(1-\sqrt{1-T}\right)^2]$.

We show that this scheme is indeed a DFI. The intuition for this is simple: the displacement noise is generated by the three mirrors and induced on the six output fields. Since the number of mirrors is smaller than the number of output fields, we have modes that are decoupled from this noise and enable the DFI. This approach is formulated below.

We use a general formulation that holds for any system with n mirrors and k fields, such that $k > n$. The system is described using the input-output formalism [58, 59] and we denote the quadrature operators of the input and output fields

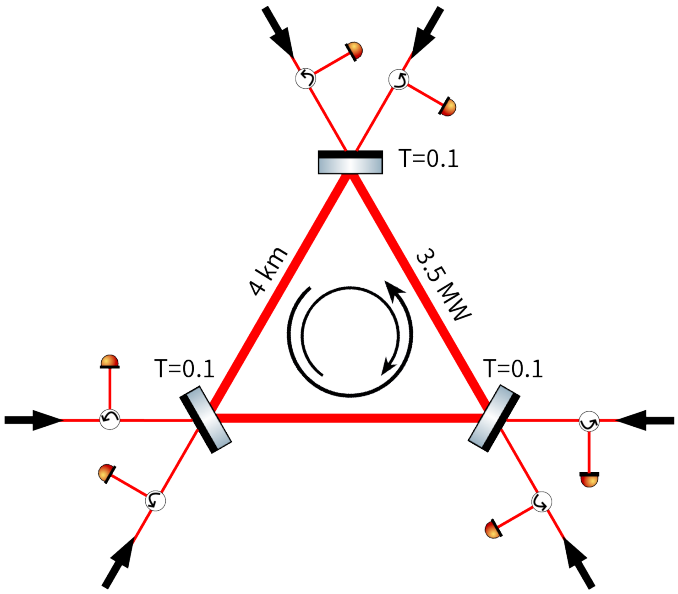

Figure 2.1: Sketch of the DFI scheme: a symmetric triangular cavity is formed by three mirrors and six input laser fields. Six detectors are placed in the opposite direction of the input fields. The configuration leads to both a clockwise and an anti-clockwise circulating field within the cavity. We used the following parameters: Arm length: $L = 4$km, Laser wavelength: 1064 nm (same as advanced LIGO [1]). Mirrors mass: 5 kg, Intracavity Power: 3.5MW (to enhance RPN for illustrations). Power transmissivity of the mirrors: $T = 0.1$.

as $\hat{\mathbf{Q}}_{\text{in}} = \begin{pmatrix} \hat{\mathbf{a}}_1 \\ \hat{\mathbf{a}}_2 \end{pmatrix}, \hat{\mathbf{Q}}_{\text{out}} = \begin{pmatrix} \hat{\mathbf{b}}_1 \\ \hat{\mathbf{b}}_2 \end{pmatrix}$, respectively. $\hat{\mathbf{a}}_1$, $\hat{\mathbf{b}}_1$ are the k-dimensional vectors of amplitude quadratures, and $\hat{\mathbf{a}}_2$, $\hat{\mathbf{b}}_2$ are the k-dimensional vectors of phase quadratures. These quadratures satisfy the standard commutation relations: $\left[\left(\hat{\mathbf{Q}}_{\text{out}}\right)_l, \left(\hat{\mathbf{Q}}_{\text{out}}\right)_k\right] = J_{l,k}$ with $J = i\begin{pmatrix} 0 & \mathbb{1}_k \\ -\mathbb{1}_k & 0 \end{pmatrix}$ (same for $\hat{\mathbf{Q}}_{\text{in}}$). The noisy displacement of the mirrors is denoted as $\{\Delta x_i\}_{i=1}^{n}$, and the amplitude of the GW polarization vector is given by $\mathbf{h} = (h_+, h_\times)^T$. The input-output relations in the frequency domain are then:

$$\hat{\mathbf{Q}}_{\text{out}}(\Omega) = M(\Omega)\,\hat{\mathbf{Q}}_{\text{in}}(\Omega) + \mathcal{V}(\Omega)\,\mathbf{h}(\Omega) + A(\Omega)\,\Delta\mathbf{x}(\Omega)\,. \tag{2.1}$$

$\Omega = 2\pi f$ is the angular frequency; hereafter this notation will be suppressed. M, A, $\mathcal{V}$ are the transfer matrices of the input modes, displacement noise, and the GW vector, respectively. Accordingly, these are $2k \times 2k$, $2k \times n$, and $2k \times 2$ dimensional matrices, that take the following general form (assuming carrier

frequency is resonant with the arm length):

$$M = \begin{pmatrix} M_{\text{int}} & 0 \\ M_{21} & M_{\text{int}} \end{pmatrix}, A = \begin{pmatrix} 0 \\ A_{\text{ph}} \end{pmatrix}, \\ \mathcal{V} = \begin{pmatrix} 0 \\ \mathcal{V}_{\text{ph}} \end{pmatrix} = \begin{pmatrix} 0 & 0 \\ \boldsymbol{\mathcal{V}}_{+,\text{ph}} & \boldsymbol{\mathcal{V}}_{\times,\text{ph}} \end{pmatrix}. \tag{2.2}$$

M_{int} is a $k \times k$ unitary interferometer transfer matrix and M_{21} is a $k \times k$ coupling matrix between the amplitude and phase quadratures due to Radiation Pressure Noise (RPN). $A, \mathcal{V}$ act only on the phase quadratures, with their support being $A_{\text{ph}}(k \times n$ dimensional), $\mathcal{V}_{\text{ph}}$ ($k \times 2$ dimensional). $\mathcal{V}_{\text{ph}}$ consists of two column vectors: $\boldsymbol{\mathcal{V}}_{+,\text{ph}}, \boldsymbol{\mathcal{V}}_{\times,\text{ph}}$, these are k-dimensional transfer vectors of $h_+, h_\times$, respectively. A detailed description of how to calculate these transfer matrices can be found in refs. [59] and Appendix A.

We are now poised to define the Displacement Free Subspace (DFS): this is the space of phase quadratures of the form: $\mathbf{u} \cdot \hat{\mathbf{b}}_{\mathbf{2}}$ with $\mathbf{u} \in \ker\left(A_{\text{ph}}^{\dagger}\right)$. Since $\mathbf{u}^{\dagger} A_{\text{ph}} \boldsymbol{\Delta}\mathbf{x} = 0$, these quadratures are decoupled from the displacement noise term in eq. (2.1) and thus resilient to this noise. Thinking of the phase quadratures as k-dimensional column vectors, the DFS is then the kernel of $A_{\text{ph}}^{\dagger}$. We denote this subspace and its projection operator as M_{DFS} and Π_{DFS}, respectively. The orthogonal complement of the DFS is the coupled subspace, it is the linear span of the column vectors of A_{ph}. This subspace and its projection operator are denoted as M_C and Π_C, respectively. Since $A_{\text{ph}}^{\dagger}$ is an $n \times k$ dimensional matrix, a sufficient condition for the existence of DFS is $k > n$, i.e., more fields than mirrors.

2.3 Quantum Precision Limits

Our figure of merit is the minimal detectable GW amplitude in any given polarization. With our interferometer, the dominant polarization is approximately h_+, hence the figure of merit is the standard deviation in estimating h_+, we denote it as σ and refer to it as the Standard Deviation (SD) or the sensitivity. This reduces the problem to a single parameter estimation of h_+, where the sensitivity is calculated below using the Cramér-Rao Bound.

According to the Cramér-Rao Bound, given a readout scheme with outcomes distribution $\{p(x)\}_x$, the variance, σ^2, of any unbiased estimator of h_+ satisfy: $\sigma^2 \geq F^{-1}$, with $F = \left\langle \left(\partial_{h_+} \ln(p)\right)^2 \right\rangle$ being the Fisher Information (FI). This lower bound is asymptotically tight [60].

In the quantum context, further optimization over the detection schemes yields the Quantum Fisher Information (QFI), denoted as I, [61] such that for any readout scheme $\sigma^2 \geq I^{-1}$.

In our case the QFI has a particularly simple form [37, 62, 63]:

$$I = 2\left(\partial_{h_+}\mathbf{d}_q\right)^\dagger \Sigma_q^{-1}\left(\partial_{h_+}\mathbf{d}_q\right), \tag{2.3}$$

where $\mathbf{d_q}$ and Σ_q are the mean vector and covariance matrix of $\hat{\mathbf{Q}}_{\text{out}}$, respectively:

$$\mathbf{d_q} = \langle\hat{\mathbf{Q}}_{\text{out}}\rangle, \left(\Sigma_q\right)_{i,j} = \frac{1}{2}\left\langle\left\{\hat{Q}_{\text{out},i}, \hat{Q}^\dagger_{\text{out},j}\right\}\right\rangle - \langle\hat{Q}_{\text{out},i}\rangle\langle\hat{Q}^\dagger_{\text{out},j}\rangle, \tag{2.4}$$

with $\{\bullet,\bullet\}$ being the anti-commutator of the operators. This simple form is because the output modes are in Gaussian state, and information about $\mathbf{h}$ is encoded only in the $\mathbf{d_q}$.

From eqs. (2.1) and (2.2) we observe that $\partial_{h_+}\mathbf{d_q} = \boldsymbol{\mathcal{V}}_+$, with $\boldsymbol{\mathcal{V}}_+ = \begin{pmatrix} 0 & \boldsymbol{\mathcal{V}}_{+,\text{ph}} \end{pmatrix}^T$, and that $\Sigma_q = M\Sigma_i M^\dagger + A\Sigma_{\mathbf{\Delta x}}A^\dagger$, where Σ_i, $\Sigma_{\mathbf{\Delta x}}$ are the covariance matrices of the input quadratures and the displacement noise $\mathbf{\Delta x}$, respectively. Assuming the input state is vacuum and the displacement noise is Gaussian i.i.d.: $\mathbf{\Delta x} \sim N\left(0, \frac{1}{2}\delta^2\mathbb{1}\right)$, the covariance matrix is then $\Sigma_q = \frac{1}{2}\left(MM^\dagger + \delta^2 AA^\dagger\right)$, and the QFI reads:

$$I = 4\boldsymbol{\mathcal{V}}_+^\dagger\left(MM^\dagger + \delta^2 AA^\dagger\right)^{-1}\boldsymbol{\mathcal{V}}_+. \tag{2.5}$$

In eq. (2.5), the RPN is included in the $MM^\dagger$ term, and the rest of the displacement noise is encoded by the additional $AA^\dagger$ term. The shot noise limit is obtained by nullifying the RPN and the displacement noise, i.e., M is unitary and $\delta = 0$, which yields: $I = 4\boldsymbol{\mathcal{V}}_+^\dagger\boldsymbol{\mathcal{V}}_+$. This limit serves as an upper bound to any noisy QFI scenario.

The QFI (eqs. (2.3) and (2.5)) is attainable with a homodyne measurement of the quadrature $\left(\Sigma_q^{-1}\boldsymbol{\mathcal{V}}_+\right)\cdot\hat{\mathbf{Q}}_{\text{out}}$ (Appendix A.4, [64]). Our sensitivity curves will therefore correspond to either the QFI, i.e., the SD with an optimal measurement: $\sigma = 1/\sqrt{I}$, or to the FI with a specific homodyne measurement: $\sigma = 1/\sqrt{F}$.

2.4 Precision Limits of the Simplified Model

We begin with a simplified model to develop an understanding of the DFI method. The simplified model is devoid of RPN, i.e., M is unitary, and the displacement noise is taken to be a white noise, i.e., $\delta(\Omega)$ is constant. The QFI is therefore:

$$I = 4\boldsymbol{\mathcal{V}}_+^\dagger\left(\mathbb{1} + \delta^2 AA^\dagger\right)^{-1}\boldsymbol{\mathcal{V}}_+. \tag{2.6}$$

The sensitivity for different levels of δ, ranging from the shot noise limit ($\delta = 0$) to infinite displacement noise ($\delta \to \infty$), is presented in fig. 2.2 (a). The DFI property is manifested in the fact that as $\delta \to \infty$ the standard deviation remains finite, denoted by the black line in fig. 2.2 (a). We thus have finite noise in GW detection even in the presence of infinite displacement noise.

To understand the behavior of the sensitivity, we note that the QFI can be decomposed as:

$$\begin{aligned} I &= F_{\mathrm{C}} + F_{\mathrm{DFS}} \\ &= 4\boldsymbol{\mathcal{V}}_+^\dagger \Pi_{\mathrm{C}} \left(\mathbb{1} + \delta^2 A A^\dagger\right)^{-1} \Pi_{\mathrm{C}} \boldsymbol{\mathcal{V}}_+ + 4\boldsymbol{\mathcal{V}}_+^\dagger \Pi_{\mathrm{DFS}} \boldsymbol{\mathcal{V}}_+. \end{aligned} \tag{2.7}$$

The first term (F_{C}) is the information from the coupled subspace and the second term (F_{DFS}) is the information from the DFS.

In the infinite displacement noise limit ($\delta \to \infty$), the first term, F_C, vanishes and thus the QFI in this limit is:

$$I_{\delta\to\infty} = 4\boldsymbol{\mathcal{V}}_+^\dagger \Pi_{\mathrm{DFS}} \boldsymbol{\mathcal{V}}_+; \tag{2.8}$$

i.e., we get information only from the DFS.

As $f \to 0$ this standard deviation diverges, indicating that in this regime $\Pi_{\mathrm{DFS}} \boldsymbol{\mathcal{V}}_+ \to 0$. For finite δ (dashed lines in fig. 2.2 (a)), the QFI converges to

$$I \approx (4/\delta^2) \boldsymbol{\mathcal{V}}_+^\dagger \left(A A^\dagger\right)^{-1} \boldsymbol{\mathcal{V}}_+ \tag{2.9}$$

at low frequencies, and thus σ grows as δ in this limit.

Furthermore, using eq. (2.7) we can quantify the effectiveness of the DFI with the following coefficient: $\eta = \frac{F_{\mathrm{DFS}}}{F_{\mathrm{DFS}}+F_C}$, i.e., the fraction of the information that comes from the DFS. It will be shown that η has an operational meaning as the gain from squeezing in the limit of large displacement noise.

2.5 Precision Limits with Realistic Noise Profiles

Let us now consider the sensitivity with realistic thermal noise and RPN. We begin by analyzing the effect of RPN alone and then study the combination of the two noises.

The effect of RPN is given by a non-unitary M, i.e., non-zero M_{21} matrix (eq. (2.2)). We assume that the mirrors are free masses, hence $M_{21} \propto \frac{1}{m\Omega^2}$, where m is the mass of the mirrors. This typically leads to a sensitivity profile that scales as Ω^{-2} [36, 37].

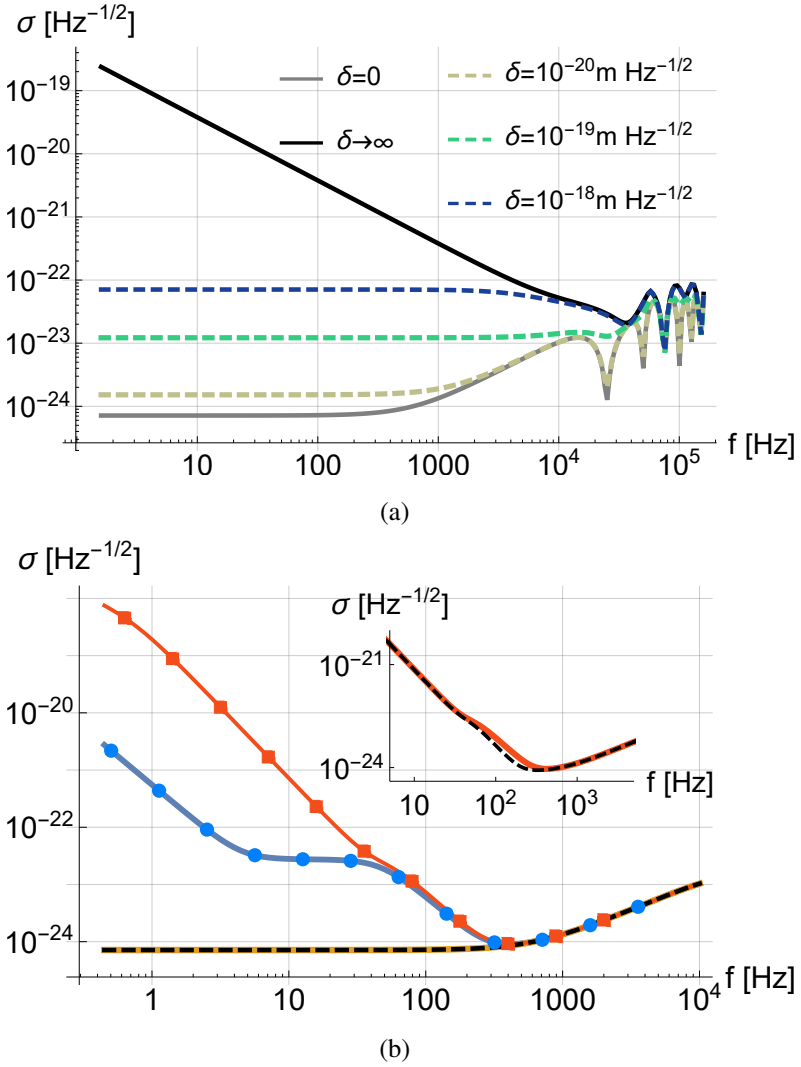

Figure 2.2: Quantum precision limits with varied noise sources. (a) Precision limits with the simplified model: The SD, σ, as a function of frequency for different levels of displacement noise (δ) (eq. (2.6)). The DFI property is manifested in the fact that σ is finite in the limit of infinite displacement noise (solid black curve). (b) Precision limits with realistic noise profiles. Given RPN alone, by measuring the optimal quadratures (eq. (2.10)) the QFI (black dashed line) coincides with the shot noise limit (solid yellow line). On the other hand, measuring the (non-optimal) phase quadratures, yields the solid blue (circles) line (eq. (2.11)). Similarly, given both RPN and thermal noise, measuring the phase quadratures yields the solid red (rectangles) line. Inset: Comparison between the phase quadratures FI (solid red line) and the QFI (black dashed line) in the presence of thermal noise and RPN.

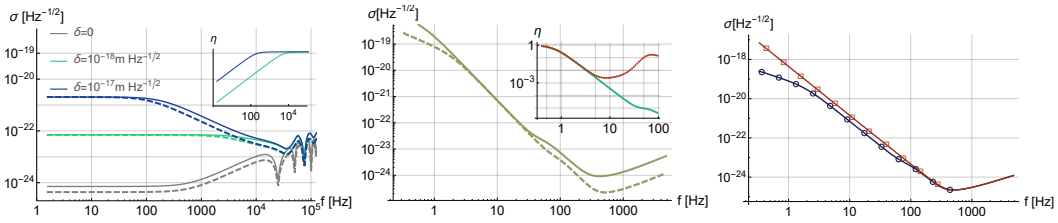

(a) (b) (c)

Figure 2.3: Effect of squeezing. (a) Performance with squeezing in the simplified model: Dashed lines correspond to SD (σ) with squeezing and solid lines to unsqueezed. For white displacement noise, squeezing becomes not effective at lower frequencies as can be also observed from the plot of η in the inset. (b) Performance with squeezing given thermal noise and RPN: The solid (dashed) line corresponds to unsqueezed (optimally squeezed) SD with phase quadratures measurement. Inset: η_{gain} (red dots) and η (green line) as a function of frequency. (c) The SD with optimal squeezed input and optimal measurement (blue curve, circles) compared to the SD with the same squeezed input but a readout combination that maximizes the signal (red curve, squares).

The QFI, in this case, saturates the shot noise limit (black dashed line in fig. 2.2 (b)), i.e., RPN is completely removed by measuring an appropriate choice of quadratures. This is a generalization of the optimal frequency-dependent readout introduced in ref. [31, 65]. Specifically, the k quadratures given by the column vectors of the matrix:

$$T_{\text{dec}} = \begin{pmatrix} -M_{\text{int}} M_{21}^{\dagger} \\ \mathbb{1} \end{pmatrix} \tag{2.10}$$

are decoupled from RPN and homodyne measurement of the corresponding k operators, $T_{\text{dec}}^{\dagger} \hat{\mathbf{Q}}_{\text{out}}$, saturates the QFI and the shot noise limit.

Measuring these optimal quadratures is experimentally challenging, the standard and simple readout quadratures are the phase quadratures. Phase quadratures however are not decoupled from RPN and measuring them yields the following FI (Appendix A.6):

$$F = 4 \boldsymbol{\mathcal{V}}_{+,\text{ph}}^{\dagger} \left(\mathbb{1} + M_{21} M_{21}^{\dagger} \right)^{-1} \boldsymbol{\mathcal{V}}_{+,\text{ph}}. \tag{2.11}$$

This expression is analogous to the QFI of the simplified model (eq. (2.6)), where the term $M_{21} M_{21}^{\dagger}$ is the displacement noise caused by RPN. It can be shown that $M_{21} = A_{\text{ph}} D_x$, where D_x is the transfer matrix of the amplitude quadratures to the displacement of the mirrors (Appendix A.6).

The DFS is therefore decoupled from this noise. The corresponding sensitivity is presented in the solid blue line (circles) of fig. 2.2 (b), where we observe an interesting behavior: unlike the conventional sensitivity curves, it does not diverge uniformly as $1/\Omega^2$ [15], instead there is a range of frequencies where the divergence stops. This plateau is due to a pseudo-DFS, a subspace that is impervious to displacement noise in this range of frequencies. Let us further elaborate on this.

In our triangular cavity scheme the phase quadratures can be decomposed to three orthogonal eigenspaces of the covariance matrix: $M_{\min} \oplus M_{\max} \oplus M_{\mathrm{DFS}}$, where $M_{\min} \oplus M_{\max}$ is a decomposition of M_{C} to eigenspaces with minimal and maximal eigenvalues, respectively. Since these are eigenspaces of the covariance matrix, the FI is a sum of the FI's achieved with each one of them separately, i.e.: $F = F_{\min} + F_{\max} + F_{\mathrm{DFS}}$. For different frequencies, different subspaces are dominant, this accounts for the non-uniform divergence. The plateau appears when $F_{\min}$ becomes dominant. $M_{\min}$ is immune to displacement noise in this range of frequencies, i.e., it is an eigenspace of $M_{21}M_{21}^{\dagger}$ with an eigenvalue that is much smaller than shot noise, hence the plateau. This is discussed further in the Appendix A.6.

Let us now consider thermal noise as well. The thermal noise is modeled as $\mathbf{\Delta x} \sim N\left(0, \frac{1}{2}\delta^2 \mathbb{1}\right)$, where $\delta^2(f) = 2.7 \cdot 10^{-30}(1/f)^5$ meter^2/Hz [66]. Hence, the effect of thermal displacement noise is similar to the simplified model with a frequency-dependent δ.

In the presence of both RPN and thermal displacement noise, the optimal measurement quadratures are the quadratures of eq. (2.10), which are decoupled from RPN. Hence RPN is completely canceled and we are left only with the thermal noise. The QFI thus takes the form of eq. (2.6) with a frequency-dependent δ. A plot of the corresponding sensitivity is presented in the inset of fig. 2.2.

Measuring the phase quadratures, RPN is not canceled and the FI reads:

$$4\boldsymbol{\mathcal{V}}_{+,\mathrm{ph}}^{\dagger}\left(\mathbb{1} + M_{21}M_{21}^{\dagger} + \delta^2 A_{\mathrm{ph}}A_{\mathrm{ph}}^{\dagger}\right)^{-1}\boldsymbol{\mathcal{V}}_{+,\mathrm{ph}}. \tag{2.12}$$

The plot of the corresponding sensitivity profile (red solid line) and a comparison with the QFI (black dashed line) is presented in the inset of fig. 2.2 (b). Three different regimes can be observed in the plot, that correspond to three eigenspaces of the covariance matrix. For low enough frequencies, the DFS becomes dominant and the SD diverges as f^{-2}, instead of $f^{-5/2}$. Before that, there is an intermediate regime where $M_{\min}$ is dominant and a short plateau exists. The comparison in fig. 2.2 (inset) between the phase quadratures FI and the QFI shows that they coincide at low

frequencies where the thermal noise is dominant but the QFI clearly outperforms the phase quadratures FI at intermediate frequencies where RPN is dominant.

2.6 Effect of Squeezing

We summarize the optimal schemes and sensitivities with squeezing. Given a squeezing factor of e^{-r} the optimal QFI is: $4\boldsymbol{\mathcal{V}}_{+,\mathrm{ph}}^{\dagger}\left(e^{-2r}\mathbb{1}+\delta^2 A_{\mathrm{ph}}A_{\mathrm{ph}}^{\dagger}\right)^{-1}\boldsymbol{\mathcal{V}}_{+,\mathrm{ph}}$, it can be achieved with squeezing of the phase quadratures and measuring the optimal quadratures of eq. (2.10). For phase quadratures measurement, the optimal FI is: $4\boldsymbol{\mathcal{V}}_{+,\mathrm{ph}}^{\dagger}\left(e^{-2r}\left(\mathbb{1}+M_{21}M_{21}^{\dagger}\right)+\delta^2 A_{\mathrm{ph}}A_{\mathrm{ph}}^{\dagger}\right)^{-1}\boldsymbol{\mathcal{V}}_{+,\mathrm{ph}}$, achievable by squeezing the optimal quadratures. These optimal squeezing quadratures and sensitivity bounds are derived in Appendix A.8.

The performance of the squeezed schemes, and comparison with the unsqueezed case, is shown in fig. 2.3. Observe that the gain from squeezing is not uniform and depends on the effectiveness of the DFI, i.e., on η. We can define the gain from squeezing as $\eta_{\mathrm{gain}}=\frac{F_{\mathrm{sq}}/F-1}{e^{2r}-1}$, where $F_{\mathrm{sq}}(F)$ is the FI with(out) squeezing. Clearly $0\leq\eta_{\mathrm{gain}}\leq 1$, where 0 corresponds to no gain and 1 to maximal gain. We show in the Appendix A.8 that in the limit of large displacement noise $\eta_{\mathrm{gain}}=\eta$, hence η_{gain} equals the fraction of information coming from the DFS. This is illustrated in the insets of fig. 2.3. DFI is therefore necessary to gain from squeezing in the presence of large displacement noise. The improvement introduced by DFI is summarized in fig. 2.3 (c) where we compare the sensitivity with squeezed input given different readout combinations: a combination that maximizes the signal and the optimal combination that saturates QFI. The sensitivity with optimal combination considerably outperforms the sensitivity with maximal-signal combination at low frequencies due to two DFI properties: better scaling with f (f^{-2} compared to $f^{-2.5}$), and larger gain from squeezing.

2.7 Extensions and Conclusions

The Appendix A.9 contains extensions of this triangular scheme to $n-$gons with n mirrors. Such polygon schemes may lead to further sensitivity improvement. The Appendix A.14 also contains an analysis of the Sagnac noise, i.e., a phase shift due to rotation. We show that the resulting sensitivity loss is small.

To conclude, we developed new DFI schemes and derived general quantum precision limits, optimal measurements, and optimal squeezing quadratures.

There are still several challenges and open questions. The main challenge is to incorporate suppression of laser noise in this architecture. The laser noise must be correlated between the different ports and the challenge is to engineer such correlation. Other challenges include further optimization over the architecture and considering detuning.

Chapter 3

LINEAR WAVEFORM ESTIMATION USING KALMAN FILTERS

3.1 Introduction

In advanced gravitational wave detectors, detuned signal recycling reshapes the spectral density of quantum noise and broadens the sensitive bandwidth without requiring a higher arm-cavity power [1, 67, 68]. This allows for enhancements in the detection of intermediate-mass black hole mergers [69], high-frequency gravitational wave signals up to a few kilohertz [70], and post-merger oscillations of hypermassive neutron stars [6]. However, detuning couples the GW signal into both amplitude and phase quadratures of the output light, rendering the readout a multi-parameter estimation problem.

In single-parameter estimation, the Quantum Cramér–Rao Bound (QCRB) sets a lower limit on the variance of any unbiased estimator, and can always be saturated in the asymptotic limit by a suitable measurement [71]. In multi-parameter scenarios, non-commutativity of optimal observables generally prevents simultaneous saturation of each individual QCRB; instead, the ultimate precision is governed by the more stringent Holevo Cramér–Rao Bound (HCRB), which accounts for measurement incompatibility [72, 73]. For detuned interferometry, this incompatibility leads to a gap between the naive single-parameter QCRB and the best joint sensitivity achievable for both quadratures [74]. This has recently been resolved by deriving the correct multi-parameter bound for detuned cavities and demonstrating that, by prioritizing one parameter (e.g., amplitude) over the conjugate (phase), one can exceed the balanced sensitivity by a factor of $\sqrt{2}$ [74].

Here, we propose and analyze a practical scheme to *attain* the single-parameter QCRB for an arbitrary chosen quadrature in a detuned interferometer, by employing real-time Bayesian filtering. Specifically, we show that Kalman filtering—either in its Extended (EKF) or Unscented (UKF) form—can be used to track the signal-induced displacement in one optical quadrature while treating the orthogonal quadrature as a disturbance. By continually updating a posterior for the target parameter — the filter sequentially refines the estimate — thereby saturating the QCRB for the parameter of interest. We simulate the estimation error and demonstrate that it

reaches the QCRB limit $\Delta^2|\hat{h}| = 1/(\mathcal{F}T)$, where $\mathcal{F}$ is the single-parameter quantum Fisher information for unit integration time and T is the total integration time.

To illustrate the utility of this approach, we apply it to a prototypical GW-detector configuration: a detuned Fabry–Pérot–Michelson interferometer with signal recycling. We calculate the quantum Fisher information for amplitude estimation in this system and show that the EKF/UKF scheme indeed attains $\Delta|h|_{EKF/UKF} = \Delta|h|_{QCRB}$. Our results demonstrate a novel synergy between quantum estimation theory and classical signal processing, opening a route to quantum-limited sensing in the multi-parameter regime.

3.2 Theory

We describe a gravitational-wave interferometer read out by homodyne detection in the two-photon formalism, which is directly generalizable to any homodyne measurement of a classical signal field [31, 75, 76]. A real gravitational-wave strain $h(t)$ induces phase modulation sidebands on the carrier field at frequencies $\omega_0 \pm \Omega$, whose annihilation operators we denote $\hat{a}(\pm\Omega)$. We define the corresponding *complex* quadrature operators

$$\hat{x}(\Omega) = \frac{\hat{a}(\Omega) + \hat{a}^\dagger(-\Omega)}{\sqrt{2}}, \quad \hat{p}(\Omega) = \frac{\hat{a}(\Omega) - \hat{a}^\dagger(-\Omega)}{i\sqrt{2}}. \tag{3.1}$$

By construction, $\hat{x}(-\Omega) = \hat{x}^\dagger(\Omega)$ and $\hat{p}(-\Omega) = \hat{p}^\dagger(\Omega)$, so each of $\hat{x}, \hat{p}$ carries both a real (cosine) and imaginary (sine) component.

In the absence of any signal, the interferometer output is held at a dark fringe so that the measured quadratures $\hat{x}_0(\Omega)$ and $\hat{p}_0(\Omega)$ contain only vacuum (and technical) noise, with one-sided spectral densities $\langle \hat{x}_0(\Omega)\hat{x}_0(-\Omega)\rangle = \langle \hat{p}_0(\Omega)\hat{p}_0(-\Omega)\rangle = \frac{1}{2}$ under our normalization [76]. Detailed derivations can be found in Appendix B.2.

A gravitational wave of Fourier component $h(\Omega) = h_c(\Omega) + ih_s(\Omega)$ (with h_c,h_s the in-phase and quadrature components) produces a displacement of the output quadratures. To linear order in h, we write

$$\begin{pmatrix} \hat{x}(\Omega) \\ \hat{p}(\Omega) \end{pmatrix} = \begin{pmatrix} \hat{x}_0(\Omega) \\ \hat{p}_0(\Omega) \end{pmatrix} + \vec{\chi}(\Omega)h(\Omega) \tag{3.2}$$

where the complex two-component *susceptibility vector*

$$\vec{\chi}(\Omega) = \begin{pmatrix} \chi_x(\Omega) \\ \chi_p(\Omega) \end{pmatrix} \tag{3.3}$$

encodes the interferometer's full linear response (optical cavity poles, mechanical transfer functions, potential optical springs, etc.) [15].

To work with real measurement observables, we decompose both quadratures and susceptibilities into their real and imaginary parts,

$$\hat{x}(\Omega) = \hat{x}_R(\Omega) + i\hat{x}_I(\Omega), \quad \chi_x(\Omega) = R_1(\Omega) + iI_1(\Omega), \tag{3.4}$$

and similarly

$$\hat{p}(\Omega) = \hat{p}_R(\Omega) + i\hat{p}_I(\Omega), \quad \chi_p(\Omega) = R_2(\Omega) + iI_2(\Omega). \tag{3.5}$$

We then form the normalized real-quadrature vector

$$\hat{\mathbf{q}}(\Omega) \equiv \frac{1}{\sqrt{T}} \begin{pmatrix} \hat{x}_R(\Omega) \\ \hat{p}_R(\Omega) \\ \hat{x}_I(\Omega) \\ \hat{p}_I(\Omega) \end{pmatrix}, \tag{3.6}$$

so that each component has vacuum variance $1/2$ and canonical commutators $[\hat{q}_i, \hat{q}_j] = i\Omega_{ij}$, where Ω follows the symplectic form in their real and imaginary counterparts independently.

In this real basis, the classical displacement due to the strain's in-phase (h_c) and quadrature (h_s) components becomes

$$\Delta\mathbf{q}(\Omega) = \sqrt{T}h_c(\Omega) \begin{pmatrix} R_1 \\ R_2 \\ I_1 \\ I_2 \end{pmatrix} + \sqrt{T}h_s(\Omega) \begin{pmatrix} -I_1 \\ -I_2 \\ R_1 \\ R_2 \end{pmatrix}. \tag{3.7}$$

Here, the pair (R_1, R_2) gives the displacements of the two cosine (in-phase) quadrature channels in response to the in-phase component of the strain, while (I_1, I_2) gives the displacements of the sine (quadrature) channels in response to the quadrature component. Together, the four coefficients R_1, R_2, I_1, I_2 completely specify how any real gravitational-wave signal produces outputs in the four real quadrature channels.

Although we specialize our discussion here to a gravitational-wave interferometer, this formalism—and in particular (eq. (3.1) to eq. (3.7))—applies generically to any homodyne measurement of a classical signal encoded in the sidebands of a bosonic field. The susceptibility vector $\vec{\chi}(\Omega)$ and its real/imaginary decomposition

can be obtained for other platforms (e.g., cavity optomechanical sensors, superconducting circuits) by following the same input–output analysis and linear response theory [15, 76]. Detailed derivations of the susceptibility functions are provided in Appendix B.1.

3.3 Filtering Approach

To estimate the signal parameters $|h|$ and ϕ in real time (where $h_c = |h|\cos\phi$ and $h_s = |h|\sin\phi$), we employ recursive Bayesian filters seeded by a heterodyne measurement. The heterodyne readout of both amplitude and phase quadratures provides an initial coarse estimate $\hat{\mathbf{x}}_0 = [|\hat{h}|_0, \hat{\phi}_0]^T$ with double the variance than would be expected if the optimal phase was known. It must be noted here that this measurement is not intended to be of the same duration as those of the filtering measurement that follow.

State Vector and Measurement Model

We use the state vector

$$\mathbf{x}_k = \begin{bmatrix} |\hat{h}|_k \\ \hat{\phi}_k \end{bmatrix} \tag{3.8}$$

where $\hat{\mathbf{x}}_k = [|\hat{h}|_k, \hat{\phi}_k]^T$ is our best estimate of the real magnitude and phase ($[|h|, \phi]^T$) after k time steps.

We assume here that the real parameters do not vary with time and can therefore represent their propagation before the filtering update as,

$$\mathbf{x}_{k+1|k} = \mathbf{x}_k\,. \tag{3.9}$$

To focus the filter on the parameter of interest, we choose two real measurement channels at each step k:

- Signal-aligned quadrature $y_{1,k}$: obtained by projecting the real-quadrature vector $\hat{\mathbf{q}}(\Omega)$ onto the current estimate of the signal displacement direction.
- Commutating quadrature $y_{2,k}$: a quadrature that is both commutating and orthogonal to the signal-aligned quadrature.

The derivations for these quadratures can be found in Appendices B.4 and B.5.

The measurement model, therefore, becomes

$$\begin{aligned} y_{1,k+1} &\sim \mathcal{N}\big(\sqrt{T}|\hat{h}|_{k+1|k} R_{\text{tot}} \cos(\phi_{meas} - \hat{\phi}_{k+1|k}), \tfrac{1}{2}\big), \\ y_{2,k+1} &\sim \mathcal{N}\big(\sqrt{T}|\hat{h}|_{k+1|k} M \sin(\phi_{meas} - \hat{\phi}_{k+1|k}), \tfrac{1}{2}\big), \end{aligned} \tag{3.10}$$

henceforward denoted as $\begin{pmatrix} y_{1,k+1} \\ y_{2,k+1} \end{pmatrix} = \mathbf{h}(\mathbf{x}_{k+1|k})$, and where,

$$R_{\text{tot}} \equiv \sqrt{R_1^2 + R_2^2 + I_1^2 + I_2^2}, \quad M \equiv \frac{R_1^2 - R_2^2 + I_1^2 - I_2^2}{R_{\text{tot}}}. \tag{3.11}$$

In this model ϕ_{meas} is set equal to $\hat{\phi}_k$ to tune the projections for the two measurements above.

By construction, $y_{1,k+1}$ collects the component of the signal displacement along the estimated direction $\vec{v}(\hat{\phi}_k)$, while $y_{2,k+1}$ measures the commutating-orthogonal component. As the filter refines $\hat{\phi}$, the projection basis aligns ever more closely with the true signal direction, making $y_{1,k+1}$ progressively approach the optimal single-parameter measurement and improving estimation efficiency. The noise in both channels remains Gaussian with variance $1/2$.

Extended Kalman Filter (EKF)

The measurement function $\mathbf{h}(\mathbf{x})$ in Eq. (3.10) is nonlinear in the state $\mathbf{x} = [|h|, \phi]^T$. To apply a Kalman filter, we therefore linearize $\mathbf{h}$ around our current estimate $\hat{\mathbf{x}}_{k+1|k}$. Since the filter maintains an estimate $\hat{\phi}_k$, we can expand

$$\mathbf{h}(\mathbf{x}) \approx \mathbf{h}(\hat{\mathbf{x}}_{k+1|k}) + H_{k+1}\big(\mathbf{x} - \hat{\mathbf{x}}_{k+1|k}\big), \tag{3.12}$$

where the Jacobian H_{k+1} is evaluated at $\hat{\mathbf{x}}_{k+1|k}$. Explicitly, using $\Delta\phi_{k+1} = \phi_{meas} - \hat{\phi}_{k+1|k}$

$$\begin{aligned} H_{k+1} &= \left.\frac{\partial \mathbf{h}}{\partial \mathbf{x}}\right|_{\hat{\mathbf{x}}_{k+1|k}} \\ &= \begin{pmatrix} \sqrt{T} R_{\text{tot}} \cos\Delta\phi_{k+1} & \sqrt{T}|\hat{h}|_{k+1|k} R_{\text{tot}} \sin\Delta\phi_{k+1} \\ \sqrt{T} M \sin\Delta\phi_{k+1} & -\sqrt{T}|\hat{h}|_{k+1|k} M \cos\Delta\phi_{k+1} \end{pmatrix} \\ &= \begin{pmatrix} \sqrt{T} R_{\text{tot}} & 0 \\ 0 & -\sqrt{T}|\hat{h}|_{k+1|k} M \end{pmatrix} \end{aligned} \tag{3.13}$$

where in the last step we use the fact $\phi_{meas} = \hat{\phi}_k$.

The EKF then proceeds with the standard prediction–update cycle:

$$K_{k+1} = P_{k+1|k} H_{k+1}^T \big(H_{k+1} P_{k+1|k} H_{k+1}^T + R\big)^{-1}, \tag{3.14}$$

$$\hat{\mathbf{x}}_{k+1|k+1} = \hat{\mathbf{x}}_{k+1|k} + K_{k+1}\big(\mathbf{y}_{k+1} - \mathbf{h}(\hat{\mathbf{x}}_{k+1|k})\big), \tag{3.15}$$

$$P_{k+1|k+1} = \big(I - K_{k+1} H_{k+1}\big) P_{k+1|k}. \tag{3.16}$$

Here $P_{k+1|k}$ and $P_{k+1|k+1}$ are the prior and posterior covariance matrices, and $R = \frac{1}{2} I$ is the measurement noise covariance. By re-linearizing at each step about the updated $\hat{\phi}$, the EKF maintains a locally valid Gaussian approximation to the posterior.

It must be noted here that the EKF is valid only under the assumption that our measurement model is linearizable. Therefore, the EKF filters performs well when it is initialized close to the real phase. In its absence, this filter cannot be reliably used to obtain the hidden state vector of our signal.

Unscented Kalman Filter (UKF)

The UKF provides a more accurate treatment of nonlinearity than the EKF by deterministically sampling the state distribution with a minimal set of *sigma points* that capture the true mean and covariance to third order [77, 78]. For our two-dimensional state $\mathbf{x} = [|h|, \phi]^T$, we generate $2n + 1 = 5$ points:

$$\chi_0 = \hat{\mathbf{x}}_{k+1|k}, \quad \chi_i = \hat{\mathbf{x}}_{k+1|k} \pm \Big[\sqrt{(n+\lambda) P_{k+1|k}}\Big]_i, i = 1, 2, \tag{3.17}$$

with $\lambda = \alpha^2(n + \kappa) - n$. Associated weights to calculate the mean and covariance ($W_i^m,\ W_i^c$) are described in eq. (B.67). Propagating through $\mathbf{h}$:

$$\begin{aligned} y_i &= \mathbf{h}(\chi_i), \\ \bar{\mathbf{y}} &= \sum_i W_i^m y_i, \\ P_{yy} &= \sum_i W_i^c (y_i - \bar{\mathbf{y}})(y_i - \bar{\mathbf{y}})^T + R, \\ P_{xy} &= \sum_i W_i^c (\chi_i - \bar{\mathbf{x}}_{k+1|k})(y_i - \bar{\mathbf{y}})^T, \\ K &= P_{xy} P_{yy}^{-1}. \end{aligned} \tag{3.18}$$

The state and covariance updates then follow

$$\begin{aligned} \hat{\mathbf{x}}_{k+1|k+1} &= \hat{\mathbf{x}}_{k+1|k} + K(\mathbf{y}_{k+1} - \bar{\mathbf{y}}), \\ P_{k+1|k+1} &= P_{k+1|k} - K P_{yy} K^T. \end{aligned} \tag{3.19}$$

This method avoids explicit Jacobians and often yields faster, more accurate convergence than the EKF in our nonlinear measurement scenario.

By capturing the true nonlinear transformation of the state distribution without explicit Jacobians, the UKF often achieves higher accuracy than the EKF. We employ the same process–noise and measurement–noise assumptions as in the EKF, and choose $\alpha = 10^{-3}, \beta = 2, \kappa = 0$ to balance numerical stability and approximation fidelity [78].

Bayesian Benchmarking

For performance comparison, we implement a recursive Bayesian estimator (in the form of a particle filter) that computes the posterior $p(\mathbf{x}_{k+1} \mid \mathbf{y}_{1:k+1})$ without Gaussian approximations [79]. Its computational cost precludes real-time use but provides a benchmark for filter optimality.

3.4 Numerical Simulations

In this section, we assess how well the EKF, UKF, and particle filter (PF) track the amplitude $|h|$ and phase ϕ of the gravitational-wave signal in real time. We compare their precision and accuracy against two benchmarks: the optimal single-parameter homodyne measurement (the QCRB limit for $|h|$) and a heterodyne readout. All filters are seeded by heterodyne measurement and then iteratively updated using the filters described in the section above.

To perform these simulations, we use a detuning of $\Delta = 2\pi \times 3\ kHz$ and a signal frequency set at $\Omega = 0.75\Delta$ — as signals in the 1–4kHz range can provide us information on the post-merger remanants of binary neutron star mergers [6, 8, 74, 80–86]. We also use a half-width at half-maximum readout rate of $2\pi \times 42\ Hz$ and an effective coupling rate of 1 between the signal and cavity modes to determine our susceptibility matrix.

In our simulations, we seed our filters with heterodyne measurements such that the $\frac{\Delta|h|}{|h|} \sim 0.1$, i.e., 10% noise level after this measurement. While we do not present the plots here for scenarios where the error is higher in the heterodyne readout, it readily follows from our discussions above that it would cause the EKF to be unreliable as the linearizability of the measurement function no longer holds and UKF would take significantly longer to converge — with convergence not being guaranteed in finite integration time.

We compare the efficacy of our filters in the regime described above using three different integration times for each filter, i.e., integrating with time steps at T, 10 T, and 100 T. This means that when a filter uses a shorter integration time, it uses a measurement with a higher noise level but makes multiple corrections of its state vector estimate. On the other hand, when using a longer integration time, each measurement has lower error, but we can make fewer updates for a signal of the same time duration. As our time parameter is scaled, we have presented our plots as a function of our measurements' Signal to Noise Ratio (SNR).

Using Fig. 3.1, we can see that all the filters asymptotically saturate the QCRB irrespective of the integration length per step. Key differences arise in the the total integration time required to achieve saturation, i.e., shorter time steps acheive this bound faster than longer time lengths. However, time steps of length T and 10T do not show significant difference in their performance. Additionally, in the RMSE of these measurements, shorter integration time leads to more fluctuations as the noise levels tend towards the optimal noise bound.

Next, we verify that the filters' internal uncertainty estimates match their actual RMSE in $|h|$. In fig. 3.2, the close overlap between each filter's estimated standard deviation and its empirical RMSE indicates that both linearization and sampling used in EKF and UKF methods are effective in correctly estimating the error levels. The predicted and observed errors are statistically indistinguishable. Further, both filters saturate the optimal filtering benchmark created using the Particle Filter.

Finally, fig. 3.3 compares the RMSE trajectories of all filters against the single-parameter QCRB for both $|h|$ and ϕ. The left panel of fig. 3.3 shows that all filters drive the RMSE in $|h|$ to asymptotically approach the QCRB, confirming that the QCRB can be effectively attained. In contrast, the right panel reveals that the RMSE in ϕ remains far above its QCRB, highlighting the inevitable sacrifice of phase precision. This behavior underscores our central result: by focusing measurement and estimation resources via filtering on a single quadrature, one can reach the quantum-limited sensitivity for amplitude at the expense of increased phase uncertainty.

3.5 Conclusions

We have demonstrated that real-time Bayesian filters—specifically the EKF and UKF—can be used to *attain* the single-parameter Quantum Cramér–Rao Bound (QCRB) for the amplitude quadrature of a detuned interferometric signal, by effec-

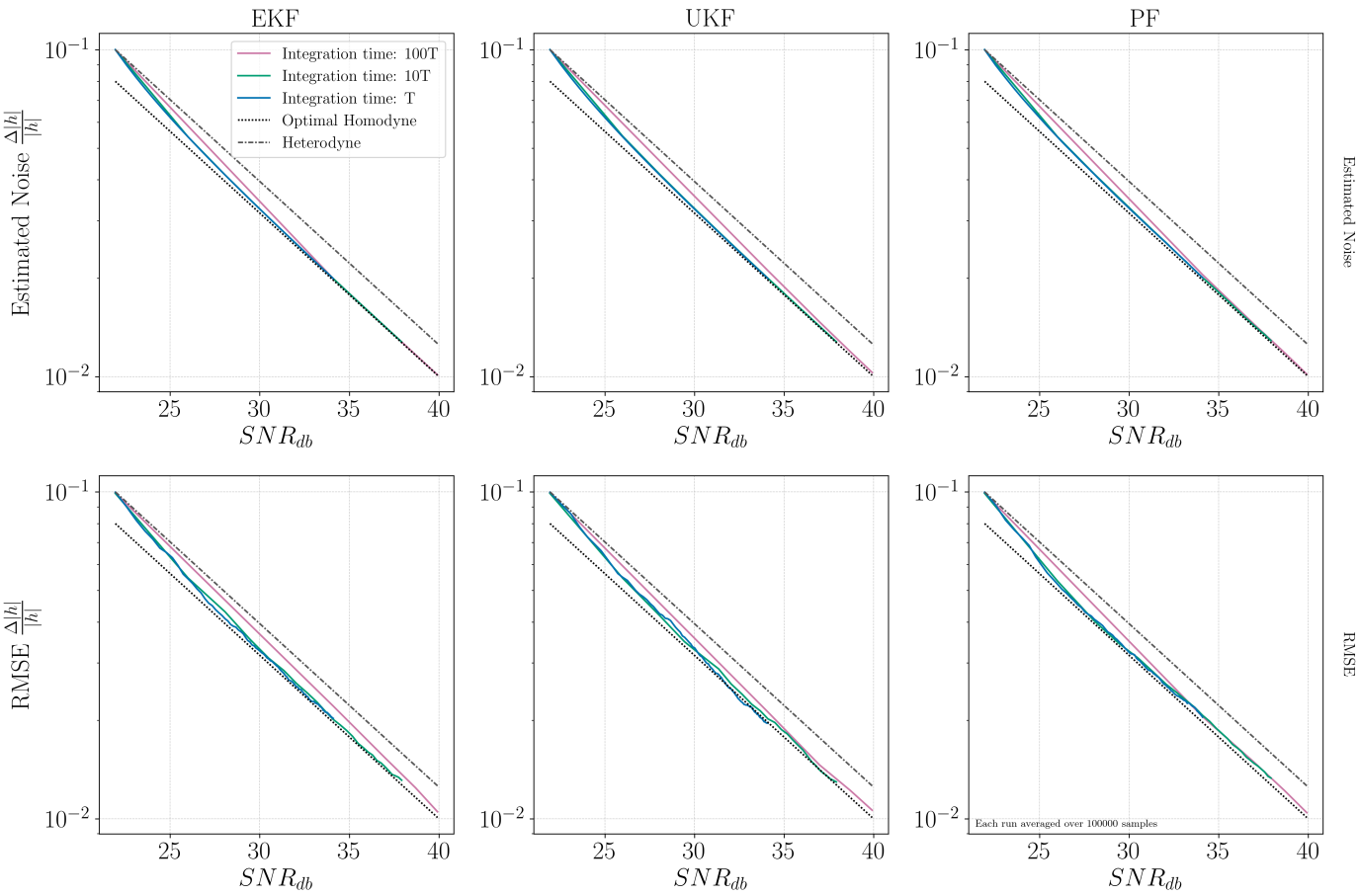

Figure 3.1: Filter performance with varied time steps. Top row: Estimated uncertainty $\Delta|h|/|h|$ predicted by each filter as a function of measurement SNR (in dB) for the extended Kalman filter (EKF, left), unscented Kalman filter (UKF, center), and particle filter (PF, right). Colored curves correspond to integration intervals of T (blue), $10T$ (green), and $100T$ (magenta), while the black dotted line shows the optimal single-parameter homodyne limit and the grey dash–dotted line the heterodyne baseline.Bottom row: Empirical RMSE under the same conditions and for the same integration times and benchmarks. All filters approach the homodyne bound at high SNR; shorter integration times yield larger fluctuations around the optimal noise level but enable more rapid convergence to the ultimate sensitivity. Curves are averaged over 10^6 Monte Carlo samples.

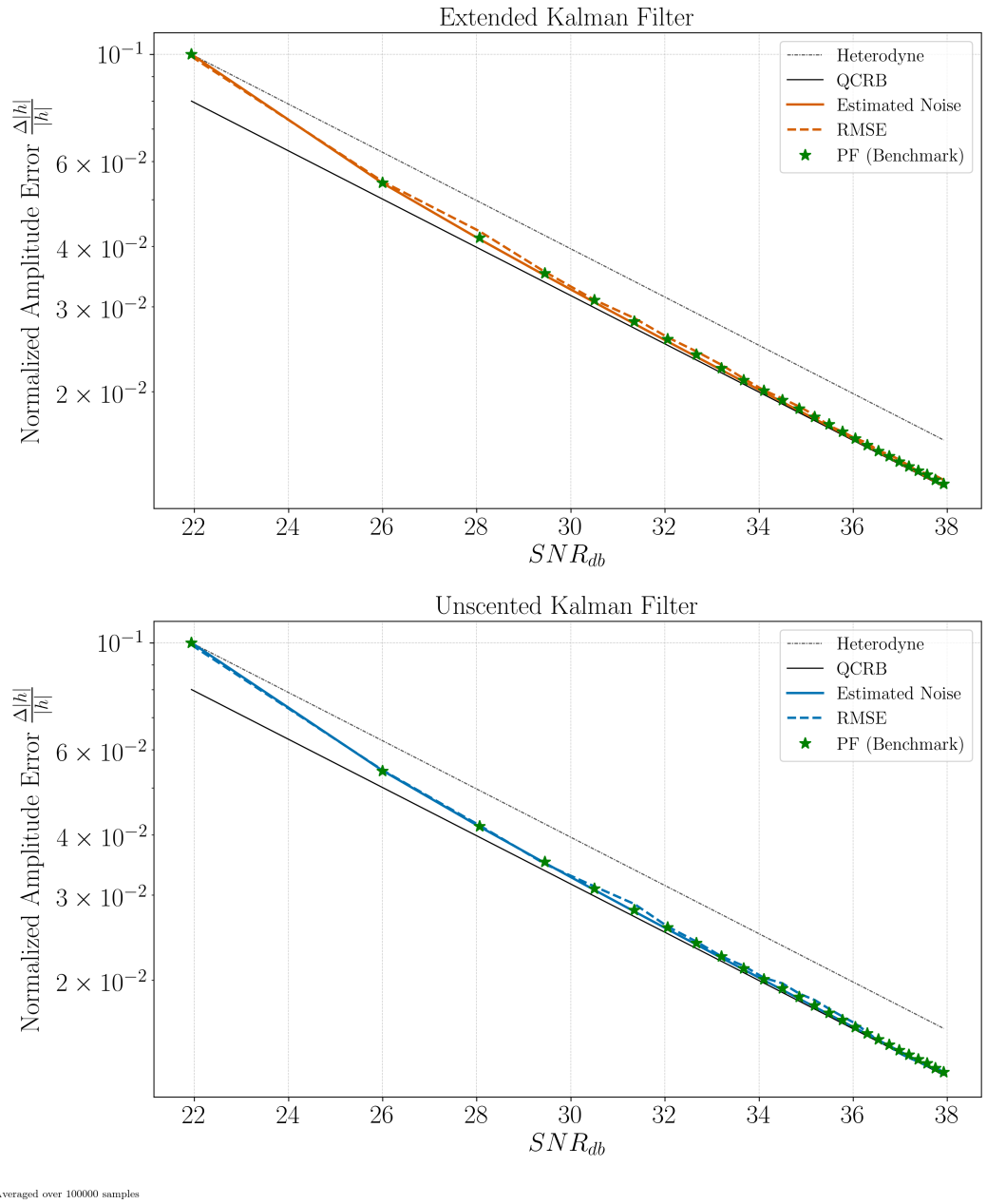

Figure 3.2: Comparison of each filter's internal estimated uncertainty (solid colored lines) against its empirical RMSE (dashed colored lines) as a function of measurement SNR (in dB), shown separately for the extended Kalman filter (EKF, top panel) and unscented Kalman filter (UKF, bottom panel). Also plotted are the heterodyne readout baseline (grey dash–dotted), the single-parameter QCRB (solid black), and the particle-filter benchmark (gold dotted). The near-perfect overlap between estimated noise, empirical RMSE, and the PF benchmark demonstrates that both EKF and UKF not only accurately quantify their own error but also saturate the optimal performance of the particle filter across the entire SNR range. Results are averaged over 10^6 Monte Carlo trials.

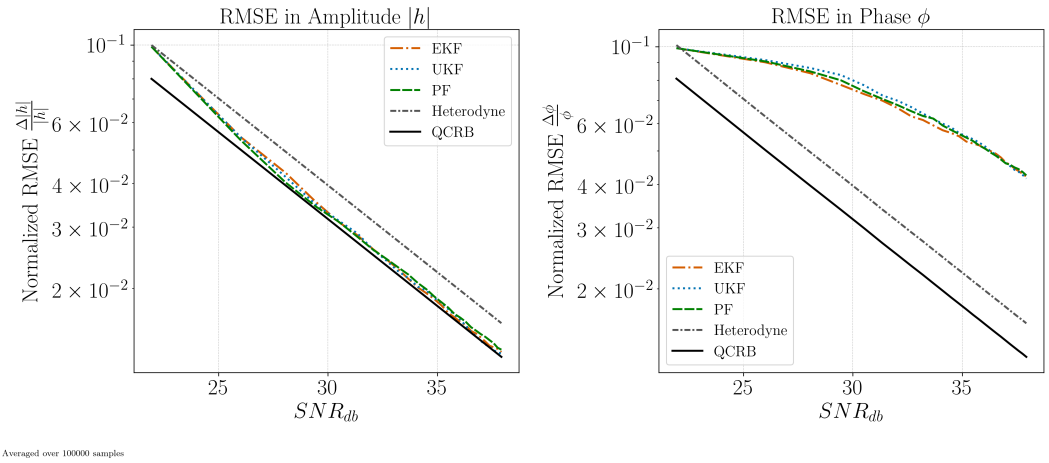

Figure 3.3: Normalized RMSE in the amplitude $|h|$ (left) and phase ϕ (right) of the gravitational-wave signal as a function of measurement SNR (in dB). Curves show the performance of the extended Kalman filter (EKF, orange dash–dotted), unscented Kalman filter (UKF, blue dotted), particle filter (PF, yellow dashed), the heterodyne readout baseline (grey dash–dotted), and the single-parameter QCRB (solid black). Results are averaged over 10^6 Monte Carlo samples. All filters asymptotically attain the amplitude QCRB at high SNR, while phase estimation remains significantly above its QCRB across the entire SNR range.

tively treating the orthogonal quadrature as a disturbance. In our simulations the RMSE in $|h|$ closely approaches $\Delta^2|\hat{h}| = 1/(\mathcal{F}T)$, while the phase error remains above the heterodyne level. This trade-off is a direct consequence of quantum estimation theory: a single-parameter QCRB may always be saturated asymptotically [71], but simultaneous saturation of incompatible observables is forbidden by the Holevo bound [72–74].

Importantly, the filtering strategy is entirely general to any homodyne measurement of a linear displacement in a bosonic field. Whether in cavity optomechanical force sensing, trapped-ion motional tomography, spin-ensemble magnetometry, or superconducting microwave resonators, one may track a chosen quadrature with an EKF/UKF to reach its QCRB solely via classical post-processing of the continuous measurement record. No quantum-nondemolition interaction or injected squeezing is required, making the method directly compatible with existing experimental platforms.

Looking forward, integrating this filtering framework with *adaptive* control—e.g., real-time feedback on the local oscillator phase—could further enhance tracking of time-varying waveforms. The formalism also extends naturally to explicitly

dynamical signals by employing state-space models with known evolution laws [15]. Overall, our work underscores the synergy between quantum-limited measurement and classical estimation theory, charting a path to quantum-optimal sensing across a broad range of applications.

Appendix A

SUPPLEMENTAL MATERIAL FOR DISPLACEMENT-NOISE FREE INTERFEROMETERS

A.1 Two-Photon Formalism

Assuming an initial phase of 0, an EM field can be written as [58]:

$$\hat{E}(t) = (A(t) + \hat{a}_1(t))\cos(\omega_0 t) + \hat{a}_2(t)\sin(\omega_0 t) \tag{A.1}$$

where $\hat{a}_{1,2}(t)$ are the Hermitian amplitude and phase quadrature operators, respectively. They describe the amplitude and phase modulation of the field (ω_0 is the carrier frequency). They satisfy $\langle \hat{a}_{1,2}(t) \rangle = 0$ and their commutation relations are given by:

$$[\hat{a}_1(t), \hat{a}_2(t')] = -i\delta(t - t'). \tag{A.2}$$

We can further define $\hat{a}_{1,2}(\Omega)$ as the Fourier transform of $\hat{a}_{1,2}(t)$:

$$\hat{a}_{1,2}(\Omega) = \frac{1}{\sqrt{2\pi}} \int \hat{a}_{1,2}(t)\, e^{-i\Omega t} \mathrm{dt}. \tag{A.3}$$

Here, we observe that $\hat{a}_{1,2}(\Omega)$ are not Hermitian but they commute with the Hermitian conjugate of themselves. This means that they have an orthonormal eigenbasis but their eigenvalues are complex. Therefore, the commutation relations between them is given by:

$$\left[\begin{pmatrix} \hat{a}_1 \\ \hat{a}_2 \end{pmatrix}, \left(\hat{a}_1^\dagger, \hat{a}_2^\dagger \right) \right] := \begin{pmatrix} [\hat{a}_1, \hat{a}_1^\dagger] & [\hat{a}_1, \hat{a}_2^\dagger] \\ [\hat{a}_2, \hat{a}_1^\dagger] & [\hat{a}_2, \hat{a}_2^\dagger] \end{pmatrix} = i \begin{pmatrix} 0 & 1 \\ -1 & 0 \end{pmatrix}, \tag{A.4}$$

where the Ω dependence is suppressed, and we used the following notation for the commutation relations matrix: $\left[\hat{\mathbf{Q}}, \hat{\mathbf{Q}}^\dagger\right] := \left(\left[\hat{Q}_i, \hat{Q}_j\right] \right)_{i,j}$. Hereafter we will use this notation.

Therefore, we can interpret the above as two harmonic oscillators with:

$$\begin{aligned} \hat{X}_R(\Omega) &= \sqrt{2}\mathrm{Re}(\hat{a}_1), \quad \hat{P}_R(\Omega) = \sqrt{2}\mathrm{Re}(\hat{a}_2), \\ \hat{X}_I(\Omega) &= \sqrt{2}\mathrm{Im}(\hat{a}_1), \quad \hat{P}_I(\Omega) = \sqrt{2}\mathrm{Im}(\hat{a}_2). \end{aligned} \tag{A.5}$$

It follows that the commutation relations of two harmonic oscillators are given by:

$$\left[\begin{pmatrix} \hat{X}_R \\ \hat{P}_R \\ \hat{X}_I \\ \hat{P}_I \end{pmatrix}, \begin{pmatrix} \hat{X}_R, \hat{P}_R, \hat{X}_I, \hat{P}_I \end{pmatrix}\right] = \begin{pmatrix} \sigma_y & 0 \\ 0 & \sigma_y \end{pmatrix}, \tag{A.6}$$

where $\sigma_{x/y}$ are the Pauli X/Y matrices and the Ω dependence is suppressed.

In a multichannel interferometer, we have a vector of input quadratures $\hat{\mathbf{Q}} = \begin{pmatrix} \hat{\mathbf{a}}_1, \hat{\mathbf{a}}_2 \end{pmatrix}^T$, which defines a vector of Hermitian quadratures (position and momentum operators) given by $\hat{\mathbf{S}} = \begin{pmatrix} \hat{\mathbf{X}}_R, \hat{\mathbf{P}}_R, \hat{\mathbf{X}}_I, \hat{\mathbf{P}}_I \end{pmatrix}^T$.

A.2 Quantum Fisher Information Matrix

This section derives eq. (2.3) in the main text and generalizes it to the case of multi-parameter estimation of $\mathbf{h}$. This requires using the Quantum Fisher Information Matrix (QFIM) which lower bounds the covariance matrix of the estimators of $\mathbf{h}$: $\mathrm{COV}(\mathbf{h}) \geq \mathcal{I}^{-1}$.

In a multichannel interferometer, the output sideband fields are given by

$$\hat{\mathbf{Q}}_{\text{out}} = \begin{pmatrix} \hat{\mathbf{b}}_1(\Omega) \\ \hat{\mathbf{b}}_2(\Omega) \end{pmatrix} \tag{A.7}$$

with commutation relations:

$$\left[\begin{pmatrix} \hat{\mathbf{b}}_1 \\ \hat{\mathbf{b}}_2 \end{pmatrix}, \left(\hat{\mathbf{b}}_1^\dagger, \hat{\mathbf{b}}_2^\dagger\right)\right] = i \begin{pmatrix} 0 & \mathbb{1}_k \\ -\mathbb{1}_k & 0 \end{pmatrix} \tag{A.8}$$

where k is the number of output fields and the Ω dependence is suppressed.

As above, the Hermitian quadratures are:

$$\hat{\mathbf{S}} = \begin{pmatrix} \hat{\mathbf{X}}_R \\ \hat{\mathbf{P}}_R \\ \hat{\mathbf{X}}_I \\ \hat{\mathbf{P}}_I \end{pmatrix} = \sqrt{2} \begin{pmatrix} \mathrm{Re}\left(\hat{\mathbf{b}}_1\right) \\ \mathrm{Re}\left(\hat{\mathbf{b}}_2\right) \\ \mathrm{Im}\left(\hat{\mathbf{b}}_1\right) \\ \mathrm{Im}\left(\hat{\mathbf{b}}_2\right) \end{pmatrix}, \tag{A.9}$$

which is the corresponding quadratures vector of $2k$ harmonic oscillators.

Given the input-output relations of $\hat{\mathbf{Q}}$ (eq. (2.1)), these relations for $\hat{\mathbf{S}}$ are given by:

$$\hat{\mathbf{S}}_{\text{out}} = M' \hat{\mathbf{S}}_{\text{in}} + \mathcal{V}' \mathbf{h}' + A' \mathbf{\Delta x}', \tag{A.10}$$

where for all complex vectors $u(= \mathbf{h}, \mathbf{\Delta x})$, we have $u' = \sqrt{2}\begin{pmatrix} \mathrm{Re}\,(u) \\ \mathrm{Im}\,(u) \end{pmatrix}$ and for all complex matrices $\mathcal{M}(= M, \mathcal{V}, A)$ we have $\mathcal{M}' = \begin{pmatrix} \mathrm{Re}\,(\mathcal{M}) & -\mathrm{Im}\,(\mathcal{M}) \\ \mathrm{Im}\,(\mathcal{M}) & \mathrm{Re}\,(\mathcal{M}) \end{pmatrix}$. $\mathbf{h}, \mathbf{\Delta x}, M, \mathcal{V}$ and A are as defined in the main text. Note that we expanded the complex-valued vector of parameters, $\mathbf{h}$, to the real-valued vector $\mathbf{h}'$, which consists of 4 parameters: $\mathrm{Re}\,(h_+)\,, \mathrm{Im}\,(h_+)\,, \mathrm{Re}\,(h_\times)\,, \mathrm{Im}\,(h_\times)$.

Since we consider an initial Gaussian state and the evolution is through a Gaussian channel, the final state of the output modes is also Gaussian and can be characterized by:

$$\begin{aligned} \mathbf{d_s}\,(\mathbf{h}') &= \langle \hat{\mathbf{S}} \rangle \\ \Sigma_{i,j} &= \frac{1}{2}\langle \hat{S}_i \hat{S}_j + \hat{S}_j \hat{S}_i \rangle - \langle \hat{S}_i \rangle \langle \hat{S}_j \rangle \end{aligned} \tag{A.11}$$

where all the information about $\mathbf{h}'$ is encoded in the first moment vector $\mathbf{d_s}(\mathbf{h}')$ (mean vector) and Σ is the covariance matrix.

The Quantum Fisher Information Matrix (QFIM) about $\mathbf{h}'$ can be expressed using these first two moments [37, 63]:

$$\mathcal{I}_{\mathbf{h}'} = 2(\partial_{\mathbf{h}'}\mathbf{d_s})^T \Sigma^{-1} (\partial_{\mathbf{h}'}\mathbf{d_s}) = 2\mathcal{V}'^{\dagger}\Sigma^{-1}\mathcal{V}', \tag{A.12}$$

where we used the fact that the state is Gaussian, that all the information is encoded in $\mathbf{d_s}$, and that $\partial_{\mathbf{h}'}\mathbf{d_s} = \mathcal{V}'$.

In the following subsection, we will show that the QFIM can be expressed in a more compact form involving only the mean values of $\hat{\mathbf{Q}}$ ($\mathbf{d_q}$), and the covariance matrix of $\hat{\mathbf{Q}}$ (Σ_q).

Complex Compact Form of the QFIM

In this subsection, we show that eq. (2.3) is a compact form of eq. (A.12).

Following ref. [62], let us first introduce the notion of circular symmetry of real matrices. A real symmetric matrix A has a circular symmetry if it takes the form of:

$$A = \begin{pmatrix} A' & -\bar{A} \\ \bar{A} & A' \end{pmatrix}. \tag{A.13}$$

If A satisfies this symmetry then we can define its complex-compact form: $A_c = A' + i\bar{A}$. This mapping between complex Hermitian matrices and real symmetric

matrices with this symmetry $M \leftrightarrow \begin{pmatrix} \mathrm{Re}\,(M) & -\mathrm{Im}\,(M) \\ \mathrm{Im}\,(M) & \mathrm{Re}\,(M) \end{pmatrix}$ is a homomorphism, i.e., it preserves multiplication:

$$A_c = B_c C_c \Longleftrightarrow \begin{pmatrix} A' & -\bar{A} \\ \bar{A} & A' \end{pmatrix} = \begin{pmatrix} B' & -\bar{B} \\ \bar{B} & B' \end{pmatrix} \begin{pmatrix} C' & -\bar{C} \\ \bar{C} & C' \end{pmatrix}. \tag{A.14}$$

As a result, identity is mapped to identity:

$$\mathbb{1}_k \longleftrightarrow \begin{pmatrix} \mathbb{1}_k & 0 \\ 0 & \mathbb{1}_k \end{pmatrix} = \mathbb{1}_{2k} \tag{A.15}$$

and $\left(A^{-1}\right)_c = A_c^{-1}$.

Let us now prove the following claim:
If the covariance matrix of the estimators of (real-valued) $\mathbf{h}'$ *has a circular symmetry, i.e., it takes the form of:*

$$COV\,(\mathbf{h}') = \begin{pmatrix} C' & -\bar{C} \\ \bar{C} & C' \end{pmatrix}, \tag{A.16}$$

then the covariance matrix of the estimators of (complex-valued) $\mathbf{h}$ *is the complex-compact form of* $COV\,(\mathbf{h}')$*:*

$$COV\,(\mathbf{h}) = C' + i\bar{C}. \tag{A.17}$$

Proof: To show this we need to show that for any $h_\phi = \cos(\phi)\, h_+ + \sin(\phi)\, h_\times$:

$$\frac{1}{2}\mathrm{var}\left(\mathrm{Re}\left(h_\phi\right)\right) + \frac{1}{2}\mathrm{var}\left(\mathrm{Im}\left(h_\phi\right)\right) = u_\phi^T \left(C' + i\bar{C}\right) u_\phi, \tag{A.18}$$

with $u_\phi = \begin{pmatrix} \cos\phi & \sin\phi \end{pmatrix}^T$. Given the circular symmetry of COV $(\mathbf{h}')$, we observe that

$$\mathrm{var}\left(\mathrm{Re}\left(h_\phi\right)\right) = \mathrm{var}\left(\mathrm{Im}\left(h_\phi\right)\right) = u_\phi^T C' u_\phi. \tag{A.19}$$

Since $\bar{C}$ is anti-symmetric $u_\phi^T \left(\bar{C}\right) u_\phi = 0$, and thus eq. (A.18) is satisfied. Note that we could omit $\bar{C}$, but we keep it for brevity of notation afterwards.

This immediately implies that if $\mathcal{I}_{\mathbf{h}'}$ satisfies a circular symmetry:

$$\mathcal{I}_{\mathbf{h}'} = \begin{pmatrix} \mathcal{I}' & -\bar{\mathcal{I}} \\ \bar{\mathcal{I}} & \mathcal{I}' \end{pmatrix}, \tag{A.20}$$

then the Cramér-Rao bound for COV ($\mathbf{h}$) is given by the complex-compact form of $\mathcal{I}_{\mathbf{h}'}$: COV ($\mathbf{h}$) $\geq \left(\mathcal{I}' + i\bar{\mathcal{I}}\right)^{-1}$, i.e., the QFIM about $\mathbf{h}$ is given by:

$$\mathcal{I} = \mathcal{I}' + i\bar{\mathcal{I}}\,. \tag{A.21}$$

Observe that by definition $\mathcal{V}'$ satisfies this circular symmetry. Hence if Σ satisfies it:

$$\Sigma = \begin{pmatrix} \Sigma' & -\bar{\Sigma} \\ \bar{\Sigma} & \Sigma' \end{pmatrix}, \tag{A.22}$$

then $\mathcal{I}_{\mathbf{h}'}$ (eq. (A.12)) also satisfies it. Therefore given that Σ has a circular symmetry the QFIM about $\mathbf{h}$ reads:

$$\mathcal{I} = 2\mathcal{V}^{\dagger}\Sigma_c^{-1}\mathcal{V}, \tag{A.23}$$

where Σ_c is the complex compact form of Σ:

$$\Sigma_c = \Sigma' + i\bar{\Sigma}. \tag{A.24}$$

The covariance matrix of $\hat{\mathbf{Q}}$ is defined as:

$$\left(\Sigma_q\right)_{i,j} = \frac{1}{2}\left\langle\left\{\hat{Q}_i, \hat{Q}_j^{\dagger}\right\}\right\rangle - \langle\hat{Q}_i\rangle\langle\hat{Q}_j^{\dagger}\rangle, \tag{A.25}$$

with $\left\{\hat{Q}_i, \hat{Q}_j^{\dagger}\right\} := \hat{Q}_i\hat{Q}_j^{\dagger} + \hat{Q}_j^{\dagger}\hat{Q}_i$ being the anti-commutator of $\hat{Q}, \hat{Q}_j^{\dagger}$.

Given that Σ satisfies the circular symmetry then,

$$\mathrm{COV}\left(\mathrm{Re}\left(\hat{Q}_i\right), \mathrm{Re}\left(\hat{Q}_j\right)\right) = \mathrm{COV}\left(\mathrm{Im}\left(\hat{Q}_i\right), \mathrm{Im}\left(\hat{Q}_j\right)\right), \tag{A.26}$$

$$\mathrm{COV}\left(\mathrm{Re}\left(\hat{Q}_i\right), \mathrm{Im}\left(\hat{Q}_j\right)\right) = -\mathrm{COV}\left(\mathrm{Im}\left(\hat{Q}_i\right), \mathrm{Re}\left(\hat{Q}_j\right)\right). \tag{A.27}$$

Hence:

$$\left(\Sigma_q\right)_{i,j} = \mathrm{Cov}\left(\hat{Q}_i\hat{Q}_j^{\dagger}\right) \tag{A.28}$$

$$= 2\left[\mathrm{COV}\left(\mathrm{Re}\left(\hat{Q}_i\right)\mathrm{Re}\left(\hat{Q}_j\right)\right) + i\mathrm{COV}\left(\mathrm{Im}\left(\hat{Q}_i\right)\mathrm{Re}\left(\hat{Q}_j\right)\right)\right] \tag{A.29}$$

$$= \left(\Sigma_c\right)_{i,j}\,. \tag{A.30}$$

We can thus write $\mathcal{I}$ as:

$$\mathcal{I} = 2\mathcal{V}^{\dagger}\Sigma_q^{-1}\mathcal{V}. \tag{A.31}$$

.

This symmetry of the covariance matrix is satisfied in our problem given that the displacement noise process is stationary (see Appendix A.5 for details). The initial state is a coherent state, hence $\Sigma_i = \frac{1}{2}\mathbb{1}$, and the symmetry for this state is satisfied. In the interferometer, it undergoes a Gaussian channel which maps the covariance matrix to:

$$\Sigma = \mathcal{R}\Sigma_i\mathcal{R}^\dagger + \Lambda, \tag{A.32}$$

where $\mathcal{R} = \begin{pmatrix} \mathrm{Re}\,(M) & -\mathrm{Im}\,(M) \\ \mathrm{Im}\,(M) & \mathrm{Re}\,(M) \end{pmatrix}$ with M being the transfer matrix. Λ is due to classical displacement noise (thermal, seismic, etc.). Given that the classical displacement noise is stationary i.i.d Λ takes the form of (see Appendix A.5): $\Lambda = \frac{\delta^2}{2}\begin{pmatrix} \mathrm{Re}\left(AA^\dagger\right) & -\mathrm{Im}\left(AA^\dagger\right) \\ \mathrm{Im}\left(AA^\dagger\right) & \mathrm{Re}\left(AA^\dagger\right) \end{pmatrix}$, with A being the transfer matrix of the displacement noise. Since $\mathcal{R}, \Sigma_0, \Lambda$ satisfy this symmetry, Σ also satisfies this symmetry and we can thus use:

$$\Sigma_q = \frac{1}{2}MM^\dagger + \frac{\delta^2}{2}AA^\dagger. \tag{A.33}$$

Inserting this into eq. (A.31) yields:

$$\mathcal{I} = 4\mathcal{V}^\dagger\left(MM^\dagger + \delta^2 AA^\dagger\right)^{-1}\mathcal{V}. \tag{A.34}$$

We observe (from numerics) that the eigenvector of $\mathcal{I}$ with maximal eigenavalue corresponds to h_+, hence this is the polarization with maximal sensitivity. Focusing on this maximal sensitivity polarization reduces the problem to a single complex parameter estimation of h_+, and thus the quantity of interest is the QFI about h_+. The single parameter QFI (I) is a special case of the multi-parameter QFIM and thus reads:

$$I = 2\mathcal{V}_+^\dagger\Sigma_q^{-1}\mathcal{V}_+ = 4\mathcal{V}_+^\dagger\left(MM^\dagger + \delta^2 AA^\dagger\right)^{-1}\mathcal{V}_+. \tag{A.35}$$

These are the expressions in eqs. (2.3) and (2.5).

Hereafter, we will focus mainly on the single parameter estimation of h_+, and will thus use this QFI expression.

A.3 Fisher Information with Homodyne Measurement

For $2k$ output quadratures $\hat{\mathbf{Q}}_{\text{out}} = \begin{pmatrix} \hat{\mathbf{b}}_1 \\ \hat{\mathbf{b}}_2 \end{pmatrix}$, let us consider a homodyne measurement of these $l \leq k$ *commuting* quadratures: $T_h^\dagger \hat{\mathbf{Q}}_{\text{out}}$, where T_h is a $2k \times l$ matrix. The outcomes of this measurement have a l-dimensional complex Gaussian distribution with a mean vector $\sqrt{2}T_h^\dagger \mathcal{V}$ and a covariance matrix $\sigma_h = T_h^\dagger \Sigma_q T_h$.

The Fisher information (FI) about h_+ is therefore [37]:

$$F = 2\mathcal{V}_+^\dagger T_h \left(T_h^\dagger \Sigma_q T_h\right)^{-1} T_h^\dagger \mathcal{V}_+. \tag{A.36}$$

The space of qudrature operators is a $2k$-dimensional linear space. For convenience, we can represent these operators as $2k$-dimensional column vectors. A single quadrature $\mathbf{u}^\dagger \hat{\mathbf{Q}}_{\text{out}}$ is represented by the (column) vector $\mathbf{u}$, and our l quadrature, $T_h^\dagger \hat{\mathbf{Q}}_{\text{out}}$, are represented by the l column vectors of the matrix T_h. We then denote the projection operator onto the l measured quadratures as Π_h, observe that $\Pi_h = T_h T_h^\dagger$.

We now show that this FI can be decomposed into the sum of the FI's of different subspaces of Π_h. Let us decompose Π_h into orthogonal subspaces $\Pi_h = \sum_i \Pi_{h_i}$, and denote the FI given measurement of Π_{h_i} quadratures as F_i : $F_i = 2\mathcal{V}_+^\dagger T_{h_i} \left(T_{h_i}^\dagger \sigma_h T_{h_i}\right)^{-1} T_{h_i}^\dagger \mathcal{V}_+$. Given that σ_h is block diagonal in this decomposition, then the measurements of Π_{h_i} are statistically independent and thus $F = \sum_i F_i$. Formally:

$$F \overset{*}{=} 2\mathcal{V}_+^\dagger \left(\sum_i \Pi_{h_i} \sigma_h \Pi_{h_i}\right)^{-1} \mathcal{V}_+ \overset{\#}{=} \sum_i 2\mathcal{V}_+^\dagger T_{h_i} \left(T_{h_i}^\dagger \sigma_h T_{h_i}\right)^{-1} T_{h_i}^\dagger \mathcal{V}_+ = \sum_i F_i \tag{A.37}$$

where $(*)$ is due to the fact that it is block diagonal and $(\#)$ is basically:

$$\begin{pmatrix} \mathcal{V}_1^\dagger & \mathcal{V}_2^\dagger & \cdots & \mathcal{V}_j^\dagger \end{pmatrix} \begin{pmatrix} \boxed{\sigma_1} & & & \\ & \boxed{\sigma_2} & & \\ & & \ddots & \\ & & & \boxed{\sigma_j} \end{pmatrix}^{-1} \begin{pmatrix} \mathcal{V}_1 \\ \mathcal{V}_2 \\ \vdots \\ \mathcal{V}_j \end{pmatrix} = \sum_i \mathcal{V}_i^\dagger \sigma_i^{-1} \mathcal{V}_i. \tag{A.38}$$

We can use this fact to analyze DFI schemes. For example, for phase quadratures measurement, the displacement free subspace (DFS) is an eigenspace of the covariance matrix, and thus the covariance matrix is block diagonal in the decomposition

to the coupled subspace and the DFS. We thus have that $F = F_{\mathrm{C}} + F_{\mathrm{DFS}}$, where F_{C} is the information from the coupled subspace and F_{DFS} is the information from the DFS. The quantity:

$$\eta = \frac{F_{\mathrm{DFS}}}{F_{\mathrm{DFS}} + F_{\mathrm{C}}} \tag{A.39}$$

is the fraction of the information that comes from the DFS and thus quantifies the effectiveness of the DFI.

A.4 Optimal Measurement Basis

We prove here that the optimal quadrature to be measured is $\Sigma_q^{-1}\boldsymbol{\mathcal{V}}_+$, i.e., the operator $\left(\Sigma_q^{-1}\boldsymbol{\mathcal{V}}_+\right)\cdot\hat{\mathbf{Q}}_{\mathrm{out}}$. We then extend this to the multi-parameter case, proving that measuring the two quadratures $\Sigma_q^{-1}\boldsymbol{\mathcal{V}}$ saturates the QFIM.

Consider the single parameter estimation of h_+. the mean vector is $\mathbf{d}_q = \boldsymbol{\mathcal{V}}h$ and the covariance matrix is Σ_q (we use here the complex compact form). Measuring the quadrature $\mathbf{u}$ of this Gaussian state yields the following FI about h_+ (special case of eq. (A.36)):

$$F = 2\frac{|\mathbf{u}\cdot\boldsymbol{\mathcal{V}}_+|^2}{\mathbf{u}^\dagger\Sigma_q\mathbf{u}}. \tag{A.40}$$

From the Cauchy-Schwarz inequality,

$$|(\sqrt{\Sigma_q}\mathbf{u})\cdot(\sqrt{\Sigma_q}^{-1}\boldsymbol{\mathcal{V}}_+)|^2 \leq \left(\mathbf{u}^\dagger\Sigma_q\mathbf{u}\right)\left(\boldsymbol{\mathcal{V}}_+{}^\dagger\Sigma_q^{-1}\boldsymbol{\mathcal{V}}_+\right) \tag{A.41}$$

$$\Rightarrow\ 2\frac{|\mathbf{u}\cdot\boldsymbol{\mathcal{V}}_+|^2}{\left(\mathbf{u}^\dagger\Sigma_q\mathbf{u}\right)} \leq 2\left(\boldsymbol{\mathcal{V}}_+{}^\dagger\Sigma_q^{-1}\boldsymbol{\mathcal{V}}_+\right), \tag{A.42}$$

where the right-hand side of the inequality is the expression for QFI and equality is obtained if and only if

$$\sqrt{\Sigma_q}\mathbf{u} \propto \sqrt{\Sigma_q}^{-1}\boldsymbol{\mathcal{V}}_+ \Rightarrow \mathbf{u} \propto \Sigma_q^{-1}\boldsymbol{\mathcal{V}}_+. \tag{A.43}$$

Hence, the QFI is saturated given that the distributed quadrature $\Sigma_q^{-1}\boldsymbol{\mathcal{V}}_+$ is measured. □

In general, the QFI is saturated by measuring a set of quadratures, if and only if $\Sigma_q^{-1}\boldsymbol{\mathcal{V}}_+$ is contained in the subspace spanned by them.

Regarding the multi-parameter estimation of h_+, $h_\times$ (or any other polarizations), we show that the QFIM is saturated by measuring the two quadratures $\Sigma_q^{-1}\boldsymbol{\mathcal{V}}$, and this is therefore the optimal measurement.

Proof: Observe that for any projection operator Π:

$$\begin{aligned} &\mathcal{V}^\dagger \sqrt{\Sigma_q}^{-1} (\mathbb{1} - \Pi) \sqrt{\Sigma_q}^{-1} \mathcal{V} \geq 0 \\ \Rightarrow &\mathcal{V}^\dagger \sqrt{\Sigma_q}^{-1} \Pi \sqrt{\Sigma_q}^{-1} \mathcal{V} \leq \mathcal{V}^\dagger \Sigma_q^{-1} \mathcal{V} \end{aligned} \tag{A.44}$$

with equality if and only if $\Pi \sqrt{\Sigma_q}^{-1} \mathcal{V} = \sqrt{\Sigma_q}^{-1} \mathcal{V}$. Taking the following projection operator: $\Pi = \sqrt{\Sigma_q} T_h \left(T_h^\dagger \Sigma_q T_h \right)^{-1} T_h^\dagger \sqrt{\Sigma_q}$, and inserting it into eq. (A.44) we obtain that:

$$2\mathcal{V}^\dagger T_h \left(T_h^\dagger \Sigma_q T_h \right)^{-1} T_h^\dagger \mathcal{V} \leq 2\mathcal{V}^\dagger \Sigma_q^{-1} \mathcal{V}. \tag{A.45}$$

The left term is exactly the homodyne FI. Note that our Π is a projection operator onto the span of the column vectors of $\sqrt{\Sigma_q} T_h$, denoted as $C\left(\sqrt{\Sigma_q} T_h\right)$. Hence equality is obtained iff $C\left(\sqrt{\Sigma_q}^{-1} \mathcal{V}\right) \subseteq C\left(\sqrt{\Sigma_q} T_h\right)$ and thus the minimal space of quadratures that saturate the inequality is: $T_h = \Sigma_q^{-1} \mathcal{V} \Lambda$, where Λ is a normalization and orthogonalization matrix. □

This was also proven in ref. [64].

Since the multi-parameter case requires commutativity of the quadratures given by the column vectors of $\Sigma_q^{-1} \mathcal{V}$, we prove a useful claim — if the quadratures given by the column vectors of $\mathcal{V}$ commute and Σ_q is a conjugate symplectic matrix then the quadratures given by $\Sigma_q^{-1} \mathcal{V}$ commute and thus the QFIM is achievable.

Proof: Since conjugate symplectic matrices form a group then Σ_q conjugate symplectic $\rightarrow \Sigma_q^{-1}$ conjugate symplectic , i.e., denoting $\mathcal{W} = \begin{pmatrix} 0 & \mathbb{1}_k \\ -\mathbb{1}_k & 0 \end{pmatrix}$:

$$\left(\Sigma_q^{-1} \right)^\dagger \mathcal{W} \Sigma_q^{-1} = \mathcal{W}. \tag{A.46}$$

Hence:

$$\mathcal{V} \text{commute} \leftrightarrow \mathcal{V}^\dagger \mathcal{W} \mathcal{V} = 0 \tag{A.47}$$

$$\Rightarrow \left(\Sigma_q^{-1} \mathcal{V} \right)^\dagger \mathcal{W} \left(\Sigma_q^{-1} \mathcal{V} \right) = \mathcal{V}^\dagger \mathcal{W} \mathcal{V} = 0. \tag{A.48}$$

Therefore $\Sigma_q^{-1} \mathcal{V}$ commute.□

In our problem, the column vectors of $\mathcal{V}$ are in the phase quadratures, hence they commute. Therefore in order to show commutativity of the optimal quadratures it suffices to show that Σ_q is symplectic.

A.5 QFI with Thermal Displacement Noise

Displacement of optical components leads to a noisy displacement of the quadratures, i.e., in Heisenberg picture: $\hat{\mathbf{Q}} \rightarrow \hat{\mathbf{Q}} + A\mathbf{\Delta x}$, where $\mathbf{\Delta x}$ is a multivariate Gaussian random variable.

The new state under the action of this noise is a Gaussian mixture of states

$$\rho = \int p\left(\mathbf{\Delta x}\right) \rho\left(\mathbf{\Delta x}\right) \mathrm{d}\mathbf{\Delta x} \tag{A.49}$$

and therefore is also Gaussian.

Note that while $\mathbf{\Delta x}\left(t\right)$ is a real vector, $\mathbf{\Delta x}\left(\Omega\right)$ is complex. The transformation of the Hermitian quadratures vector $\hat{\mathbf{S}}$ is therefore given by

$$\hat{\mathbf{S}} \rightarrow \hat{\mathbf{S}} + A'\mathbf{\Delta x}', \tag{A.50}$$

where

$$A' = \begin{pmatrix} \mathrm{Re}\left(A\right) & \text{-}\mathrm{Im}\left(A\right) \\ \mathrm{Im}\left(A\right) & \mathrm{Re}\left(A\right) \end{pmatrix}, \Delta x' = \sqrt{2} \begin{pmatrix} \mathrm{Re}\left(\Delta x\right) \\ \mathrm{Im}\left(\Delta x\right) \end{pmatrix}. \tag{A.51}$$

Since $\langle \mathbf{\Delta x} \rangle = 0$, the vector of the first moments $\mathbf{d_s}$ is unchanged. The covariance matrix however changes to:

$$\begin{aligned} \Sigma =& \Sigma_i + \langle (A'\mathbf{\Delta x}')(A'\mathbf{\Delta x}')^\dagger \rangle \\ =& \Sigma_i + A'\Sigma_{\mathbf{\Delta x}'}A'^\dagger, \end{aligned} \tag{A.52}$$

where Σ_i is the covariance matrix of the states in the absence of displacement noise and $\Sigma_{\Delta x'} = \langle \mathbf{\Delta x}'(\mathbf{\Delta x}')^\dagger \rangle$ is the covariance matrix of $\mathbf{\Delta x}'$.

We assume that the displacement noise $\{\mathbf{\Delta x}\left(t\right)\}_t$ is a Gaussian stationary process, where the different $\Delta x_i\left(t\right), \Delta x_j\left(t\right)$ are i.i.d. Therefore $\mathbf{\Delta x}'\left(\Omega\right)$ is also a Gaussian random variable with a covariance matrix of:

$$\begin{aligned} \langle \left(\mathrm{Re}\left(\Delta x\right)\right)^2 \rangle &= 2 \int_0^T \int_0^T \langle \Delta x\left(t_1\right) \Delta x\left(t_2\right) \rangle \cos\left(\Omega t_1\right) \cos\left(\Omega t_2\right) dt_1 dt_2 \\ &\approx T \int_0^T C\left(\tau\right) \cos\left(\Omega\tau\right) d\tau \end{aligned} \tag{A.53}$$

$$\begin{aligned}\left\langle \left(\mathrm{Im}\left(\Delta x\right)\right)^2\right\rangle &= 2\int_0^T\int_0^T \left\langle \Delta x\left(t_1\right)\Delta x\left(t_2\right)\right\rangle \sin\left(\Omega t_1\right)\sin\left(\Omega t_2\right)dt_1dt_2 \\ &\approx T\int_0^T C\left(\tau\right)\cos\left(\Omega\tau\right)d\tau\end{aligned} \tag{A.54}$$

$$\left\langle \mathrm{Re}\left(\Delta x\right)\mathrm{Im}\left(\Delta x\right)\right\rangle = 2\int_0^T\int_0^T \left\langle \Delta x\left(t_1\right)\Delta x\left(t_2\right)\right\rangle \cos\left(\Omega t_1\right)\sin\left(\Omega t_2\right)dt_1dt_2 \approx 0, \tag{A.55}$$

and of course all the correlations of $\Delta x_i', \Delta x_j'(i \neq j)$ vanish. Therefore $\Sigma_{\Delta x'} = \frac{\delta^2}{2}\mathbb{1}$, and thus $\mathbf{\Delta x}' \sim N\left(0, \frac{\delta^2}{2}\mathbb{1}\right)$.

Since $\Sigma_i = \frac{1}{2}M'M'^{\dagger}$, we get that:

$$\Sigma = \frac{1}{2}\left(M'M'^{\dagger} + \delta^2 A'A'^{\dagger}\right). \tag{A.56}$$

The QFIM therefore reads

$$\begin{aligned}I =& 2\partial_{\mathbf{h}}\mathbf{d_s}^{\dagger}\left(M'M'^{\dagger} + \delta^2 A'A'^{\dagger}\right)^{-1}\partial_{\mathbf{h}}\mathbf{d_s} \\ =& 2\mathcal{V}'^{\dagger}\left(M'M'^{\dagger} + \delta^2 A'A'^{\dagger}\right)^{-1}\mathcal{V}'.\end{aligned} \tag{A.57}$$

Alternatively, the form of the covariance matrix can be also directly derived from the Wigner function. Due to the displacement noise, we have:

$$W\left[\rho\right] = \int p\left(\mathbf{\Delta x}\right) W\left[\rho\left(\mathbf{\Delta x}\right)\right] \mathrm{d}\mathbf{\Delta x}. \tag{A.58}$$

For k output quadratures, the Wigner function per realization of $\mathbf{\Delta x}$ is:

$$W(\mathbf{\Delta x}) = \frac{1}{\left(2\pi\right)^{2k}\sqrt{\mathrm{Det}\left(\sigma\right)}}\exp\left[-\frac{1}{2}\left(\mathbf{S} - d_{\mathbf{h}} - d_{\mathbf{\Delta x}}\right)^{\dagger}\Sigma_i^{-1}\left(\mathbf{S} - d_{\mathbf{h}} - d_{\mathbf{\Delta x}}\right)\right]. \tag{A.59}$$

Since $p\left(\mathbf{\Delta x}\right)$ is Gaussian, then the averaging (eq. (A.58)) is basically a convolution of two Gaussian distributions,

$$N(\mathbf{d_s}, \Sigma_i) \circledast N\left(0, \mathrm{Cov}(d_{\mathbf{\Delta x}})\right) = N(\mathbf{d_s}, \Sigma_i) \circledast N\left(0, \delta^2 A'A'^{\dagger}\right) = N(\mathbf{d_s}, \Sigma_i + \delta^2 A'A'^{\dagger}). \tag{A.60}$$

Therefore,

$$W = \frac{1}{(2\pi)^{2n}\sqrt{\mathrm{Det}\,(\Sigma)}} \exp\left[-\frac{1}{2}\left(\mathbf{S} - d_{\mathbf{h}}\right)^{\dagger} \Sigma^{-1} \left(\mathbf{S} - d_{\mathbf{h}}\right)\right], \tag{A.61}$$

with $\Sigma = \Sigma_i + \delta^2 A' A'^{\dagger}$.

We can therefore observe that the full covariance matrix, eq. (A.56), satisfies the symmetry of eq. (A.22). We have shown in Appendix A.2 that if the covariance matrix satisfies the circular symmetry then the QFI can be written in the complex compact form, this justifies our use of this form:

$$I = 4\boldsymbol{\mathcal{V}}_{+}^{\dagger}\left(MM^{\dagger} + \delta^2 AA^{\dagger}\right)\boldsymbol{\mathcal{V}}_{+}. \tag{A.62}$$

On a brief note — a DFS is defined as the kernel of the (general) noise term $A_{\mathrm{ph}}\Sigma_{\Delta x}A_{\mathrm{ph}}^{\dagger}$. Note that $\ker\left(A_{\mathrm{ph}}^{\dagger}\right)$ is contained in this subspace. furthermore if $\Sigma_{\Delta x}$ is a full rank matrix, the DFS is equal to $\ker\left(A_{\mathrm{ph}}^{\dagger}\right)$.

A.6 FI and QFI with Radiation Pressure

Derivation of Transfer Matrix

Let us first write how Radiation Pressure Noise (RPN) enters into the equations [59]. Resonance conditions are assumed. Given $\hat{\mathbf{a}}, \hat{\mathbf{d}}$ fields that hit a mirror — $\hat{\mathbf{a}} = \begin{pmatrix} \hat{a}_1 \\ \hat{a}_2 \end{pmatrix}$, $\hat{\mathbf{d}} = \begin{pmatrix} \hat{d}_1 \\ \hat{d}_2 \end{pmatrix}$ — the reflected fields $\hat{\mathbf{b}}, \hat{\mathbf{c}}$ satisfy:

$$\begin{pmatrix} \hat{\boldsymbol{b}} \\ \hat{\boldsymbol{c}} \end{pmatrix} = M_{\mathrm{mirror}} \begin{pmatrix} \hat{\boldsymbol{a}} \\ \hat{\boldsymbol{d}} \end{pmatrix} - 2\left(\frac{\omega_0}{c}\right)\frac{\sqrt{R}}{\sqrt{\hbar\omega_0}}\Delta\hat{x}\begin{pmatrix} \boldsymbol{D}_{\boldsymbol{a}}^{*} \\ \boldsymbol{D}_{\boldsymbol{d}}^{*} \end{pmatrix}, \tag{A.63}$$

with $M_{\mathrm{mirror}} = \begin{pmatrix} -\sqrt{R} & & \sqrt{T} & \\ & -\sqrt{R} & & \sqrt{T} \\ \sqrt{T} & & \sqrt{R} & \\ & \sqrt{T} & & \sqrt{R} \end{pmatrix}$ being the mirror transformation, $\Delta\hat{x}$ is the displacement due to RPN. Assuming resonance ($\omega_0 L/c = 2\pi n$, where n is an integer): $\boldsymbol{D_j} = \sqrt{2p_j}\begin{pmatrix} 1 \\ 0 \end{pmatrix}$, $\boldsymbol{D_j^*} = \sqrt{2p_j}\begin{pmatrix} 0 \\ -1 \end{pmatrix}$, where p_j is the power of the j-th carrier field. eq. (A.63) is the general way displacement noise is being propagated. In RPN $\Delta\hat{x}$ is an operator, and it is given by :

$$\begin{aligned} \Delta\hat{x} &= \frac{1}{m\Omega^2}\sqrt{\frac{\hbar\omega_0}{c^2}}\left[\begin{pmatrix} \boldsymbol{D_a^t} & -\boldsymbol{D_d^t} \end{pmatrix}\begin{pmatrix} \hat{\boldsymbol{a}} \\ \hat{\boldsymbol{d}} \end{pmatrix} + \begin{pmatrix} \boldsymbol{D_b^t} & -\boldsymbol{D_c^t} \end{pmatrix}\begin{pmatrix} \hat{\boldsymbol{b}} \\ \hat{\boldsymbol{c}} \end{pmatrix}\right] \\ &= \frac{1}{m\Omega^2}\sqrt{\frac{2\hbar\omega_0}{c^2}}\left[\sqrt{p_a}\hat{a}_1 - \sqrt{p_d}\hat{d}_1 + \sqrt{p_b}\hat{b}_1 - \sqrt{p_c}\hat{c}_1\right]. \end{aligned} \tag{A.64}$$

Inserting this $\Delta\hat{x}$ into eq. (A.63) we get two coupled sets of equations. For the amplitude quadratures:

$$\begin{pmatrix} \hat{b}_1 \\ \hat{c}_1 \end{pmatrix} = M_{\text{mirror}} \begin{pmatrix} \hat{a}_1 \\ \hat{d}_1 \end{pmatrix}, \tag{A.65}$$

and for the phase quadrature:

$$\begin{aligned} \begin{pmatrix} \hat{b}_2 \\ \hat{c}_2 \end{pmatrix} =& M_{\text{mirror}} \begin{pmatrix} \hat{a}_2 \\ \hat{d}_2 \end{pmatrix} \\ &- \frac{2\sqrt{2}\omega_0\sqrt{R}}{m\Omega^2 c^2} \left[\sqrt{p_a}\hat{a}_1 - \sqrt{p_d}\hat{d}_1 + \sqrt{p_b}\hat{b}_1 - \sqrt{p_c}\hat{c}_1\right] \begin{pmatrix} \sqrt{2p_a} \\ \sqrt{2p_d} \end{pmatrix}. \end{aligned} \tag{A.66}$$

This implies a general structure for the multichannel case: the equations for the amplitude quadratures are closed and their solution is given by

$$\hat{\mathbf{b}}_\mathbf{1} = M_{\text{int}}\hat{\mathbf{a}}_\mathbf{1}, \tag{A.67}$$

where M_{int} is the unitary transfer matrix of the interferometer which does not depend on the RPN. The equations for the amplitude quadratures are coupled to the phase quadratures and their solution is given by:

$$\hat{\mathbf{b}}_\mathbf{2} = M_{\text{int}}\hat{\mathbf{a}}_\mathbf{2} + M_{21}\hat{\mathbf{a}}_\mathbf{1}. \tag{A.68}$$

Hence amplitude noise is being propagated into phase noise with a transfer matrix M_{21}. The input-output relations therefore read:

$$\begin{pmatrix} \hat{\mathbf{b}}_\mathbf{1} \\ \hat{\mathbf{b}}_\mathbf{2} \end{pmatrix} = \begin{pmatrix} M_{\text{int}} & 0 \\ M_{21} & M_{\text{int}} \end{pmatrix} \begin{pmatrix} \hat{\mathbf{a}}_\mathbf{1} \\ \hat{\mathbf{a}}_\mathbf{2} \end{pmatrix}. \tag{A.69}$$

Two observations regarding the transfer matrix of eq. (A.69) will be useful later:

1. M_{21} can be expressed as a concatenation of two transfer matrices: $M_{21} = AD_x$, where A is the transfer matrix of mirror displacement vector $\boldsymbol{\Delta}\hat{\mathbf{x}}$, and D_x is the transfer matrix of the amplitude noise to the displacement vector: $\boldsymbol{\Delta}\hat{\mathbf{x}} = D_x\hat{\mathbf{a}}_\mathbf{1}$. This fact will be used to in Appendix A.7.

2. Commutation relations have to be preserved (see eq. (A.8)). This implies that M is a conjugate symplectic matrix and thus $M_{\text{int}}^\dagger M_{21}$ is Hermitian.

3. From eq. (A.66) we observe that $M_{21} \propto 1/m\Omega^2$.

Quantum Fisher Information (QFI)

Given the general form of the transfer matrix M (eq. (A.69)), we can calculate the general form of the QFI and FI. The QFI is given by $4\boldsymbol{\mathcal{V}}_+^\dagger \left(MM^\dagger\right)^{-1} \boldsymbol{\mathcal{V}}_+$ where $MM^\dagger$ $(= 2\Sigma_q)$ equals to:

$$MM^\dagger = \begin{pmatrix} \mathbb{1} & M_{\text{int}} M_{21}^\dagger \\ M_{21} M_{\text{int}}^\dagger & \mathbb{1} + M_{21} M_{21}^\dagger \end{pmatrix}. \tag{A.70}$$

Since M_{int} is unitary we can observe that:

$$\begin{aligned} \left(MM^\dagger\right)^{-1} &= \begin{pmatrix} * & -M_{\text{int}} M_{21}^\dagger \\ * & \mathbb{1} \end{pmatrix} \\ \overset{\#}{\Longrightarrow} I = 4\boldsymbol{\mathcal{V}}_+^\dagger \boldsymbol{\mathcal{V}}_+ &= 4\boldsymbol{\mathcal{V}}_{+,\text{ph}}^\dagger \boldsymbol{\mathcal{V}}_{+,\text{ph}}, \end{aligned} \tag{A.71}$$

where (#) is because: $\mathcal{V} = \begin{pmatrix} 0 \\ \mathcal{V}_{\text{ph}} \end{pmatrix}$. The QFI thus obtainsnthe shot-noise limit. This is a generalization of the single channel optimal frequency-dependent readout scheme [31]: by measuring certain quadratures we can overcome the RPN. Using the results of Appendix A.4, we know that the optimal quadratures to be measured are (up to normalization): $\Sigma_q^{-1} \boldsymbol{\mathcal{V}}_+$. The optimal quadrature is therefore:

$$\mathbf{u} \propto \begin{pmatrix} -M_{\text{int}} M_{21}^\dagger \boldsymbol{\mathcal{V}}_{+,\text{ph}} \\ \boldsymbol{\mathcal{V}}_{+,\text{ph}} \end{pmatrix}, \tag{A.72}$$

i.e., measuring the operator $\mathbf{u} \cdot \hat{\mathbf{Q}}_{\text{out}}$ is optimal. This $\mathbf{u}$ is a linear combination of the k column vectors of the matrix T_{dec}:

$$T_{\text{dec}} = \begin{pmatrix} -M_{\text{int}} M_{21}^\dagger \\ \mathbb{1} \end{pmatrix}. \tag{A.73}$$

These k column vectors correspond to k quadratures decoupled from RPN. To see explicitly that these quadratures are decoupled from RPN, note that the covariance matrix can be written as:

$$\Sigma_q \propto \begin{pmatrix} \mathbb{1} & M_{\text{int}} M_{21}^\dagger \\ M_{21} M_{\text{int}}^\dagger & \mathbb{1} + M_{21} M_{21}^\dagger \end{pmatrix} = \begin{pmatrix} 0 & 0 \\ 0 & \mathbb{1} \end{pmatrix} + \begin{pmatrix} \mathbb{1} \\ M_{21} M_{\text{int}}^\dagger \end{pmatrix} \begin{pmatrix} \mathbb{1} & M_{\text{int}} M_{21}^\dagger \end{pmatrix}, \tag{A.74}$$

the space spanned by these quadratures is thus decoupled from RPN. Hence any combination of these quadratures is decoupled from this noise and thus yields an

FI that does not diverge in the $f \to 0$ limit, the optimal combination of eq. (A.72) obtains the shot noise limit.

Two remarks are now in order:

- We remark that the quadratures of eq. (A.73) are not orthonormal, the orthonormalized quadratures are the k column vectors of the following matrix:

$$\begin{pmatrix} -M_{\rm int}M_{21}^{\dagger} \\ \mathbb{1} \end{pmatrix} \left(\mathbb{1} + M_{21}M_{21}^{\dagger}\right)^{-1/2}. \tag{A.75}$$

- We note that these quadratures can be measured simultaneously only if they commute. Let show that they indeed commute:

$$\begin{pmatrix} -M_{21}M_{\rm int}^{\dagger} & \mathbb{1} \end{pmatrix} \begin{pmatrix} 0 & \mathbb{1} \\ -\mathbb{1} & 0 \end{pmatrix} \begin{pmatrix} -M_{\rm int}M_{21}^{\dagger} \\ \mathbb{1} \end{pmatrix} = -M_{\rm int}M_{21}^{\dagger} + M_{21}M_{\rm int}^{\dagger} = 0, \tag{A.76}$$

  where in the last equality we used the fact that $M_{21}M_{\rm int}^{\dagger}$ is Hermitian.

We can thus either measure the quadratures of eq. (A.73) or the optimal quadrature in eq. (A.72). The advantage in measuring the quadratures of eq. (A.72) is that they are independent of $\boldsymbol{\mathcal{V}}_+$. They are optimal for the estimation of any polarization, and thus optimal also for simultaneous estimation of $\boldsymbol{\mathcal{V}}_+, \mathcal{V}_\times$ or any two other polarizations.

Fisher Information (FI)

Let us now consider the case of measuring the phase quadratures. The correspondong covariance matrix is obtained by applying eq. (A.36), i.e., keeping only the phase quadrature terms in the full covariance matrix (eq. (A.70)), which leaves us with $\sigma_h = 1/2\left(\mathbb{1} + M_{21}M_{21}^{\dagger}\right)$, and thus the FI is $F = 4\boldsymbol{\mathcal{V}}_{+,\rm ph}^{\dagger}\left(\mathbb{1} + M_{21}M_{21}^{\dagger}\right)^{-1}\boldsymbol{\mathcal{V}}_{+,\rm ph}$. $M_{21}M_{21}^{\dagger}$ is basically the displacement noise term.

Since $M_{21} = A_{\rm ph}D_x$, we get:

$$M_{21}M_{21}^{\dagger} = A_{\rm ph}D_xD_x^{\dagger}A_{\rm ph}^{\dagger}, \tag{A.77}$$

hence it takes the form of displacement noise (eq. (A.52)) with $D_xD_x^{\dagger}$ being the covariance matrix of the displacement vector $\mathbf{\Delta x}$. We can immediately observe that

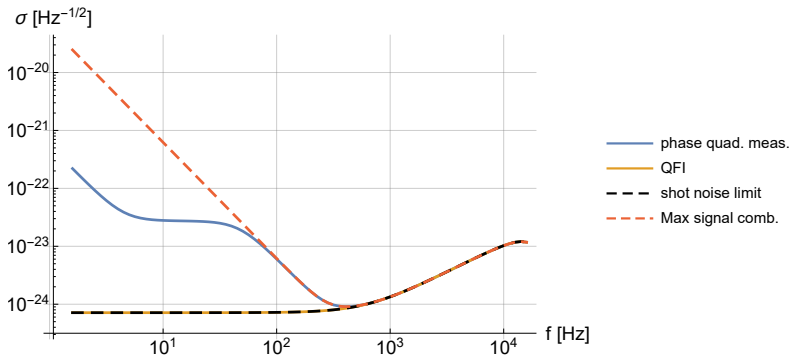

(a)

Figure A.1: Sensitivity profile with RPN for different measurement bases. The QFI corresponds to optimal measurement (solid orange line) and saturates the shot noise limit (black dashed line). The solid blue line corresponds to phase quadratures measurement (and thus optimal combination of phase quadratures) and the dashed red line to the max-signal combination of phase quadratures, i.e., a combination that is optimal given only shot noise.

the space decoupled from this noise is $\ker\left(D_x^\dagger A_{\rm ph}^\dagger\right)$. The DFS, $\ker A_{\rm ph}^\dagger$, is thus contained in this subspace and therefore decoupled from this noise.

In fig. A.1 we show the sensitivity profile given RPN for different homodyne measurements: optimal (eq. (A.72)), phase quadratures and maximal signal combination (basically $\mathcal{V}$, which maximizes the signal and thus optimal in case there is only shot noise). For the optimal frequency-dependent combination (eq. (A.72)), the SD coincides with the shot noise limit as expected.

It is interesting to compare the behavior of the FI with phase quadratures measurement and the behavior with the max-signal combination in fig. A.1. Both diverge at low frequencies and clearly since the max-signal combination is not optimal its sensitivity is worse than the sensitivity of the phase quadratures measurement. While the max-signal combination diverges uniformly as $1/f^2$, the optimal phase quadratures combination has an intermediate range where the divergence stops and the sensitivity remains constant. This creates two orders of magnitude difference between the sensitivity with max-signal combination and with the optimal phase quadratures combination.

This plateau is due to a pseudo-DFS contained in the coupled subspace, $M_{\rm C}$. For any frequency, $M_{21}M_{21}^\dagger$ has 3 eigenvalues: $0, t_{\rm min}, t_{\rm max}$, where $t_{\rm min} \ll t_{\rm max}$. The phase quadratures can be thus decomposed to the corresponding eigenspaces. The

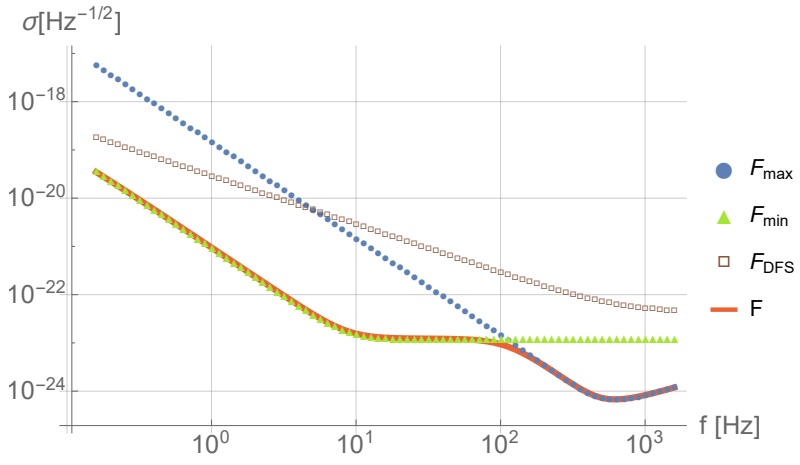

(a)

Figure A.2: Sensitivity profile that corresponds to phase quadratures measurement (F) along with $F_{\max}$ (blue dots), $F_{\min}$ (green triangles), and F_{DFS} (brown squares), as defined in the text. As shown in the text $F = F_{\max} + F_{\min} + F_{\mathrm{DFS}}$.

eigenspace of 0 is the DFS, M_{DFS}, and the eigenspaces of $t_{\min}, t_{\max}$ are denoted as $M_{\min}, M_{\max}$, respectively. Note that $M_{\mathrm{C}} = M_{\min} \oplus M_{\max}$. Since the covariance matrix is diagonal w.r.t these subspaces the FI is a sum of the FI's of these subspaces:

$$F = F_{\mathrm{DFS}} + F_{\mathrm{C}} = F_{\mathrm{DFS}} + F_{\max} + F_{\min}, \tag{A.78}$$

where $F_{\max}, F_{\min}$ are the FI's achieved with $M_{\max}, M_{\min}$, respectively. $\boldsymbol{\mathcal{V}}_+$ is mostly in the subspace $M_{\max}$, hence for frequencies higher than the plateau range $F \approx F_{\max}$. The SD that corresponds to $F_{\max}$ goes as $1/f^2$ and coincides with the max-signal combination (see fig. A.2). As f gets smaller, $F_{\max}$ drops as f^4 while $F_{\min}$ remains the same (since $t_{min} \ll 1$). In this regime $M_{\min}$ functions as a pseudo-DFS since the effect of displacement noise is much smaller than the shot noise. Therefore at some point $F_{\min} > F_{\max}$, and the FI coincides with the $F_{\min}$ which remains the same. This is the plateau that can be observed in figs. A.1 and A.2. $t_{\min}$ however also goes as $1/f^4$ and thus for low enough frequencies $t_{\min} \gg 1$ and the SD continues to diverge as $1/f^2$. This is shown in fig fig. A.2 where the FI is shown along with the contribution of $F_{\max}, F_{\min}, F_{\mathrm{DFS}}$. We can see the crossing between $F_{\max}$ and $F_{\min}$ that takes place at the beginning of the plateau.

A.7 FI and QFI with Radiation Pressure and Thermal Displacement Noise

In realistic scenarios we have both RPN and thermal displacement noise, i.e., a covariance matrix of $\Sigma_q = 1/2\left(MM^\dagger + \delta^2 AA^\dagger\right)$. The QFI in this case is the same

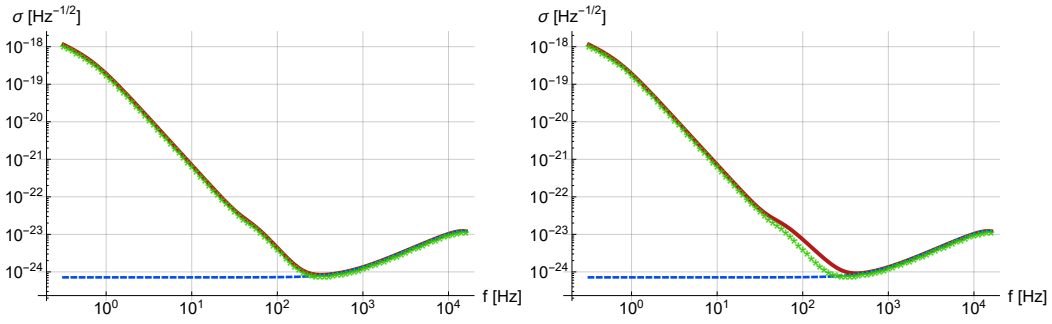

(a) (b)

Figure A.3: Sensitivity profile given thermal noise, with and without radiation pressure. (a) QFI: QFI with both thermal noise and RPN (red, solid line) coincides with QFI given only thermal noise (green diamonds). Blue dashed line corresponds to the shot noise limit. (b) FI with phase quadrature measurement: red solid line corresponds to both thermal and RPN, green diamonds to only thermal noise and blue, dashed line to shot noise limit.

as with only thermal displacement noise since the RPN can be removed using the same optimal frequency-dependent readout (eqs. (A.72) and (A.73)). Let us show this formally:

$$\Sigma_q = 1/2 \begin{pmatrix} \mathbb{1} & M_{\rm int} M_{21}^\dagger \\ M_{21} M_{\rm int}^\dagger & \mathbb{1} + M_{21} M_{21}^\dagger + \delta^2 A_{\rm ph} A_{\rm ph}^\dagger \end{pmatrix}. \tag{A.79}$$

With a similar calculation as before:

$$\Sigma_q^{-1} = 2 \begin{pmatrix} * & -M_{\rm int} M_{21}^\dagger \left(\mathbb{1} + \delta^2 A_{\rm ph} A_{\rm ph}^\dagger\right)^{-1} \\ * & \left(\mathbb{1} + \delta^2 A_{\rm ph} A_{\rm ph}^\dagger\right)^{-1} \end{pmatrix} \tag{A.80}$$

$$\Rightarrow I = 4 \boldsymbol{\mathcal{V}}_{+,\rm ph}^\dagger \left(\mathbb{1} + \delta^2 A_{\rm ph} A_{\rm ph}^\dagger\right)^{-1} \boldsymbol{\mathcal{V}}_{+,\rm ph}. \tag{A.81}$$

Hence RPN is removed with this optimal readout, this is shown in fig. A.3 (a). The optimal quadrature is

$$u \propto \begin{pmatrix} -M_{\rm int} M_{21}^\dagger \tilde{\mathcal{V}} \\ \tilde{\mathcal{V}} \end{pmatrix}, \tag{A.82}$$

where $\tilde{\mathcal{V}} = \left(\mathbb{1} + \delta^2 A_{\rm ph} A_{\rm ph}^\dagger\right)^{-1} \boldsymbol{\mathcal{V}}_{+,\rm ph}$. As in Appendix A.6, we can achieve this QFI also by measuring the quadratures decoupled from RPN of eq. (A.73). The only difference is that now the optimal linear combination of these quadratures is $\tilde{\mathcal{V}}$ instead of $\boldsymbol{\mathcal{V}}_+$.

Measuring the phase quadratures the FI reads:

$$\begin{aligned} F &= 4\boldsymbol{\mathcal{V}}_{+,\mathrm{ph}}^{\dagger}\left(\mathbb{1}+M_{21}M_{21}^{\dagger}+\delta^{2}A_{\mathrm{ph}}A_{\mathrm{ph}}^{\dagger}\right)^{-1}\boldsymbol{\mathcal{V}}_{+,\mathrm{ph}} \\ &\overset{*}{=} 4\boldsymbol{\mathcal{V}}_{+,\mathrm{ph}}^{\dagger}\left(\mathbb{1}+A_{\mathrm{ph}}\left[D_{x}D_{x}^{\dagger}+\delta^{2}\mathbb{1}\right]A_{\mathrm{ph}}^{\dagger}\right)^{-1}\boldsymbol{\mathcal{V}}_{+,\mathrm{ph}}. \end{aligned} \tag{A.83}$$

There are two displacement noise terms: $M_{21}M_{21}^{\dagger}$ due to RPN and $\delta^{2}A_{\mathrm{ph}}A_{\mathrm{ph}}^{\dagger}$ due to thermal displacement noise. In $(*)$ we use the fact that $M_{21}=A_{\mathrm{ph}}D_{x}$, therefore the two noise terms can be written as a single displacement noise $\mathbf{\Delta x}$, with a covariance matrix of $1/2\left(\delta^{2}\mathbb{1}+D_{x}D_{x}^{\dagger}\right)$. Since this covariance matrix is full rank the DFS is $\ker\left(A_{\mathrm{ph}}^{\dagger}\right)$ (in our triangular cavity example it is 3 dimensional).

The behavior of the FI for phase quadratures measurement is shown in the red line of fig. A.3 (b): there is an intermediate regime where the RPN is dominant and the FI does not coincide with the FI of only thermal noise. For low enough frequencies however the thermal noise becomes dominant and the FI coincides with the FI of only thermal noise.

A more detailed analysis of the behavior of the FI is presented in fig. A.4. Similar to the behavior observed in Appendix A.6, the divergence is not uniform, but splits into three different regimes. Like in Appendix A.6, we can decompose the phase quadratures to: $M = M_{\max}\oplus M_{\min}\oplus M_{\mathrm{DFS}}$, and define the corresponding FI's: $F_{\max}, F_{\min}, F_{\mathrm{DFS}}$. Since these subspaces are eigenspaces of the covariance matrix we have: $F = F_{\max}+F_{\min}+F_{\mathrm{DFS}}$. In fig. A.4 we examine the contribution of these FI's. We can observe three regimes: for relatively high frequencies $F_{\max}$ is dominant and coincides with F. $M_{\max}$ is a single dimensional subspace that has maximal noise (largest eigenvalue of the covariance matrix), but also yields maximal signal. Therefore in the limit of small noise F coincides with it. Around $f\approx 10^{2}$ Hz, $F_{\min}$ becomes larger than $F_{\max}$, this transition can be observed in fig. A.4. After this crossing $F_{\min}$ becomes the dominant contribution. Like in fig. A.2, there is a small range of frequencies with plateau, where $v_{\min}\approx 1$. For lower frequencies ($f\approx 1$) the noise becomes larger and the dominant contribution is from the DFS: $F\approx F_{\mathrm{DFS}}$.

A.8 Effect of Squeezing

So far the initial state was taken to be a coherent state, i.e., $\Sigma_i=\frac{1}{2}\mathbb{1}$. By squeezing some of the quadratures the sensitivity can be improved. The covariance matrix with squeezing is $\Sigma_i=\frac{1}{2}e^{2r}\Pi_1+\frac{1}{2}e^{-2r}\left(\mathbb{1}-\Pi_1\right)$, i.e., k commuting quadratures

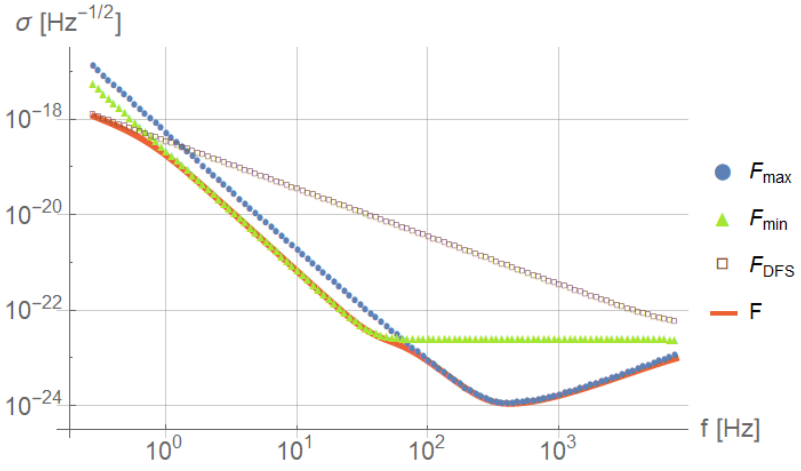

(a)

Figure A.4: Similar to fig. A.2 given thermal displacement noise and RPN with phase quadratures measurement. Three different regimes of the FI: the solid red line correspond to F, the blue dots to $F_{\max}$, green triangles to $F_{\min}$ and brown squares to F_{DFS}. The different FI's coincide with total FI in three different regimes.

are squeezed, where Π_1 is their projection operator. As a result the conjugate k quadratures are antisqueezed. A trivial upper bound of the QFI corresponds to squeezing all the quantum noise by e^{-2r}, i.e.:

$$I \leq 2\boldsymbol{\mathcal{V}}_+^\dagger \left(\Sigma_{\min}\right)^{-1} \boldsymbol{\mathcal{V}}_+, \tag{A.84}$$

where $2\Sigma_{\min} = e^{-2r} MM^\dagger + \delta^2 AA^\dagger$, i.e., the quantum part , $MM^\dagger$, is squeezed by e^{-2r}. This bound of the QFI implies a bound on the FI with any homodyne measurement. The bound for the FI given phase quadratures measurement is:

$$\begin{aligned} F &\leq 2\boldsymbol{\mathcal{V}}_+^\dagger T_{\mathrm{ph}} \left(T_{\mathrm{ph}}^\dagger \Sigma_{\min} T_{\mathrm{ph}}\right)^{-1} T_{\mathrm{ph}}^\dagger \boldsymbol{\mathcal{V}}_+ \\ &= 4\boldsymbol{\mathcal{V}}_{+,\mathrm{ph}}^\dagger \left(e^{-2r}\left(\mathbb{1} + M_{21}M_{21}^\dagger\right) + \delta^2 A_{\mathrm{ph}} A_{\mathrm{ph}}^\dagger\right)^{-1} \boldsymbol{\mathcal{V}}_{+,\mathrm{ph}}, \end{aligned} \tag{A.85}$$

i.e., squeezing the quantum part, $\mathbb{1} + M_{21}M_{21}^\dagger$, by e^{-2r}. We show a brief proof of these bounds. For brevity we omit the $\delta^2 AA^\dagger$ term which does not change the proof:

$$2\Sigma_q = M\left[e^{2r}\Pi_1 + e^{-2r}\left(\mathbb{1} - \Pi_1\right)\right] M^\dagger \geq e^{-2r} MM^\dagger = 2\Sigma_{\min} \tag{A.86}$$

$$\overset{*}{\Rightarrow} \Sigma^{-1} \leq \Sigma_{\min}^{-1} \tag{A.87}$$

$$\overset{**}{\Rightarrow} \boldsymbol{\mathcal{V}}_+^\dagger \left(\Sigma\right)^{-1} \boldsymbol{\mathcal{V}}_+ \leq \boldsymbol{\mathcal{V}}_+^\dagger \left(\Sigma_{\min}\right)^{-1} \boldsymbol{\mathcal{V}}_+. \tag{A.88}$$

$(*)$ is due to the fact that for any positive semi-definite matrices B_1, B_2: $B_1 \geq B_2 \Rightarrow B_1^{-1} \leq B_2^{-1}$. $(**)$ is immediate from definition. Similarly:

$$\boldsymbol{\mathcal{V}}_+^\dagger T_{\text{ph}} \left(T_{\text{ph}}^\dagger \Sigma T_{\text{ph}}\right)^{-1} T_{\text{ph}}^\dagger \boldsymbol{\mathcal{V}}_+ \leq \boldsymbol{\mathcal{V}}_+^\dagger T_{\text{ph}} \left(T_{\text{ph}}^\dagger \Sigma_{\text{min}} T_{\text{ph}}\right)^{-1} T_{\text{ph}}^\dagger \boldsymbol{\mathcal{V}}_+. \tag{A.89}$$

Let us now show that both of these bounds are achievable. We first show that by an optimal choice of squeezed quadratures, Π_1, the phase quadratures bound of eq. (A.85) is achievable.

Optimal Squeezing for Phase Quadrature Measurements

To saturate eq. (A.85) we need to find a set of commuting quadratures such that squeezing them yields this bound. Let us first find suitable quadratures and then verify that they commute. We therefore need to find a projection operator Π_1 such that

$$M \left(e^{2r}\Pi_1 + e^{-2r}\left(\mathbb{1} - \Pi_1\right)\right) M^\dagger = \begin{pmatrix} * & * \\ * & e^{-2r}\left(\mathbb{1} + M_{21}M_{21}^\dagger\right) \end{pmatrix}. \tag{A.90}$$

This implies that Π_1 needs to satisfy:

$$M\Pi_1 M^\dagger = \begin{pmatrix} * & * \\ * & 0 \end{pmatrix}, \tag{A.91}$$

i.e., no antisqueezing in the phase quadratures. Following the derivation for single input single output [31], we use an ansatz:

$$\Pi_1 = \begin{pmatrix} \cos(\mathcal{A})^2 & \cos(\mathcal{A})\sin(\mathcal{A}) \\ \cos(\mathcal{A})\sin(\mathcal{A}) & \sin(\mathcal{A})^2 \end{pmatrix}, \tag{A.92}$$

where $\mathcal{A}$ is a Hermitian matrix that we seek to find. It can be checked that this defines a projection operator ($\Pi_1^2 = \Pi_1$) onto the space spanned by $\begin{pmatrix} \cos(\mathcal{A}) \\ \sin(\mathcal{A}) \end{pmatrix}$. We now observe:

$$\begin{aligned} & M \begin{pmatrix} \cos(\mathcal{A})^2 & \cos(\mathcal{A})\sin(\mathcal{A}) \\ \cos(\mathcal{A})\sin(\mathcal{A}) & \sin(\mathcal{A})^2 \end{pmatrix} M^\dagger \\ &= \begin{pmatrix} * & * \\ * & \left(M_{21}\cos(\mathcal{A}) + M_{\text{int}}\sin(\mathcal{A})\right)\left(\cos(\mathcal{A})\, M_{21}^\dagger + \sin(\mathcal{A})\, M_{\text{int}}^\dagger\right) \end{pmatrix} \\ &\Longrightarrow M_{21}\cos(\mathcal{A}) + M_{\text{int}}\sin(\mathcal{A}) = 0 \\ &\Longrightarrow \mathcal{A} = \arctan\left(-M_{\text{int}}^\dagger M_{21}\right). \end{aligned} \tag{A.93}$$

Note that $-M_{\text{int}}^{\dagger}M_{21}$ is Hermitian hence $\mathcal{A}$ is well defined. It is therefore optimal to squeeze the quadratures projected by $\mathbb{1} - \Pi_1$:

$$\begin{aligned}\begin{pmatrix} -\sin(\mathcal{A}) \\ \cos(\mathcal{A}) \end{pmatrix} &= \begin{pmatrix} -\sin\left(-\arctan\left(M_{\text{int}}^{\dagger}M_{21}\right)\right) \\ \cos\left(-\arctan\left(M_{\text{int}}^{\dagger}M_{21}\right)\right) \end{pmatrix} \\ &= \begin{pmatrix} M_{\text{int}}^{\dagger}M_{21} \\ \mathbb{1} \end{pmatrix}\left(\mathbb{1} + \left(M_{\text{int}}^{\dagger}M_{21}\right)^2\right)^{-1/2}.\end{aligned} \tag{A.94}$$

It is straightforward to see that these quadratures commute: for any $\mathcal{A}$

$$\begin{pmatrix} -\sin(\mathcal{A}) & \cos(\mathcal{A}) \end{pmatrix}\begin{pmatrix} 0 & \mathbb{1}_k \\ -\mathbb{1}_k & 0 \end{pmatrix}\begin{pmatrix} -\sin(\mathcal{A}) \\ \cos(\mathcal{A}) \end{pmatrix} = 0. \tag{A.95}$$

Numerical results of the SD without squeezing and with optimal squeezing are presented in fig. A.5.

QFI with Squeezing

It is simple to show that the QFI satisfies the bound of eq. (A.84). The calculation is identical to the calculations in Appendices A.5 and A.6. Given squeezing of phase quadratures:

$$\begin{aligned}\Sigma =& 1/2\begin{pmatrix} M_{\text{int}} & 0 \\ M_{21} & M_{\text{int}} \end{pmatrix}\begin{pmatrix} e^{2r}\mathbb{1} & 0 \\ 0 & e^{-2r}\mathbb{1} \end{pmatrix}\begin{pmatrix} M_{\text{int}}^{\dagger} & M_{21}^{\dagger} \\ 0 & M_{\text{int}}^{\dagger} \end{pmatrix} + \frac{\delta^2}{2}AA^{\dagger} \\ =& 1/2\begin{pmatrix} e^{2r}\mathbb{1} & M_{\text{int}}M_{21}^{\dagger}e^{2r} \\ M_{21}M_{\text{int}}^{\dagger}e^{2r} & e^{-2r}\mathbb{1} + M_{21}M_{21}^{\dagger}e^{2r} + \delta^2 A_{\text{ph}}A_{\text{ph}}^{\dagger} \end{pmatrix} \\ \Rightarrow \Sigma^{-1} =& 2\begin{pmatrix} * & -M_{\text{int}}M_{21}^{\dagger}\left(e^{-2r}\mathbb{1} + \delta^2 A_{\text{ph}}A_{\text{ph}}^{\dagger}\right)^{-1} \\ * & \left(e^{-2r}\mathbb{1} + \delta^2 A_{\text{ph}}A_{\text{ph}}^{\dagger}\right)^{-1} \end{pmatrix} \\ \Rightarrow I =& 4\boldsymbol{\mathcal{V}}_{+,\text{ph}}^{\dagger}\left(e^{-2r}\mathbb{1} + \delta^2 A_{\text{ph}}A_{\text{ph}}^{\dagger}\right)^{-1}\boldsymbol{\mathcal{V}}_{+,\text{ph}}.\end{aligned} \tag{A.96}$$

The quadrature that saturates this bound is:

$$\begin{pmatrix} -M_{\text{int}}M_{21}^{\dagger} \\ \mathbb{1} \end{pmatrix}\left(e^{-2r}\mathbb{1} + \delta^2 A_{\text{ph}}A_{\text{ph}}^{\dagger}\right)^{-1}\boldsymbol{\mathcal{V}}_{+,\text{ph}}. \tag{A.97}$$

The QFI sensitivity with and without squeezing is presented in fig. A.5. It is interesting to compare this QFI to the phase quadratures FI. Without squeezing the QFI is significantly better than the FI in the regime of dominant RPN (in this

illustration 50 Hz-500 Hz). Optimal squeezing removes this difference almost completely since it squeezes the RPN while keeping the thermal displacement noise intact. We can also observe that in both cases the gain from squeezing is not uniform: in some frequency regimes this gain is much larger than in other regimes. This is explained in the next subsection.

η and Squeezing

As mentioned in the main text, for a given choice of homodyne measurement we can define the gain factor

$$\eta_{\text{gain}} = \frac{\frac{F_{\text{sq}}}{F} - 1}{e^{2r} - 1}, \tag{A.98}$$

where $F_{\text{sq}}(F)$ is the FI with(out) squeezing.

For phase quadratures measurement we defined η in the main text as:

$$\eta = \frac{F_{\text{DFS}}}{F}, \tag{A.99}$$

where F_{DFS} is the FI coming from the DFS. This is well defined for phase quadratures measurement, since in this case the quadratures space contains a DFS, $h_{\text{DFS}} \subseteq h$, and the DFS is an eigenspace of the relevant covariance matrix σ_h. Furthermore for phase quadratures measurement we can decompose: $h = h_{\text{DFS}} \oplus h_{\text{C}}$, where h_{C} is the coupled subspace, and thus $F = F_{\text{DFS}} + F_{\text{C}}$, where:

$$F_{\text{DFS}} = 4\mathcal{V}_{\text{DFS}}^{\dagger}\mathcal{V}_{\text{DFS}}, \tag{A.100}$$

$$F_{\text{C}} = 4\mathcal{V}_{\text{C}}^{\dagger}\left(\mathbb{1} + M_{21}M_{21}^{\dagger} + \delta^2 A_{\text{ph}}A_{\text{ph}}^{\dagger}\right)^{-1}\mathcal{V}_{\text{C}} \tag{A.101}$$

where $\mathcal{V}_{\text{DFS}} = \Pi_{\text{DFS}}\mathcal{V}_{\text{ph}}$, $\mathcal{V}_{\text{C}} = \Pi_{\text{C}}\mathcal{V}_{\text{ph}}$.

Optimal squeezing changes the covariance matrix to

$$\frac{e^{-2r}}{2}\left(\mathbb{1} + \mathbb{M}_{2\mathbb{1}}\mathbb{M}_{2\mathbb{1}}^{\dagger}\right) + \frac{\delta^2}{2}A_{\text{ph}}A_{\text{ph}}^{\dagger}, \tag{A.102}$$

and thus after squeezing:

$$F_{\text{DFS}} = 4e^{2r}\mathcal{V}_{\text{DFS}}^{\dagger}\mathcal{V}_{\text{DFS}} \tag{A.103}$$

$$F_{\text{C}} = 4\mathcal{V}_{\text{C}}^{\dagger}\left(e^{-2r}\left(\mathbb{1} + M_{21}M_{21}^{\dagger}\right) + \delta^2 A_{\text{ph}}A_{\text{ph}}^{\dagger}\right)^{-1}\mathcal{V}_{\text{C}}. \tag{A.104}$$

Assuming large displacement noise, i.e., large enough δ, we can approximate:

$$F_{\text{C}} \approx 4\mathcal{V}_{\text{C}}^{\dagger}\left(\delta^2 A_{\text{ph}}A_{\text{ph}}^{\dagger}\right)^{-1}\mathcal{V}_{\text{C}}, \tag{A.105}$$

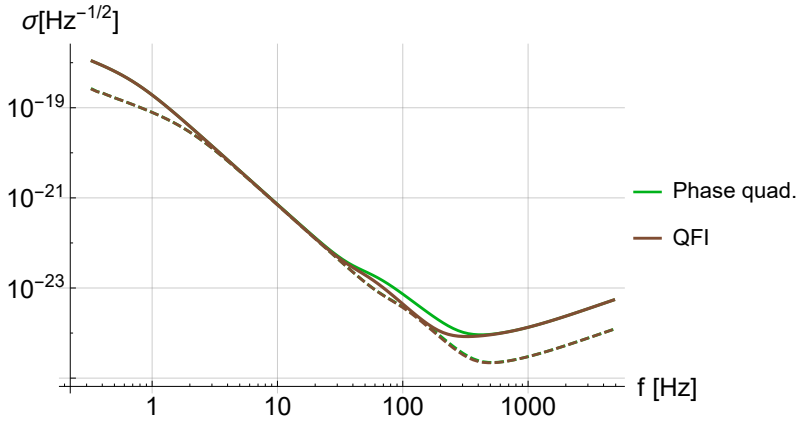

Figure A.5: SD with optimal measurement (brown) and phase quadratures measurement (green). The solid lines correspond to the unsqueezed case and the dashed to optimal squeezing. In this illustration $r = 1.5$.

where $\left(\delta^2 AA^\dagger\right)^{-1}$ refers to the pseudo-inverse of $\delta^2 AA^\dagger$ and we can use it since $\mathcal{V}_C \perp \ker\left(A_{ph}A_{ph}^\dagger\right)$ (by definition of the coupled subspace). Hence F_{DFS} is increased by the squeezing factor e^{2r}, while in the limit of large displacement noise F_C remains unchanged. Clearly only the DFS gains from squeezing and thus the gain from squeezing should go as the effectiveness of the DFI. We can show this formally with η_{gain}:

$$\frac{F_{sq}}{F} = \frac{e^{2r}F_{DFS} + F_C}{F_{DFS} + F_C} \tag{A.106}$$

$$\eta_{gain} = \frac{\frac{F_{sq}}{F} - 1}{e^{2r} - 1} = \frac{\left(e^{2r} - 1\right)F_{DFS}}{\left(e^{2r} - 1\right)\left(F_{DFS} + F_C\right)} = \frac{F_{DFS}}{F} = \eta. \tag{A.107}$$

Therefore in the limit of large displacement noise $\eta_{gain} = \eta$, this is illustrated in (3) in the main text.

A.9 Extensions

The triangular scheme can be extended to any $n-$gon with n mirrors, as illustrated in fig. A.6. The n mirrors are illustrated as n vertices of an $n-$gon embedded on a circle. For each polygon the different light trajectories correspond to different billiard trajectories hitting the vertices, hence there are $n-1$ possible trajectories that correspond to $n-1$ reflection angles $\left\{\frac{2\pi}{n}l\right\}_{l=1}^{n-1}$. The two schemes illustrated in fig. A.6 correspond to all $n-1$ trajectories (top), i.e., $n\,(n-1)$ input and output fields, and two cyclic trajectories with maximal length (bottom), angles $\pi\frac{n-1}{n}, \pi\frac{n+1}{n}$ for odd n. We consider here only the schemes with two maximal length cyclic trajectories.

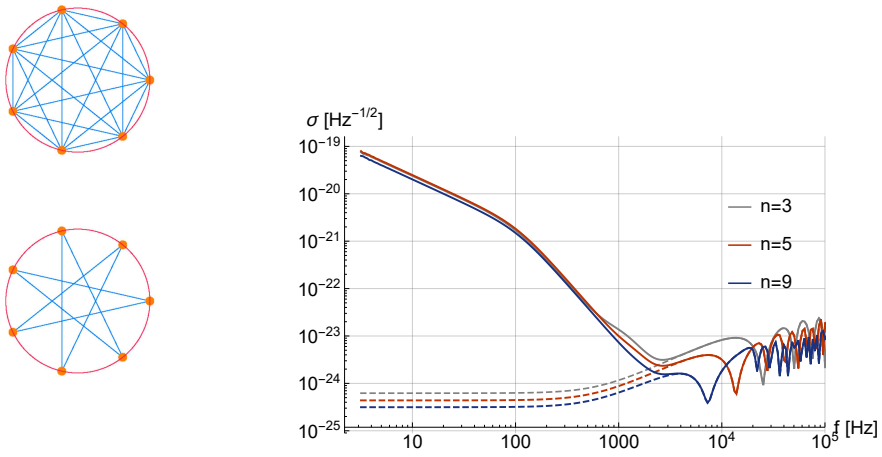

(a) (b)

Figure A.6: Extensions of the DFI scheme. (a) Extensions of the DFI triangular scheme to an arbitrary n-gon. The vertices represent the mirrors and the blue edges represent the light trajectories. (b) Comparison between the sensitivities of the different n-gon schemes: dashed lines correspond to shot-noise only and solid lines to thermal displacement noise as well. The blue, red and gray lines correspond to $n = 3, 5, 9$, respectively.

Therefore the number of input/output fields is $2n$ and the phase quadratures DFS is n-dimensional. In fig. A.6 the triangular scheme ($n = 3$) is compared to larger number of mirrors: $n = 5, 9$, where thermal displacement noise is considered. In this comparison, all the n-gons have the same radius and the intracavity power is the same (taken to be $10^5 \frac{T}{\left(1-\sqrt{R}\right)^2} \approx 3.8$ MW).

It can be observed in fig. A.6 that, assuming only shot noise, the sensitivity in the DC (static signal) limit becomes better as n is increased. More precisely, in DC the QFI goes as $I \propto n$. The reason is that the length of the trajectory goes as n which accounts for a factor of n in the response vector $\mathcal{V}$, on the other hand there is more loss due to the increased number of mirros which accounts for a factor of $\frac{1}{\sqrt{n}}$. Altogether $\mathcal{V}$ goes as $\sqrt{n}$ and thus the QFI as n. However once we add thermal displacement noise the sensitivities of the schemes coincide and only a very minor improvement is observed for larger n.

Further extensions, such as using all the $n-1$ trajectories as shown in fig. A.6 hold the promise for improved sensitivities, as they have larger DFS. We leave these extensions for future work.

A.10 Newtonian and Seismic Noise

Apart from thermal and radiation pressure noise, interferometers suffer also from newtonian and seismic noise [20, 21].

Like thermal noise, they can be modelled as random displacement vector $\mathbf{\Delta x}_{\mathrm{NN}}, \mathbf{\Delta x}_{\mathrm{S}}$ propagated to the output quadratures by a transfer matrix A. Denoting the covariance matrices of $\mathbf{\Delta x}_{\mathrm{NN}}, \mathbf{\Delta x}_{\mathrm{S}}$ as σ_{S}, σ_{NN}, we get that the QFI with these noises reads:

$$I = 4\boldsymbol{\mathcal{V}}_{+}^{\dagger}\left(MM^{\dagger} + A\left(\delta^2\mathbb{1} + \sigma_{\mathrm{NN}} + \sigma_{\mathrm{S}}\right)A^{\dagger}\right)^{-1}\boldsymbol{\mathcal{V}}_{+}. \tag{A.108}$$

Unlike thermal noise, the assumption of uncorrelated noise between mirrors is no longer correct for these noises. For example, two nearby mirrors will have correlated seismic and newtonian noises.

A.11 Calculation Outline

The QFI and QFIM are expressed using the transfer matrices $\boldsymbol{\mathcal{V}}$, M, A. In this section, we outline how these transfer matrices are calculated:

Step 1: solve the equations for the carrier amplitudes

Let us denote the input carrier amplitudes entering the cavity as $\{A_{\mathrm{in},j}\}_{j=1}^{6}$, the carrier amplitudes hitting/ reflecting inside the cavity as $\{A_{\mathrm{hit},j}\}_{j=1}^{6}$, $\{A_{\mathrm{ref},j}\}_{j=1}^{6}$, respectively, and the outgoing amplitudes as $\{A_{\mathrm{out},j}\}_{j=1}^{6}$.

Given the input carrier amplitudes $\{A_{\mathrm{in},j}\}_{j=1}^{6}$ we can solve for $\{A_{\mathrm{hit},j}\}_{j=1}^{6}$, $\{A_{\mathrm{ref},j}\}_{j=1}^{6}$, $\{A_{\mathrm{out},j}\}_{j=1}^{6}$ using the following set of input-output linear equations:

Mirror equations:

$$\begin{pmatrix} A_{\mathrm{out},j} \\ A_{\mathrm{ref},j} \end{pmatrix} = \begin{pmatrix} -\sqrt{R} & \sqrt{T} \\ \sqrt{T} & \sqrt{R} \end{pmatrix}\begin{pmatrix} A_{\mathrm{in},j} \\ A_{\mathrm{hit},j} \end{pmatrix} \tag{A.109}$$

Propagation equations:

$$A_{\mathrm{hit},j+1} = A_{\mathrm{ref},j} \tag{A.110}$$

where R, T are the reflectivity and transmissivity of the mirrors and we assume symmetric configuration of identical transmissivities. Given that all input amplitudes are also the same ($A_{\mathrm{in},j} = E$) the analytical solution for $A_{\mathrm{hit},j}, A_{\mathrm{ref},j}, A_{\mathrm{out},j}$ is

$$A_{\mathrm{hit},j} = A_{\mathrm{ref},j} = E\frac{\sqrt{T}}{1-\sqrt{R}} = E\frac{\sqrt{1+\sqrt{R}}}{\sqrt{1-\sqrt{R}}} \tag{A.111}$$

$$A_{\mathrm{out},j} = E. \tag{A.112}$$

The solution to $A_{\mathrm{hit},j}.A_{\mathrm{out},j}$ will be inserted in the equations of the sideband fields.

Regarding power amplification in our cavity: the ratio between the carrier power inside and outside the cavity is:

$$\frac{p_{\mathrm{hit}}}{p_{\mathrm{in}}} = \frac{p_{\mathrm{ref}}}{p_{\mathrm{in}}} = \frac{T}{\left(1-\sqrt{R}\right)^2}. \tag{A.113}$$

In our triangular scheme the total intracavity power is $2p_{\mathrm{hit}}$, the factor of 2 is due to the clockwise and counter-clockwise trajectories. The total input power is $6p_{\mathrm{in}}$, because there are in total 6 input fields. This yields the gain enhancement factor: $\frac{T}{3\left(1-\sqrt{R}\right)^2}$.

Step 2: solve the equations of the sideband fields The input and output sideband fields are $\begin{pmatrix} \hat{\mathbf{a}}_1 \\ \hat{\mathbf{a}}_2 \end{pmatrix}$, $\begin{pmatrix} \hat{\mathbf{b}}_1 \\ \hat{\mathbf{b}}_2 \end{pmatrix}$, respectively, as before. We introduce the intracavity sideband fields $\begin{pmatrix} \mathbf{c}_{\mathrm{hit},1} \\ \mathbf{c}_{\mathrm{hit},2} \end{pmatrix}$, $\begin{pmatrix} \hat{\mathbf{c}}_{\mathrm{ref},1} \\ \hat{\mathbf{c}}_{\mathrm{ref},2} \end{pmatrix}$ that hit and reflect from the mirrors, respectively. The transfer matrices are obtained by solving the following set of linear equations:

Mirror equation with no radiation pressure:

$$\begin{aligned} \begin{pmatrix} \hat{b}_{1,j} \\ \hat{b}_{2,j} \\ \hat{c}_{\mathrm{hit},1,j} \\ \hat{c}_{\mathrm{hit},2,j} \end{pmatrix} = & \begin{pmatrix} -\sqrt{R} & & \sqrt{T} & \\ & -\sqrt{R} & & \sqrt{T} \\ \sqrt{T} & & \sqrt{R} & \\ & \sqrt{T} & & \sqrt{R} \end{pmatrix} \begin{pmatrix} \hat{a}_{1,j} \\ \hat{a}_{2,j} \\ \hat{c}_{\mathrm{ref},1,j} \\ \hat{c}_{\mathrm{ref},2,j} \end{pmatrix} \\ & - \Delta x \cos(\pi/6)\sqrt{R}\left(\frac{\omega_0}{c}\right) \begin{pmatrix} 0 \\ A_{\mathrm{in},j} \\ 0 \\ A_{\mathrm{hit},j} \end{pmatrix} \end{aligned} \tag{A.114}$$

or *Mirror equation with radiation pressure* (see also Appendix A.6:)

$$\begin{aligned}\begin{pmatrix} \hat{b}_{1,j} \\ \hat{b}_{2,j} \\ \hat{c}_{\mathrm{hit},1,j} \\ \hat{c}_{\mathrm{hit},2,j} \end{pmatrix} = &\begin{pmatrix} -\sqrt{R} & & \sqrt{T} & \\ & -\sqrt{R} & & \sqrt{T} \\ \sqrt{T} & & \sqrt{R} & \\ & \sqrt{T} & & \sqrt{R} \end{pmatrix} \begin{pmatrix} \hat{a}_{1,j} \\ \hat{a}_{2,j} \\ \hat{c}_{\mathrm{ref},1,j} \\ \hat{c}_{\mathrm{ref},2,j} \end{pmatrix} \\ &- \Delta x \cos(\pi/6) \sqrt{R} \left(\frac{\omega_0}{c}\right) \begin{pmatrix} 0 \\ A_{\mathrm{in},j} \\ 0 \\ A_{\mathrm{hit},j} \end{pmatrix} \\ &- 2\sqrt{2} \frac{\omega_0 \sqrt{R}}{m\Omega^2 c^2} [\sqrt{I_{\mathrm{in}}} \hat{a}_{1,j} - \sqrt{I_{\mathrm{hit}}} \hat{c}_{\mathrm{hit},1,j} \\ &+ \sqrt{I_{\mathrm{out}}} \hat{b}_{1,j} - \sqrt{I_{\mathrm{hit}}} \hat{c}_{\mathrm{ref},1,j}] \begin{pmatrix} 0 \\ -\sqrt{2I_{\mathrm{hit}}} \\ 0 \\ -\sqrt{2I_{\mathrm{hit}}} \end{pmatrix}. \end{aligned} \tag{A.115}$$

Propagation equations:

$$\begin{pmatrix} \hat{c}_{\mathrm{hit},1,j+1} \\ \hat{c}_{\mathrm{hit},2,j+1} \end{pmatrix} = e^{-i\Omega \frac{L}{c}} \begin{pmatrix} \hat{c}_{\mathrm{ref},1,j} \\ \hat{c}_{\mathrm{ref},2,j} \end{pmatrix} + A_{\mathrm{ref},j} \left(\frac{\omega_0}{c}\right) \begin{pmatrix} 0 \\ h_j(f) \end{pmatrix}, \tag{A.116}$$

where $h_j(f)$ is the response to the GW in the j-th arm.

To write it explicitly let us introduce necessary notation:

The GW signal travels along an arbitrary direction given by the unit vector,

$$\mathbf{k} = (\sin(\theta)\cos(\phi), \sin(\theta)\sin(\phi), \cos(\theta)), \tag{A.117}$$

and the orthogonal unit vectors to $\boldsymbol{k}$ are

$$\mathbf{u} = (-\cos(\theta)\cos(\phi), -\cos(\theta)\sin(\phi), \sin(\theta)), \tag{A.118}$$

$$\mathbf{v} = (-\cos(\phi), \sin(\phi), 0). \tag{A.119}$$

$h_j(f)$ is then given by [24]:

$$h_j(f) = \zeta_j(f) \left(h_+ \langle n_j | e_+ | n_j \rangle + h_\times \langle n_j | e_\times | n_j \rangle \right), \tag{A.120}$$

where $e_+ = \mathbf{u} \otimes \mathbf{u} - \mathbf{v} \otimes \mathbf{v}$, $e_\times = \mathbf{u} \otimes \mathbf{v} + \mathbf{v} \otimes \mathbf{u}$ are the polarization tensors and $|n_j\rangle$ is the unit vector of the j-th arm.

The factor $\zeta_j\,(f)$ contains the dependence on the frequency and GW direction and is given by

$$\zeta_j\,(f) = E\left(\frac{\omega_0}{c}\right) L\,\mathrm{sinc}\left(\epsilon(1-\mathbf{n}_j\cdot\mathbf{k})\right)\exp\left(i\frac{1}{L}\left(\mathbf{x}_{j,1}+\mathbf{x}_{j,2}\right)\cdot\mathbf{k}\epsilon - i\epsilon\right), \quad \text{(A.121)}$$

with $\epsilon = 2\pi f L/2$ and $\mathbf{x}_{j,1}, \mathbf{x}_{j,2}$ are the positions of the mirrors.

Equations eq. (A.115), eq. (A.116) form a set of 36 linear equations for 36 variables $\hat{\mathbf{b}}_1, \hat{\mathbf{b}}_2, \hat{\mathbf{c}}_{\mathrm{ref},1}, \hat{\mathbf{c}}_{\mathrm{ref},2}, \hat{\mathbf{c}}_{\mathrm{hit},1}, \hat{\mathbf{c}}_{\mathrm{hit},2}$. We can recast these equations as:

$$L\begin{pmatrix}\hat{\mathbf{b}}_1\\ \hat{\mathbf{b}}_2\\ \hat{\mathbf{c}}_{\mathrm{ref},1}\\ \hat{\mathbf{c}}_{\mathrm{ref},2}\\ \hat{\mathbf{c}}_{\mathrm{hit},1}\\ \hat{\mathbf{c}}_{\mathrm{hit},2}\end{pmatrix} = O\begin{pmatrix}\hat{\mathbf{a}}_1\\ \hat{\mathbf{a}}_2\end{pmatrix} + K_1\boldsymbol{\Delta}\mathbf{x} + K_2\mathbf{h} \quad \text{(A.122)}$$

$$\Rightarrow\begin{pmatrix}\hat{\mathbf{b}}_1\\ \hat{\mathbf{b}}_2\\ \hat{\mathbf{c}}_{\mathrm{ref},1}\\ \hat{\mathbf{c}}_{\mathrm{ref},2}\\ \hat{\mathbf{c}}_{\mathrm{hit},1}\\ \hat{\mathbf{c}}_{\mathrm{hit},2}\end{pmatrix} = L^{-1}O\begin{pmatrix}\hat{\mathbf{a}}_1\\ \hat{\mathbf{a}}_2\end{pmatrix} + L^{-1}K_1\boldsymbol{\Delta}\mathbf{x} + L^{-1}K_2\mathbf{h}, \quad \text{(A.123)}$$

where L, O, K_1, K_2 are matrices of size $36\times 36, 36\times 12, 36\times 3, 36\times 2$, respectively. Hence the transfer matrices $M, A, \mathcal{V}$ are given by the first 12 rows of $L^{-1}O, L^{-1}K_1, L^{-1}K_2$, respectively.

A.12 GW response: Analytical Expressions of Transfer Matrix $\mathcal{V}$

We calculate the GW response, i.e., the vector of the first moments $\mathbf{d} = \mathcal{V}\mathbf{h}$, from which we can get the shot noise limit $4\mathcal{V}_{\mathrm{ph}}^{\dagger}\mathcal{V}_{\mathrm{ph}}$. Since the responce to the GW is in the phase quadratures, it suffices to calculate the 6-dimensional $\mathcal{V}_{\mathrm{ph}}$ and the corresponding $\mathbf{d}_{\mathrm{ph}} = \mathcal{V}_{\mathrm{ph}}\mathbf{h}$. We calculate it for the symmetric triangular scheme depicted in (1) in the main text. Let us introduce the required notation: L-length of the arms, A_{in}-amplitude of the incoming fields (identical for all fields), ω_0-frequency of the carrier fields, c-speed of light. All the mirrors have the same power reflectivity R (and power transmissivity $T = 1 - R$).

As shown in section Appendix A.11, The GW response in the $j-$th arm, $h_j\,(f)$, is then given by eq. (A.120), with $\zeta_j\,(f)$ given in eq. (A.121). We can observe that as $f \to 0$, $\zeta_j\,(f) \to L$ for all arms, and the response is simplified to

$$h_j\,(f) = A_{\rm in}\left(\frac{\omega_0}{c}\right) L\left(h_+\langle n_j|e_+|n_j\rangle + h_\times\langle n_j|e_\times|n_j\rangle\right). \tag{A.124}$$

We consider a cyclic trajectory, hence each h_j propagates to the k-th output mode in the following way:

$$\left(d_{\rm ph}\right)_k = \frac{T}{(1-\sqrt{R})(1-R'^{1.5})}\cdot(R'h_k + \sqrt{R'}h_{k+1} + h_{k+2}), \tag{A.125}$$

with $R' = Re^{i2\Omega L}$. Hence the full vector of output modes (clockwise and counter-clockwise) reads:

$$\mathbf{d}_{\rm ph} = \frac{(1+\sqrt{R})}{(1-R'^{3/2})}\begin{pmatrix} \begin{pmatrix} R'h_1 + \sqrt{R'}h_2 + h_3 \\ R'h_2 + \sqrt{R'}h_3 + h_1 \\ R'h_3 + \sqrt{R'}h_1 + h_2 \end{pmatrix}_{\rm L} \\ \begin{pmatrix} h_1 + \sqrt{R'}h_2 + R'h_3 \\ h_2 + \sqrt{R'}h_3 + R'h_1 \\ h_3 + \sqrt{R'}h_1 + R'h_2 \end{pmatrix}_{\rm R} \end{pmatrix}. \tag{A.126}$$

From here we can obtain the shot-noise limit. The QFIM about $h_+, h_\times$ in the shot-noise limit is given by:

$$\mathbf{h}^\dagger \mathcal{I}\,\mathbf{h} = \mathbf{d}_{\rm ph}^\dagger \mathbf{d}_{\rm ph}, \tag{A.127}$$

with $\mathbf{h} = (h_+, h_\times)^T$.

We thus calculate $\mathbf{d}_{\rm ph}^\dagger \mathbf{d}_{\rm ph}$ using eq. (A.126):

$$\begin{aligned} \mathbf{d}_{\rm ph}^\dagger \mathbf{d}_{\rm ph} =& A_{\rm in}^2\left(\frac{\omega_0}{c}\right)^2 \frac{T}{\left(1-\sqrt{R}\right)^2}\frac{T}{\left|1-R'^{1.5}\right|^2} \\ & \left[l_1\,(R)\sum_{j=1}^{3} h_j^2 + l_2\,(R')\sum_{j,m>j} h_j h_m\right], \end{aligned} \tag{A.128}$$

where $l_1\,(R) = \frac{1-R^3}{1-R}$ and $l_2\,(R') = 2{\rm Re}\left(\sqrt{R'}\frac{1-R'^{1.5}}{1-\sqrt{R'}}\right)$.

Let us now focus on the DC limit ($f \ll c/L$ and thus $R = R'$). In this limit eq. (A.128) becomes:

$$\begin{aligned}\mathbf{d}_{\mathrm{ph}}^{\dagger}\mathbf{d}_{\mathrm{ph}} =& 2A_{\mathrm{in}}^2\left(\frac{\omega_0}{c}\right)^2\frac{\left(1+\sqrt{R}\right)^2}{\left(1-R^{1.5}\right)^2}\cdot \\ &\left[\frac{1-R^3}{1-R}\sum_j h_j^2 + 2\sqrt{R}\frac{1-R^{1.5}}{1-\sqrt{R'}}\sum_{m>j} h_j h_m\right].\end{aligned} \tag{A.129}$$

Note that in the relevant limit of $T \ll 1$:

$$\frac{1-R^3}{1-R}, \sqrt{R}\frac{1-R^{1.5}}{1-\sqrt{R}} \approx 3R + O\left(T^2\right) \tag{A.130}$$

hence this expression can be further simplified to:

$$\mathbf{d}_{\mathrm{ph}}^{\dagger}\mathbf{d}_{\mathrm{ph}} \approx 6A_{\mathrm{in}}^2\left(\frac{\omega_0}{c}\right)^2\frac{\left(1+\sqrt{R}\right)^2}{\left(1-R^{1.5}\right)^2}R\left(\sum_j h_j\right)^2. \tag{A.131}$$

The coefficients of the bilinear terms of $h_+, h_\times$ in eqs. (A.129) and (A.131) correspond to the FIM elements (eq. (A.128)). It can be shown that the coefficient of $h_+h_\times$ vanishes , hence the FIM is diagonal in the $h_+, h_\times$ basis. Note that

$$\begin{aligned}\sum_j h_j &= Lh_+\sum_j \langle n_j|e_+|n_j\rangle + Lh_\times\sum_j \langle n_j|e_\times|n_j\rangle \\ &= \frac{3}{2}Lh_+\mathrm{Tr}_{x-y}\left(e_+\right) + \frac{3}{2}Lh_\times\mathrm{Tr}_{x-y}\left(e_\times\right) \\ &= \frac{3}{2}Lh_+\mathrm{Tr}_{x-y}\left(e_+\right).\end{aligned} \tag{A.132}$$

In the second equality we use the fact that $\sum_j |n_j\rangle\langle n_j|$ is proportional to the projection operator on the $x-y$ plane: $\sum_j |n_j\rangle\langle n_j| = \frac{3}{2}\Pi_{x-y}$, , hence $\sum_j \langle n_j|\bullet|n_j\rangle = \frac{3}{2}\mathrm{Tr}_{x-y}\left(\bullet\right)$. In the third equality we use the fact that $\mathrm{Tr}_{x-y}\left(e_\times\right) = 0$, because:

$$\mathrm{Tr}_{x-y}\left(e_\times\right) = 2\langle u|\Pi_{x-y}|v\rangle = 0. \tag{A.133}$$

Hence combining eqs. eq. (A.131), eq. (A.132), we get that the minimal variance is

about h_+ (maximal eigenvalue of the FIM) and it reads:

$$\begin{aligned}\sigma = \Delta h_+ &= \frac{1}{2\sqrt{||V^\dagger \mathcal{V}||}} \\ \Rightarrow \Delta h_+ &\approx \frac{1}{2A_{\text{in}}\left(\frac{\omega_0}{c}\right) L|\text{Tr}_{x-y}\left(e_+\right)|\sqrt{13.5\frac{\left(1+\sqrt{R}\right)^2}{\left(1-R^{1.5}\right)^2}R}} \\ &= \frac{1}{2A_{\text{in}}\left(\frac{\omega_0}{c}\right) L\sin\left(\theta\right)^2\sqrt{13.5\frac{\left(1+\sqrt{R}\right)^2}{\left(1-R^{1.5}\right)^2}R}}.\end{aligned} \tag{A.134}$$

A.13 Displacement Response: Analytical Expression of Transfer Matrix A

Each mirror displacement Δx_j is coupled to a single output mode: $\sum_i \left(A_{\text{ph}}\right)_{i,j}\Delta x_j$, where A_{ph} is the transfer matrix. Let us define the vector $d_{\Delta x} = A_{\text{ph}}\mathbf{\Delta x}$. We find the propagation into the clockwise cyclic trajectory and from symmetry we get the propagation into the counter clockwise trajectory: It can be observed that for every j,k the coefficient of Δx_j in $(d_{\Delta x})_{j+k,\text{L}}$ is identical to its coefficient in $(d_{\Delta x})_{j-k,\text{R}}$, where by $j \pm k$ we mean mod 3. Observe that for every $j \neq 0$ the coefficient of Δx_j in $(d_{\Delta x})_{j+k,\text{L}}$ is equal to

$$-A_{\text{in}}\left(\frac{\omega_0}{c}\right)\cos\left(\pi/6\right)\frac{\left(1+\sqrt{R}\right)\left(R'\right)^{k/2}}{\left(1-R'^{3/2}\right)}, \tag{A.135}$$

the coefficient of Δx_j in b_j $(k=0)$ is equal to

$$\begin{aligned}&-A_{\text{in}}\left(\frac{\omega_0}{c}\right)\cos\left(\pi/6\right)\left(\sqrt{R}+\frac{\left(1+\sqrt{R}\right)\left(R'\right)^{3/2}}{\left(1-R'^{3/2}\right)}\right) \\ &= -A_{\text{in}}\left(\frac{\omega_0}{c}\right)\cos\left(\pi/6\right)\left(\frac{\sqrt{R}+R'^{3/2}}{1-R'^{3/2}}\right).\end{aligned} \tag{A.136}$$

Hence in the DC limit the transfer matrix of the displacement vector, A_{ph}, reads:

$$A_{\text{ph}} = -A_{\text{in}}\left(\frac{\omega_0}{c}\right)\cos\left(\pi/6\right)\frac{\sqrt{R}}{\left(1-R^{3/2}\right)}\cdot \tag{A.137}$$

$$\begin{pmatrix} \begin{pmatrix}1+R\\1+\sqrt{R}\\\sqrt{R}+R\end{pmatrix}_{\text{L}} & \begin{pmatrix}\sqrt{R}+R\\1+R\\1+\sqrt{R}\end{pmatrix}_{\text{L}} & \begin{pmatrix}1+\sqrt{R}\\\sqrt{R}+R\\1+R\end{pmatrix}_{\text{L}} \\ \begin{pmatrix}1+R\\\sqrt{R}+R\\1+\sqrt{R}\end{pmatrix}_{\text{R}} & \begin{pmatrix}1+\sqrt{R}\\1+R\\\sqrt{R}+R\end{pmatrix}_{\text{R}} & \begin{pmatrix}\sqrt{R}+R\\1+\sqrt{R}\\1+R\end{pmatrix}_{\text{R}} \end{pmatrix} \tag{A.138}$$

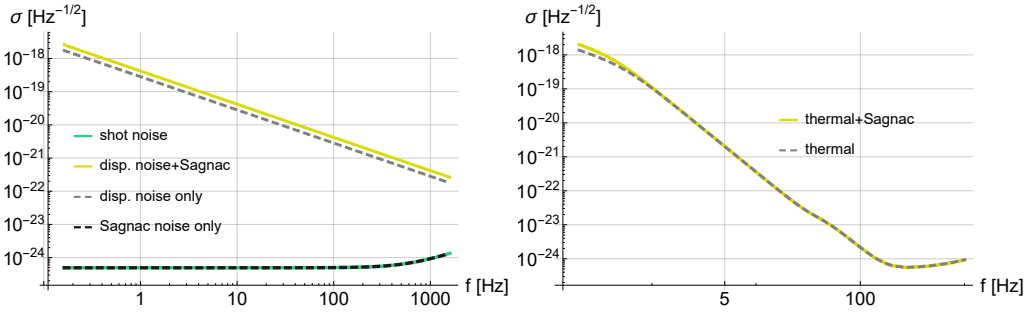

Figure A.7: Sagnac Effect. Left: sensitivity profiles with *white infinite* displacement and Sagnac noises. The bottom green (solid) line corresponds to the shot noise limit. The top yellow (solid) line corresponds to both infinite displacement and Sagnac noises. The dashed gray (top) and black (bottom) lines correspond to displacement and Sagnac noise only, respectively. Right: Comparison between thermal noise only (dashed, grey line) and thermal noise with infinite Sagnac noise (yellow, solid curve). The Sagnac noise almost does not change the sensitivity profile; its effect becomes non-negligible only in the limit of very poor sensitivity.

Comparing with the DC limit of eq. (A.126), we can observe that the GW response is a linear combination of the vector of $A_{\rm ph}$, hence the DC divergence of the SD.

A.14 Sagnac Effect

Since our proposed interferometers have a non-zero area, a rotation, such as the rotation of the Earth, would induce a phase shift. This unwanted phase shift is an additional noise source that should be accounted for.

In this section we calculate this effect and find the contribution to the noise budget. Denoting the rotation axis as z axis and the rotation frequency ω_r, by moving to the rotating frame the first order correction (in $\omega_r L/c$) to the flat metric reads:

$$h = \begin{pmatrix} 0 & \frac{\omega_r}{c} y & -\frac{\omega_r}{c} x & 0 \\ \frac{\omega_r}{c} y & 0 & 0 & 0 \\ -\frac{\omega_r}{c} x & 0 & 0 & 0 \\ 0 & 0 & 0 & 0 \end{pmatrix}. \tag{A.139}$$

Given a light that propagates in direction $\mathbf{n}$ and a carrier frequency ω_0, the resulting phase shift reads:

$$\begin{aligned} \partial_{\mathbf{n}} \phi_s &= -\frac{\omega_0}{2c} h^{\mu\nu} n_\mu n_\nu \\ \Rightarrow \phi_s &= -\frac{\omega_0}{2c} \int_0^L n_i n_j h_{i,j} \left(ct_0 + \xi, \boldsymbol{x_0} + \xi \boldsymbol{n}\right) \mathrm{d}\xi. \end{aligned} \tag{A.140}$$

Inserting the correction to the metric due to rotation, eq. (A.139), yields:

$$n_i n_j h_{i,j}\left(ct,\mathbf{r}\right) = \begin{pmatrix} -1 & n_x & n_y & n_z \end{pmatrix} \frac{\omega_r}{c} \begin{pmatrix} 0 & y & -x & 0 \\ y & 0 & 0 & 0 \\ -x & 0 & 0 & 0 \\ 0 & 0 & 0 & 0 \end{pmatrix} \begin{pmatrix} -1 \\ n_x \\ n_y \\ n_z \end{pmatrix} \tag{A.141}$$
$$= 2\omega_r/c\left(\mathbf{n}_{x-y} \times \mathbf{r}_{x-y}\right),$$

where $\mathbf{n}_{x-y}$, $\mathbf{r}_{x-y}$ are the projections of $\mathbf{n}$ and $\mathbf{r}$ onto the $x-y$ plane. From here we can calculate the phase shift generated in each arm (given a cyclic trajectory). This expression can be further simplified for straight arms where the trajectory can be parameterized as $\mathbf{r}\left(\xi\right) = \mathbf{r}_j + \xi\hat{n}_j$, and thus $\hat{n}_j \times \mathbf{r}_j = \mathbf{r}_{j+1} \times \mathbf{r}_j$. Summing over all the phases accumulated in a cyclic trajectory yields the well-known Sagnac phase shift $\sum_j \phi_j = -\frac{\omega_r\omega_0}{c^2}\sum_j \mathbf{r}_{j+1} \times \mathbf{r}_j = -2\frac{\omega_r\omega_0}{c^2}A$. In our case, since all the ports are open, the shift in each output port will be different. Once we have the different phase shifts $\left\{\phi_j\right\}_{j=1}^{3}$, they are being propagated to the output ports in the same manner as in eq. (A.126), yielding:

$$\mathbf{d}_{\text{Sagnac}} = \frac{(1+\sqrt{R})}{(1-R'^{3/2})} \begin{pmatrix} \begin{pmatrix} R'\phi_1 + \sqrt{R'}\phi_2 + \phi_3 \\ R'\phi_2 + \sqrt{R'}\phi_3 + \phi_1 \\ R'\phi_3 + \sqrt{R'}\phi_1 + \phi_2 \end{pmatrix}_{\text{L}} \\ -\begin{pmatrix} \phi_1 + \sqrt{R'}\phi_2 + R'\phi_3 \\ \phi_2 + \sqrt{R'}\phi_3 + R'\phi_1 \\ \phi_3 + \sqrt{R'}\phi_1 + R'\phi_2 \end{pmatrix}_{\text{R}} \end{pmatrix}. \tag{A.142}$$

Given a fixed rotation frequency (Ω_r) and axis, such as the rotation of earth, this effect results in a systematic dc noise. In that case it should not affect the sensitivity since: 1. as a systematic noise it can be deducted. 2. it appears only on dc, in which the SD diverges anyway.

Let us address the case of random AC rotations where this noise cannot be accounted as systematic. In this case, $\mathbf{d}_{\text{Sagnac}}$ is a Gaussian noise and we include it in the QFIM expression along with the displacement noise, written as

$$I = 4\mathcal{V}^\dagger\left(MM^\dagger + \delta^2 AA^\dagger + \mathbf{d}_{\text{Sagnac}}\mathbf{d}_{\text{Sagnac}}^\dagger\right)^{-1}\mathcal{V}. \tag{A.143}$$

Let us now examine the effect of this noise and in particular whether it has the same effect as displacement noise. The results are shown in fig. A.7. The effect of Sagnac noise is quite negligible compared to the displacement noise. The curve

of Sagnac noise alone, even infinite Sagnac noise, coincides with the shot noise limit. The reason for this is that in the dc limit the overlap between the Sagnac noise (eq. (A.142)) and the GW signal (eq. (A.126)) is very small, they are almost orthogonal. In this limit the GW signal is close to symmetric while the Sagnac noise is close to anti symmetric. The effect of the Sagnac noise becomes more pronounced in the limit of large displacement noise where the contribution of the small overlap is non-negligible.

A.15 Comparison with Standard Sagnac Interferometers

In this section, we compare the performance of our triangular symmetric DFI scheme (fig. A.8(a) top) with the performance of the standard triangular Sagnac interferometer (fig. A.8(a) bottom). The standard triangular Sagnac interferometer has the same geometry as our DFI scheme: 3 mirrors that form a triangle, but unlike the DFI scheme only one port is open and 2 other ports are close. Hence the standard Sagnac scheme has two input/ output fields, while our DFI scheme has six input/output.

Since the Sagnac interferometer has 2 outputs and 3 mirrors it does not necessarily have a DFS. In practice, due to symmetry, the Sagnac interferometer has a DFS in dc, but does not have a DFS at higher frequencies (in dc $\text{rank}\,(A) = 1$). We thus expect our DFI scheme to outperform the standard Sagnac scheme in the presence of strong displacement noise.

This expectation is confirmed in the numerical results shown in fig. A.8(b), where we compare the performance of the interferometers given phase quadratures measurement with realistic noise profile (thermal noise and radiation pressure). In this comparison the intracavity power is the same. It can be observed that the symmetric DFI outperforms the Sagnac interferometer in almost the entire frequency range. At high frequencies, the symmetric DFI has a better shot noise limit, which accounts for a better sensitivity in this regime. At lower frequencies, the RPN and displacement noise are dominant. The noise resilient subspaces of the symmetric DFI, i.e., DFS and pseudo-DFS, enable better sensitivity in this regime. Interestingly, despite the fact that the Sagnac interferometer has a DFS in dc, its dc divergence is much worse than that of the symmetric DFI.

We remark that the standard Sagnac and symmetric DFI differ only in the mirrors transmissivities (see fig. A.8(a)). This raises the question of what are the optimal transmissivities of the mirrors? We performed numerical optimization of

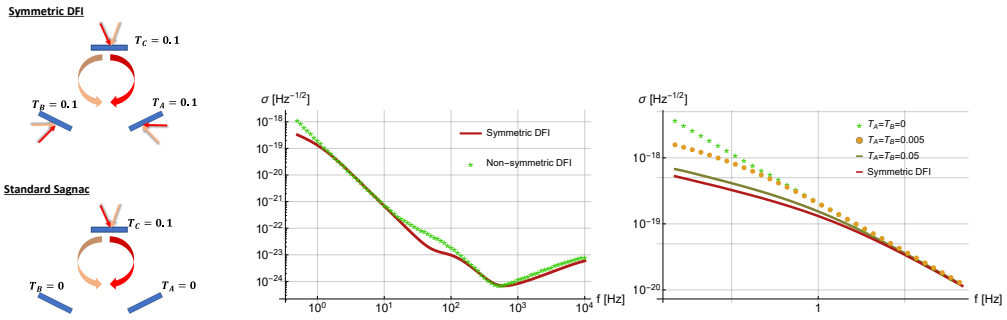

(a) (b) (c)

Figure A.8: Comparison of DFI and Sagnac Interferometers. (a) Top: our symmetric DFI interferometer, bottom: standard triangular Sagnac interferometer, where only one port is open. (b) Sensitivity comparison between the standard triangular Sagnac and the symmetric DFI given phase quadratures measurement and realistic noise profile (RPN and thermal noise). (c) Sensitivity comparison, at low frequencies, between different transmissivity configurations, illustrating the optimality of the symmetric DFI.

the sensitivity as a function of the mirrors' transmissivities, with the constraint of $0 \leq T_A, T_B, T_C \leq 0.1$ and fixed intracavity power. We observed that the optimal values correspond to our symmetric DFI configuration: $T_A, T_B, T_C = 0.1$. These results are illustrated in fig. A.8(c) and they establish the optimality of the symmetric DFI scheme analyzed in the work.

Appendix B

SUPPLEMENTARY MATERIAL FOR WAVEFORM ESTIMATION USING KALMAN FILTERS

B.1 Two-Photon Formalism for the Signal Susceptibility

We consider a detuned Fabry-Pérot-Michelson interferometer whose differential mode couples linearly to a classical strain signal $h(t)$. 'Detuned' here means the carrier laser frequency ω_0 is offset by Δ from the cavity's resonance. The differential mode (responsive to h) is well approximated as a single optical cavity mode with annihilation operator $\hat{a}(t)$, detuning Δ, and amplitude-decay rate γ (half-width at half-maximum). The interaction Hamiltonian is

$$H_{int} = g h(t) \hat{X}, \qquad \hat{X} = \frac{\hat{a} + \hat{a}^\dagger}{\sqrt{2}}, \tag{B.1}$$

where g is an effective coupling (set by circulating power and arm length), and $\hat{X}$ is the intracavity amplitude quadrature (with $\langle \hat{X} \rangle = 0$ in steady state). Its conjugate is $\hat{P} = (\hat{a} - \hat{a}^\dagger)/(i\sqrt{2})$, satisfying $[\hat{X}, \hat{P}] = i$. Physically, $h(t)$ induces an amplitude-phase modulation of the light via this X-quadrature coupling.

Heisenberg-Langevin equations. Including cavity loss and detuning, the linearized equations of motion in the Fourier domain ($\dot{Q} \to i\Omega Q(\Omega)$) read [74],

$$(\gamma - i\Omega)\hat{X}(\Omega) = \sqrt{2\gamma}\hat{X}_{in}(\Omega) - \Delta\hat{P}(\Omega), \tag{B.2}$$

$$(\gamma - i\Omega)\hat{P}(\Omega) = \sqrt{2\gamma}\hat{P}_{in}(\Omega) + \Delta\hat{X}(\Omega) - \frac{g}{\hbar}h(\Omega). \tag{B.3}$$

Here $\hat{X}_{in}, \hat{P}_{in}$ are the vacuum-noise quadratures entering at the dark port.

Input-output relations. The output quadratures at the detection port are given by the standard boundary conditions,

$$\hat{X}_{out}(\Omega) = -\hat{X}_{in}(\Omega) + \sqrt{2\gamma}\hat{X}(\Omega), \qquad \hat{P}_{out}(\Omega) = -\hat{P}_{in}(\Omega) + \sqrt{2\gamma}\hat{P}(\Omega). \tag{B.4}$$

Susceptibility vector. Solving the intracavity equations and substituting into the input-output relations, one isolates the terms proportional to $h(\Omega)$. The result can

be written as

$$\begin{pmatrix}\hat{X}_{out}(\Omega)\\ \hat{P}_{out}(\Omega)\end{pmatrix} = \underbrace{\frac{g\sqrt{2\gamma}}{(\gamma - i\Omega)^2 + \Delta^2}\begin{pmatrix}\Delta\\ -\gamma + i\Omega\end{pmatrix}}_{\vec{\chi}(\Omega)} h(\Omega) + (\text{vacuum noise terms}). \tag{B.5}$$

We thus identify the *two-photon susceptibility vector*

$$\boxed{\vec{\chi}(\Omega) = \begin{pmatrix}\chi_x(\Omega)\\ \chi_p(\Omega)\end{pmatrix} \equiv \frac{g\sqrt{2\gamma}}{(\gamma - i\Omega)^2 + \Delta^2}\begin{pmatrix}\Delta\\ -\gamma + i\Omega\end{pmatrix}.} \tag{B.6}$$

A resonant cavity ($\Delta = 0$) thus places all signal in $\hat{P}_{out}$, while detuning ($\Delta \neq 0$) rotates it into both quadratures in a frequency-dependent fashion.

It is to be noted here that the susceptibility matrix is complex and when using real quadratures, we decompose this as

$$\chi = \begin{pmatrix}Re[\chi_x]\\ Re[\chi_p]\\ Im[\chi_x]\\ Im[\chi_p]\end{pmatrix} = \begin{pmatrix}R_1\\ R_2\\ I_1\\ I_2\end{pmatrix}. \tag{B.7}$$

B.2 Normalization of Quadrature Operators for Finite Integration Time

In the two-photon formalism [75], the output field at the dark port is described by an annihilation operator $\hat{a}(t)$ in a frame rotating at the carrier frequency. In the time domain it obeys the canonical commutation

$$[\hat{a}(t), \hat{a}^\dagger(t')] = \delta(t - t'). \tag{B.8}$$

To analyze a finite measurement interval of duration T, we define the two-photon Fourier-domain mode at sideband frequency Ω by

$$\hat{a}_T(\Omega) = \frac{1}{\sqrt{T}}\int_{-T/2}^{T/2} dt e^{i\Omega t}\hat{a}(t), \qquad \hat{a}_T^\dagger(-\Omega) = \frac{1}{\sqrt{T}}\int_{-T/2}^{T/2} dt e^{-i\Omega t}\hat{a}^\dagger(t). \tag{B.9}$$

The $1/\sqrt{T}$ prefactor ensures

$$[\hat{a}_T(\Omega), \hat{a}_T^\dagger(\Omega')] = sinc[\frac{T}{2}(\Omega - \Omega')]. \tag{B.10}$$

For a discrete transformation grid or long integration time, this leads to

$$[\hat{a}_T(\Omega), \hat{a}_T^\dagger(\Omega')] = \delta_{\Omega,\Omega'}, \tag{B.11}$$

so that modes at different discrete frequencies are independent.

We then form the two-photon quadrature operators for each Ω,

$$\hat{x}(\Omega) = \frac{\hat{a}_T(\Omega) + \hat{a}_T^\dagger(-\Omega)}{\sqrt{2}}, \qquad \hat{p}(\Omega) = \frac{\hat{a}_T(\Omega) - \hat{a}_T^\dagger(-\Omega)}{i\sqrt{2}}, \tag{B.12}$$

which obey the canonical commutation

$$[\hat{x}(\Omega), \hat{p}(\Omega')] = i\delta_{\Omega,\Omega'}. \tag{B.13}$$

In particular, for each fixed Ω, $\hat{x}(\Omega)$ and $\hat{p}(\Omega)$ behave as dimensionless position and momentum operators.

Vacuum Variances and Spectral Density

In the vacuum state $|0\rangle$, $\langle 0|\hat{a}_T^\dagger(\Omega)\hat{a}_T(\Omega')|0\rangle = 0$ and $\langle 0|\hat{a}_T(\Omega)\hat{a}_T^\dagger(\Omega')|0\rangle = \delta_{\Omega,\Omega'}$. Hence

$$\langle 0|\hat{x}(\Omega)\hat{x}(\Omega')|0\rangle = \frac{1}{2}\left\langle 0\middle|\hat{a}_T(\Omega)\hat{a}_T^\dagger(-\Omega')\middle|0\right\rangle = \frac{1}{2}\delta_{\Omega,\Omega'}, \tag{B.14}$$

and similarly

$$\langle 0|\hat{p}(\Omega)\hat{p}(\Omega')|0\rangle = \frac{1}{2}\delta_{\Omega,\Omega'}. \tag{B.15}$$

In particular, for the same mode $\Omega = \Omega'$,

$$\langle 0|\hat{x}(\Omega)^2|0\rangle = \langle 0|\hat{p}(\Omega)^2|0\rangle = \tfrac{1}{2}. \tag{B.16}$$

To connect to the noise spectral density, recall that for a stationary mode the symmetrized PSD is defined by

$$S_{xx}(\Omega)\delta_{\Omega,\Omega'} = \left\langle \frac{\hat{x}(\Omega)\hat{x}^\dagger(\Omega') + \hat{x}^\dagger(\Omega')\hat{x}(\Omega)}{2} \right\rangle. \tag{B.17}$$

Since $\hat{x}^\dagger(\Omega) = \hat{x}(-\Omega)$ and $\langle 0|\hat{x}(\Omega)\hat{x}(-\Omega)|0\rangle = \frac{1}{2}$, one finds

$$S_{xx}(\Omega) = \frac{1}{2}, \qquad S_{pp}(\Omega) = \frac{1}{2}, \tag{B.18}$$

in units with $\hbar = 1$. Thus each two-photon quadrature mode carries a vacuum noise floor of $1/2$ in its spectral density.

Because of the $1/\sqrt{T}$ normalization in $\hat{a}_T(\Omega)$, the total variance of the integrated quadrature $\frac{1}{\sqrt{T}}\int_0^T \hat{x}(t)dt$ remains $1/2$, rather than growing with T. This normalization underlies all subsequent estimation of signal and noise in the quadrature basis.

B.3 Heterodyne Readout For Seeding Filters

When the optimal homodyne angle $\phi_{opt}(\Omega)$ is unknown, we cannot pre-align a single-quadrature measurement to the signal displacement $\vec{\chi}(\Omega)h(\Omega)$. Instead, a *heterodyne* readout is used to access two *commuting* real quadratures simultaneously, at the expense of a 3dB noise penalty. In the two-photon basis of real quadratures

$$\hat{\mathbf{q}}(\Omega) = \frac{1}{\sqrt{T}}\begin{pmatrix} \hat{x}_R(\Omega) \\ \hat{p}_R(\Omega) \\ \hat{x}_I(\Omega) \\ \hat{p}_I(\Omega) \end{pmatrix}, \tag{B.19}$$

we choose two commuting quadratures

$$\hat{q}_1(\Omega) = \hat{x}_R(\Omega), \qquad \hat{q}_3(\Omega) = \hat{x}_I(\Omega), \tag{B.20}$$

so that $[\hat{q}_1, \hat{q}_3] = 0$. These yield the measurements

$$\hat{y}_1 = \hat{q}_1 + n_1, \qquad \hat{y}_2 = \hat{q}_3 + n_2, \tag{B.21}$$

where n_1, n_2 are independent zero-mean Gaussian vacuum noises with $\mathrm{Var}(n_i) = \frac{1}{2}$.

Signal-induced means. Decomposing the complex susceptibility vector $\vec{\chi}(\Omega) = (\chi_x, \chi_p)^T$ into real parts $\{R_1, R_2\}$ and imaginary parts $\{I_1, I_2\}$,

$$\chi_x = R_1 + iI_1, \quad \chi_p = R_2 + iI_2, \tag{B.22}$$

the total real-quadrature displacement from a complex strain $h(\Omega) = h_c + ih_s$ is

$$\Delta\mathbf{q} = \sqrt{T}h_c\begin{pmatrix} R_1 \\ R_2 \\ I_1 \\ I_2 \end{pmatrix} + \sqrt{T}h_s\begin{pmatrix} -I_1 \\ -I_2 \\ R_1 \\ R_2 \end{pmatrix}. \tag{B.23}$$

In particular, the two measured quadratures acquire means

$$\begin{aligned}\langle y_1\rangle &= \sqrt{T}(R_1 h_c - I_1 h_s) = \sqrt{T}|h|\big(R_1\cos\phi - I_1\sin\phi\big),\\ \langle y_2\rangle &= \sqrt{T}(I_1 h_c + R_1 h_s) = \sqrt{T}|h|\big(I_1\cos\phi + R_1\sin\phi\big),\end{aligned} \tag{B.24}$$

where we have written $h_c = |h|\cos\phi$ and $h_s = |h|\sin\phi$.

Variances. Since the output is a displaced vacuum in each real quadrature, the vacuum fluctuations in $\hat{q}_1, \hat{q}_3$ contribute $\frac{1}{2}$ each, so the total variance of each y_i is $\frac{1}{2}$.

Fisher information and CRBs. Treating (y_1, y_2) as two independent Gaussian observations of means μ_1, μ_2 in (B.24) and common variance $\sigma^2 = \frac{1}{2}$, the Fisher information matrix for $\theta_1 = |h|$, $\theta_2 = \phi$ is

$$I_{ij} = \sum_{k=1}^{2} \frac{1}{\sigma^2}\frac{\partial\mu_k}{\partial\theta_i}\frac{\partial\mu_k}{\partial\theta_j}. \tag{B.25}$$

The required derivatives then are

$$\begin{aligned}\frac{\partial\mu_1}{\partial|h|} &= \sqrt{T}(R_1\cos\phi - I_1\sin\phi), \quad \frac{\partial\mu_1}{\partial\phi} &&= -\sqrt{T}|h|(R_1\sin\phi + I_1\cos\phi),\\ \frac{\partial\mu_2}{\partial|h|} &= \sqrt{T}(I_1\cos\phi + R_1\sin\phi), \quad \frac{\partial\mu_2}{\partial\phi} &&= \sqrt{T}|h|(R_1\cos\phi - I_1\sin\phi).\end{aligned} \tag{B.26}$$

Summing the squares, we find

$$I_{|h|,|h|} = 2T(R_1^2 + I_1^2), \qquad I_{\phi,\phi} = 2T|h|^2(R_1^2 + I_1^2), \qquad I_{|h|,\phi} = 0. \tag{B.27}$$

Hence the classical Cramér-Rao bounds are

$$\mathrm{Var}(|\hat{h}|) \geq \frac{1}{2T(R_1^2 + I_1^2)}, \qquad \mathrm{Var}(\hat{\phi}) \geq \frac{1}{2T|h|^2(R_1^2 + I_1^2)}. \tag{B.28}$$

While optimal measurements based on the values of the susceptibility vector are possible, we do not seek such optimality here. Instead, these measurements provide the initial (non-optimal) heterodyne estimates of amplitude $|h|$ and phase ϕ, when the optimal homodyne angle is unknown.

B.4 Optimal Quadratures for Measuring $|h|$

We work in the normalized real two-photon basis at sideband frequency Ω,

$$\hat{\mathbf{q}}(\Omega) = \frac{1}{\sqrt{T}}\begin{pmatrix}\hat{x}_R(\Omega)\\ \hat{p}_R(\Omega)\\ \hat{x}_I(\Omega)\\ \hat{p}_I(\Omega)\end{pmatrix}, \tag{B.29}$$

where T denotes the measurement time and each component has a vacuum variance of $\frac{1}{2}$.

Next, we introduce the complex signal $h(\Omega) = h_c + ih_s$ which acts to displace $\hat{\mathbf{q}}$ by

$$\langle \hat{\mathbf{q}} \rangle = \sqrt{T}\big(h_s \mathbf{R} + h_c \mathbf{I}\big), \tag{B.30}$$

where we have defined the real displacement directions

$$\mathbf{R} = \begin{pmatrix} R_1 \\ R_2 \\ I_1 \\ I_2 \end{pmatrix}, \qquad \mathbf{I} = \begin{pmatrix} -I_1 \\ -I_2 \\ R_1 \\ R_2 \end{pmatrix}, \tag{B.31}$$

and it can be readily checked that $\mathbf{R} \cdot \mathbf{I} = 0$. For convenience, we also set $\|\mathbf{R}\| = \|\mathbf{I}\| = R_{tot}$.

We then rewrite eq. (B.30) as,

$$\langle \hat{\mathbf{q}} \rangle = \sqrt{T}|h|\big(\cos\phi \mathbf{R} + \sin\phi \mathbf{I}\big) \equiv \sqrt{T}|h|\mathbf{v}(\phi), \qquad \mathbf{v}(\phi) = \cos\phi \mathbf{R} + \sin\phi \mathbf{I}. \tag{B.32}$$

where $\mathbf{v}(\phi)$ denotes the vector for signal displcement in the real quadrature basis.

To isolate the pure direction (independent of magnitude), we define the corresponding unit vector

$$\hat{\mathbf{v}}(\phi) = \frac{\mathbf{v}(\phi)}{R_{tot}}. \tag{B.33}$$

Projecting onto this "signal-aligned" direction yields the optimal single-parameter quadrature measurement. Explicitly, we have

$$\hat{y}_{opt} = \hat{\mathbf{v}}(\phi)^T \hat{\mathbf{q}} = \frac{1}{R_{tot}}\Big[\cos\phi(R_1\hat{q}_1 + R_2\hat{q}_2 + I_1\hat{q}_3 + I_2\hat{q}_4) \tag{B.34}$$

$$+ \sin\phi(-I_1\hat{q}_1 - I_2\hat{q}_2 + R_1\hat{q}_3 + R_2\hat{q}_4)\Big]. \tag{B.35}$$

By construction, this quadrature is maximally sensitive to the signal. Its expectation and variance follow directly:

$$\langle \hat{y}_{opt} \rangle = \hat{\mathbf{v}}^T \langle \hat{\mathbf{q}} \rangle = \sqrt{T}|h|R_{tot}, \qquad \mathrm{Var}[\hat{y}_{opt}] = \frac{1}{2}. \tag{B.36}$$

Therefore, the estimator $\big|\tilde{h}\big| = \langle \hat{y}_{opt} \rangle / (\sqrt{T}R_{tot})$ is unbiased and achieves variance

$$\Delta^2|\tilde{h}| = \frac{1}{2TR_{tot}^2}, \tag{B.37}$$

which exactly saturates the single-parameter homodyne quantum Cramér-Rao bound for estimating $|h|$ (derived in Appendix B.6).

B.5 Construction of a Commutating Pair to the Optimal Measurement

To retain phase information while leaving the optimal quadrature $\hat{y}_{opt}$ undisturbed, we introduce the **orthogonal-commutating** quadrature. This additional quadrature picks up the phase error without adding measurement back-action. We define,

$$\hat{\mathbf{w}}(\phi) = \frac{1}{R_{tot}} \left[\cos\phi \begin{pmatrix} I_1 \\ -I_2 \\ -R_1 \\ R_2 \end{pmatrix} + \sin\phi \begin{pmatrix} R_1 \\ -R_2 \\ I_1 \\ -I_2 \end{pmatrix} \right] \tag{B.38}$$

by construction orthogonal to $\hat{\mathbf{v}}(\phi)$, so that $\hat{\mathbf{v}}(\phi).\hat{\mathbf{w}}(\phi) = 0$. We then define the corresponding operator

$$\hat{y}_{\perp} = \hat{\mathbf{w}}(\phi)^T \hat{\mathbf{q}}(\Omega). \tag{B.39}$$

Using the nonzero commutators $[\hat{q}_1, \hat{q}_2] = [\hat{q}_3, \hat{q}_4] = i$, we can verify

$$[\hat{y}_{opt}, \hat{y}_{\perp}] = \frac{i}{R_{\text{tot}}^2} \left(\mathbf{v}^T \Omega \mathbf{w} \right) = 0, \tag{B.40}$$

where

$$\Omega = \begin{pmatrix} 0 & 1 & 0 & 0 \\ -1 & 0 & 0 & 0 \\ 0 & 0 & 0 & 1 \\ 0 & 0 & -1 & 0 \end{pmatrix}, \tag{B.41}$$

is the symplectic form in the real quadrature basis. Moreover, since different frequencies Ω correspond to independent optical modes, observables at distinct frequencies automatically commute.

In summary, the pair $\{\hat{y}_{opt}(\Omega), \hat{y}_{\perp}(\Omega)\}$ constitutes a fully commuting set at each frequency. Measuring $\hat{y}_{opt}$ gives the best estimate of the amplitude $|h|$, while $\hat{y}_{\perp}$ simultaneously provides sensitivity to the signal phase ϕ, all without introducing any back-action trade-off.

B.6 Quantum Fisher Information and Ultimate QCRB

Since the joint output state at frequency Ω is a pure Gaussian displaced by $\sqrt{T}|h|\mathbf{v}(\phi)$ in the four-dimensional real quadrature space, we can show that the quantum Fisher information matrix for $\theta_1 = |h|$, $\theta_2 = \phi$ is

$$\mathcal{F}_{|h|,|h|} = 4\text{Var}\big[G_{|h|}\big], \qquad \mathcal{F}_{\phi,\phi} = 4\text{Var}\big[G_{\phi}\big], \qquad \mathcal{F}_{|h|,\phi} = 0, \tag{B.42}$$

where the generators of displacements are

$$G_{|h|} = \sqrt{T}\hat{\mathbf{v}}(\phi)^T\hat{\mathbf{q}}, \qquad G_{\phi} = \sqrt{T}|h|\hat{\mathbf{v}}'(\phi)^T\hat{\mathbf{q}}, \tag{B.43}$$

and $\hat{\mathbf{v}}$ is defined in (B.35) and $\mathbf{v}'$ is its phi derivative. Since each component of $\hat{\mathbf{q}}$ has vacuum variance $\frac{1}{2}$ and $\|\mathbf{v}\| = \|\mathbf{v}'\| = R_{tot}$, we obtain

$$\mathrm{Var}[G_{|h|}] = \tfrac{1}{2}TR_{tot}^2, \qquad \mathrm{Var}[G_\phi] = \tfrac{1}{2}T|h|^2R_{tot}^2, \tag{B.44}$$

and hence

$$\mathcal{F}_{|h|,|h|} = 2TR_{tot}^2, \quad \mathcal{F}_{\phi,\phi} = 2T|h|^2R_{tot}^2. \tag{B.45}$$

The quantum Cramér-Rao bounds (QCRBs) then follow:

$$\mathrm{Var}(\widehat{|h|}) \geq \frac{1}{\mathcal{F}_{|h|,|h|}} = \frac{1}{2TR_{tot}^2}, \qquad \mathrm{Var}(\hat{\phi}) \geq \frac{1}{\mathcal{F}_{\phi,\phi}} = \frac{1}{2T|h|^2R_{tot}^2}. \tag{B.46}$$

Comparing (B.28) and (B.46) shows that the heterodyne measurement is in general *suboptimal* by the factor $\dfrac{R_{tot}^2}{R_1^2 + I_1^2} \geq 1$.

B.7 Extended Kalman Filter for Amplitude and Phase Estimation

Note: We follow a slightly different convention here than in Chapter 3. Both approaches are equivalent and readily interchangeable.

Once the optimal measurement basis is fixed (using the commuting real quadrature vectors $\hat{v}(\hat{\phi})$ and $\hat{w}(\hat{\phi})$ defined in the previous sections), we can treat the measurement outcomes as noisy observations of a nonlinear function of the signal parameters and local oscillator phase. In this section, we develop an Extended Kalman Filter (EKF) to estimate the signal amplitude $|h|$ and phase ϕ from the joint quadrature measurements.

We assume the signal is stationary or slowly varying over the measurement interval, so that $|h|$ and ϕ can be treated as approximately constant (this framework can be generalized to dynamically evolving signals). The two commuting quadratures observables $\hat{y}_{\mathrm{opt}}$ and $\hat{y}_\perp$ (aligned along $v(\hat{\phi})$ and $w(\hat{\phi})$, respectively) provide simultaneous measurements in each frequency mode. Here $\hat{\phi}$ is the current best estimate for the signal's phase.

Nonlinear Measurement Model

Physically, $\hat{y}_{\mathrm{opt}}$ is the quadrature projection aligned with the expected signal phase, capturing primarily the amplitude information, while $\hat{y}_\perp$ is the conjugate quadrature (orthogonal in the four-dimensional quadrature space) that captures any residual signal due to phase mismatch.

Using the notation established earlier, let R_{tot} denotes the total signal response magnitude in the $v(\hat{\phi})$ direction, and M denotes the corresponding normalized response in the orthogonal direction $w(\hat{\phi})$. The nonlinear measurement function can then be written as:

$$\mathbf{y} = \begin{pmatrix} y_{\text{opt}} \\ y_{\perp} \end{pmatrix} = \sqrt{T}|h| \begin{pmatrix} R_{\text{tot}} \cos(\hat{\phi} - \phi) \\ M \sin(\hat{\phi} - \phi) \end{pmatrix} + \mathbf{n}, \tag{B.47}$$

where $M = \frac{R_1^2 - R_2^2 + I_1^2 - I_2^2}{R_{tot}}$, T is the integration time per time step used in the measurement, and $\mathbf{n}$ is the additive Gaussian noise vector. In our shot-noise-limited scenario, we assume $\mathbf{n}$ has zero mean and covariance $R = \frac{1}{2}I$.

When the local oscillator or quadrature basis is perfectly aligned with the signal ($\hat{\phi} = \phi$, so $\Delta\phi = 0$), we have $\cos(\Delta\phi) = 1$ and $\sin(\Delta\phi) = 0$, which means y_{opt} captures the full signal $|h|$ (scaled by $\sqrt{T}R_{\text{tot}}$) while $y_{\perp}$ carries no signal (only noise). If there is a phase error, however, some fraction of the signal leaks into the $y_{\perp}$ measurement: y_{opt} is reduced by the factor $\cos(\Delta\phi)$ and $y \perp$ acquires a signal component $|h| \sin(\Delta\phi)$. By processing y_{opt} and $y_{\perp}$ together we can simultaneously adjust our estimates of $|h|$ and ϕ.

The factors R_{tot} and M account for the frequency-domain response of the interferometer in the chosen quadrature basis, and are known constants from the signal model.

Linearization and Jacobian of the Measurement Function

To apply the EKF [87], we treat the unknown state vector as

$$\mathbf{x} = \begin{pmatrix} |h| \\ \Delta\phi \end{pmatrix}. \tag{B.48}$$

where $\Delta\phi = \hat{\phi} - \phi$. An estimated phase $\hat{\phi}$ is chosen (from a prior coarse measurement) and subsequently $\hat{\phi}$ will be updated as our estimate of ϕ improves.

For our prediction step, we assume a stationary signal; therefore:

$$\mathbf{x}_{k+1|k} = \mathbf{x}_k + \mathbf{w}_k, \tag{B.49}$$

with $\mathbf{w}_k$ being process noise. For a strictly constant signal we set $\mathbf{w}_k = \mathbf{0}$ (no process noise), and more generally $\mathbf{w}_k$ can capture any slow drift or uncertainty in the signal's evolution if needed. In the following we proceed with the assumption of no process noise, so the state is unchanged in prediction steps.

The measurement model can be written compactly as $\mathbf{y} = h(\mathbf{x}) + \mathbf{n}$, where $h(\mathbf{x})$ is the nonlinear vector-valued function given by:

$$h(\mathbf{x}) = \begin{pmatrix} \sqrt{T}|h|R_{\text{tot}}\cos(\Delta\phi) \\ \sqrt{T}|h|M\sin(\Delta\phi) \end{pmatrix}, \tag{B.50}$$

In order to use the Kalman filter framework, we linearize this function about the current estimate. That is, at each update we compute the Jacobian matrix of partial derivatives of $h(\mathbf{x})$ with respect to the state variables. The Jacobian H is a 2×2 matrix (since we have two measurement outputs and two state parameters) given by:

$$H(\mathbf{x}) = \left.\frac{\partial h(\mathbf{x})}{\partial \mathbf{x}}\right|_{\mathbf{x}=\hat{\mathbf{x}}} = \begin{pmatrix} \frac{\partial y_{\text{opt}}}{\partial |h|} & \frac{\partial y_{\text{opt}}}{\partial(\Delta\phi)} \\ \frac{\partial y_{\perp}}{\partial |h|} & \frac{\partial y_{\perp}}{\partial(\Delta\phi)} \end{pmatrix}_{\mathbf{x}=\hat{\mathbf{x}}}, \tag{B.51}$$

evaluated at the current a priori state estimate $\hat{\mathbf{x}}$ (before the measurement update). Computing these derivatives from the above $h(x)$, we obtain:

- For the y_{opt} measurement function $h_1(x) = \sqrt{T}|h|R_{\text{tot}}\cos(\Delta\phi)$:

$$\frac{\partial h_1}{\partial |h|} = \sqrt{T}R_{\text{tot}}\cos(\Delta\phi), \quad \frac{\partial h_1}{\partial \Delta\phi} = -\sqrt{T}|h|R_{\text{tot}}\sin(\Delta\phi). \tag{B.52}$$

- For the $y_{\perp}$ measurement function $h_2(x) = \sqrt{T}|h|M\sin(\Delta\phi)$:

$$\frac{\partial h_2}{\partial |h|} = \sqrt{T}M\sin(\Delta\phi), \quad \frac{\partial h_2}{\partial \Delta\phi} = \sqrt{T}|h|M\cos(\Delta\phi). \tag{B.53}$$

Putting these together, the Jacobian matrix is:

$$H(\hat{\mathbf{x}}) = \begin{pmatrix} \sqrt{T}R_{\text{tot}}\cos(\widehat{\Delta\phi}) & -\sqrt{T}|\hat{h}|R_{\text{tot}}\sin(\widehat{\Delta\phi}) \\ \sqrt{T}M\sin(\widehat{\Delta\phi}) & \sqrt{T}|\hat{h}|M\cos(\widehat{\Delta\phi}) \end{pmatrix}, \tag{B.54}$$

where $|\hat{h}|$ and $\widehat{\Delta\phi}$ are the current predicted values for the amplitude and phase error, respectively. This linearization $h(\mathbf{x}) \approx h(\hat{\mathbf{x}}) + H(\hat{\mathbf{x}})(\mathbf{x} - \hat{\mathbf{x}})$ allows the EKF to update the state as if the measurement response were locally linear around the estimate.

Notice here that H depends on the current estimate of the signal. For instance, $\frac{\partial y_{\text{opt}}}{\partial(\Delta\phi)} = -\sqrt{T}|h|R_{\text{tot}}\sin(\Delta\phi)$ is zero when $\Delta\phi = 0$ (i.e., when we believe we are perfectly aligned with the signal phase, small changes in phase estimate have no first-order effect on y_{opt}). Conversely, if $\Delta\phi$ is nonzero, this derivative is nonzero, indicating that a small change in the phase estimate will significantly change the expected y_{opt}.

Similarly, $\partial y_\perp / \partial(\Delta\phi)$ is proportional to $\cos(\Delta\phi)$, which is highest when $\Delta\phi = 0$ (meaning $y_\perp$ is most sensitive to phase when we are nearly aligned with the signal, as expected since at true alignment $y_\perp$ should be zero and any slight phase error will create a linear change in $y_\perp$).

Finally, as our quadtrature measurment is always updated to reflect our best estimate of the state, we have

$$H(\hat{\mathbf{x}}) = \begin{pmatrix} \sqrt{T} R_{\text{tot}} & 0 \\ 0 & \sqrt{T}|\hat{h}| M \end{pmatrix}. \tag{B.55}$$

Next, we formalize the EKF update steps using this linearization.

EKF Update Equations and Algorithm

The Extended Kalman Filter proceeds in predict-update cycles. At each frequency bin (or each measurement time step), we first predict the state and covariance, then incorporate the new measurement $(y_{\text{opt}}, y_\perp)$ to correct the estimates. In our setting, since the state is assumed constant, the prediction step simply carries forward the previous estimate. The measurement update step then refines the estimate based on the observed quadrature outcomes. The full EKF algorithm in this context is as follows:

1. **Initialization:** Before processing any optimal-basis measurement, an initial estimate for the state $\hat{\mathbf{x}}_0 = [|\hat{h}|_0; \widehat{\Delta\phi}_0]^T$ is chosen via heterodyne measurement, along with an initial error covariance P_0. Detailed forms of these estimates can be found in Sec. B.3.

2. **Prediction (Time Update):** For each new time step (indexed by $k+1$, following k measurments), we propagate the state and covariance forward according to the process model. In our static model, this means:

$$\hat{\mathbf{x}}_{k+1|k} = \hat{\mathbf{x}}_k, \tag{B.56}$$

$$P_{k+1|k} = P_k. \tag{B.57}$$

   $\hat{\mathbf{x}}_{k+1|k} = [|\hat{h}|_{k+1|k}, \widehat{\Delta\phi}_{k+1|k}]^T$ is thus our a priori estimate before seeing any new data.

3. **Measurement Prediction:** Using the nonlinear model, we predict the expected measurement outcomes based on the current predicted state. We plug

$\hat{\mathbf{x}}_{k+1|k}$ into the measurement function:

$$\hat{\mathbf{y}}_{k+1|k} = h(\hat{\mathbf{x}}_{k+1|k}) = \begin{pmatrix} \sqrt{T}|\hat{h}|_{k+1|k} R_{\text{tot}} \cos(\widehat{\Delta\phi}_{k+1|k}) \\ \sqrt{T}|\hat{h}|_{k+1|k} M \sin(\widehat{\Delta\phi}_{k+1|k}) \end{pmatrix} = \begin{pmatrix} \sqrt{T}|\hat{h}|_{k+1|k} R_{\text{tot}} \\ 0 \end{pmatrix}, \tag{B.58}$$

where we have used the fact that we set the interferometer's local oscillator phase or quadrature basis to $\hat{\phi}_{k+1|k}$. This gives the predicted values $\hat{y}_{\text{opt}}$ and $\hat{y}_{\perp}$ prior to the new measurement, based on our current guesses of $|h|$ and ϕ.

4. **Obtain New Measurement:** We then collect the new actual measurement $\mathbf{z}_{k+1} = [y_{\text{opt},k+1}; y_{\perp,k+1}]^T$ by performing the optimal quadrature (and its commutating pair) readout at this step. This $\mathbf{z}_{k+1}$ is a random Gaussian vector with mean $h([|\hat{h}|_{true}, \widehat{\phi}_{k+1|k} - \phi_{true}]^T)$ and covariance R.

5. **Innovation (Residual) Computation:** Compute the innovation $\mathbf{r}_{k+1}$, which is the difference between the actual measurement and the predicted measurement:

$$\mathbf{r}_{k+1} = \mathbf{z}_{k+1} - \hat{\mathbf{y}}_{k+1|k}. \tag{B.59}$$

This 2×1 vector represents the new information provided by the measurement — if our predictions were perfect, $\mathbf{r}_{k+1}$ would be zero-mean noise; any systematic deviation indicates a discrepancy between the current state estimate and the true signal.

6. **Kalman Gain Calculation:** We linearize the measurement model about $\hat{\mathbf{x}}_{k+1|k}$ by computing the Jacobian $H_{k+1} = H(\hat{\mathbf{x}}_{k+1|k})$ as described above. We can then compute the Kalman gain matrix K_{k+1}, which weighs how the innovation should be mapped into state corrections:

$$K_{k+1} = P_{k+1|k} H_{k+1}^T (H_{k+1} P_{k+1|k} H_{k+1}^T + R)^{-1}. \tag{B.60}$$

Here $H_{k+1} P_{k+1|k} H_{k+1}^T + R$ is the 2×2 innovation covariance matrix, combining the predicted state uncertainty projected into measurement space and the intrinsic measurement noise. The gain K_{k+1} (a 2×2 matrix) tells us how strongly to trust the new measurement relative to the prior: if the measurement noise is small or our prior uncertainty is large, K_{k+1} will have larger values (giving more weight to the innovation), whereas if the state was already known very precisely or measurement is noisy, K_{k+1} will be smaller.

7. **State Update:** We update the state estimate by applying the innovation weighted by the Kalman gain:

$$\hat{\mathbf{x}}_{k+1|k+1} = \hat{\mathbf{x}}_{k+1|k} + K_{k+1}\mathbf{r}_{k+1}. \tag{B.61}$$

This produces the a posteriori estimate $\hat{\mathbf{x}}_{k+1|k+1} = [|\hat{h}|_{k+1|k+1}; \widehat{\Delta\phi}_{k+1|k+1}]^T$ after incorporating the measurement at step $k+1$.

The off-diagonal terms of K_{k+1} allow each measurement channel to adjust both state variables. For example, if the $y_\perp$ measurement in z_{k+1} came out higher than expected (positive innovation in $y_\perp$), this indicates the phase estimate $\hat{\phi}$ was likely too far ahead of the true phase (so ϕ was actually larger, making $\hat{\phi} - \phi$ too negative and thus $\sin(\Delta\phi)$ was underestimated). The Kalman gain will translate this residual into a reduction of $\widehat{\Delta\phi}$ (i.e., an increase in the estimated true phase ϕ) to better align with the signal. At the same time, a large $|y_\perp|$ might also slightly adjust the amplitude if the filter infers that some signal power in $y_\perp$ means the amplitude could be larger. Similarly, a discrepancy in y_{opt} predominantly corrects the amplitude estimate, but can also tweak the phase. In practice, because we chose an optimal basis, the y_{opt} channel has a much stronger dependence on $|h|$ and the $y_\perp$ channel on ϕ, and the Kalman gain matrix will reflect that.

After this state correction, we update the measurement phase by setting $\hat{\phi} = \hat{\phi}_{k+1|k+1}$ (the new phase estimate) as the basis for the next measurement, thereby keeping $\widehat{\Delta\phi} = 0$. In our formulation, $\widehat{\Delta\phi}_{k+1|k+1}$ represents the remaining phase error after update; we expect the EKF to drive this toward zero mean as it converges.

8. **Covariance Update:** We update the state covariance to reflect the reduced uncertainty after incorporating the measurement:

$$P_{k+1|k+1} = (I - K_{k+1}H_{k+1})P_{k+1|k}(I - K_{k+1}H_{k+1})^T + K_{k+1}RK_{k+1}^T. \tag{B.62}$$

This update produces the new covariance $P_{k+1|k+1}$, which will typically be smaller than $P_{k+1|k}$, reflecting the gained information. For example, the variance in ϕ (second diagonal element of P) will drop as successive $y_\perp$ measurements pin down the phase, and the variance in $|h|$ will drop as y_{opt} homes in on the amplitude.

9. **Iterate:** Finally, we Set $k+1 \to k+2$ and repeat. Each new time step is processed in the same way, continually refining the estimates. In the end, after

processing all available data, we obtain a final estimate $|\hat{h}|$ and $\hat{\phi}$ along with their covariance matrix P, which quantifies the estimation uncertainty.

B.8 Unscented Kalman Filter for Amplitude and Phase Estimation

While the Extended Kalman Filter linearizes the nonlinear measurement function via its Jacobian, the Unscented Kalman Filter (UKF) instead captures the effects of nonlinearity by propagating a carefully chosen set of "sigma points" through the exact nonlinear mapping [78]. This approach can yield better performance when the measurement model is strongly nonlinear. Empirically, we learn that UKFs tend to perform well when the parameter distributions are unimodal, which is the case for our system.

State and Measurement Model

We again take as our state vector at discrete time k

$$\mathbf{x}_k = \begin{pmatrix} |h|_k \\ \Delta\phi_k \end{pmatrix}, \quad \Delta\phi_k \equiv \hat{\phi}_k - \phi, \tag{B.63}$$

and

$$\mathbf{x}_{k+1|k} = \mathbf{x}_k. \tag{B.64}$$

The measurement function is identical to that in the EKF:

$$\mathbf{y}_{k+1|k} = h(\mathbf{x}_{k+1|k}) + \mathbf{n}_{k+1}, \qquad h(\mathbf{x}) = \sqrt{T}\big|h\big|_{k+1|k} \begin{pmatrix} R_{tot}\cos(\Delta\phi_{k+1|k}) \\ M\sin(\Delta\phi_{k+1|k}) \end{pmatrix}, \tag{B.65}$$

with zero-mean Gaussian noise $\mathbf{n}_{k+1} \sim \mathcal{N}(0, \frac{1}{2}I)$.

Unscented Transform and Sigma-Point Generation

The core idea of the UKF is to represent the posterior distribution of the state by a small set of deterministically chosen "sigma points" that capture the first two moments of the state estimate upto the third order. For an n-dimensional state (here $n = 2$), we form $2n + 1 = 5$ sigma points $\{\chi^{(i)}_{k+1|k}\}_{i=0}^{2n}$ around the current a priori mean $\hat{\mathbf{x}}_{k+1|k}$ and covariance $P_{k+1|k}$:

$$\begin{aligned} \chi^{(0)}_{k+1|k} &= \hat{\mathbf{x}}_{k+1|k}, \\ \chi^{(i)}_{k+1|k} &= \hat{\mathbf{x}}_{k+1|k} + \Big[\sqrt{(n+\lambda)P_{k+1|k}}\Big]_i, \quad i = 1, \ldots, n, \\ \chi^{(i+n)}_{k+1|k} &= \hat{\mathbf{x}}_{k+1|k} - \Big[\sqrt{(n+\lambda)P_{k+1|k}}\Big]_i, \quad i = 1, \ldots, n. \end{aligned} \tag{B.66}$$

Here, $\lambda = \alpha^2(n+\kappa) - n$ sets the spread of the sigma points, and $[\sqrt{(n+\lambda)P}]_i$ denotes the i-th row of the matrix square-root. Typical choices for the UKF parameters are $\alpha \approx 10^{-3}$, $\kappa = 0$, and $\beta = 2$.

Each sigma point also carries its associated weights to calculate the mean and covariance:

$$\begin{aligned} W_m^{(0)} &= \frac{\lambda}{n+\lambda}, & W_c^{(0)} &= \frac{\lambda}{n+\lambda} + (1 - \alpha^2 + \beta), \\ W_m^{(i)} &= W_c^{(i)} = \frac{1}{2(n+\lambda)}, & & i = 1, \ldots, 2n. \end{aligned} \tag{B.67}$$

Prediction Step

Because our process model is simply identity plus noise, the sigma points propagate unchanged:

$$\chi_{k+1|k}^{(i)} = \chi_{k+1|k}^{(i)}, \quad i = 0, \ldots, 2n. \tag{B.68}$$

The predicted state mean and covariance are then reconstructed by weighted sums:

$$\bar{\mathbf{x}}_{k+1|k} = \sum_{i=0}^{2n} W_m^{(i)} \chi_{k+1|k}^{(i)}, \qquad P_{k+1|k} = \sum_{i=0}^{2n} W_c^{(i)} \left[\chi_{k+1|k}^{(i)} - \bar{\mathbf{x}}_{k+1|k}\right] \left[\chi_{k+1|k}^{(i)} - \bar{\mathbf{x}}_{k+1|k}\right]^T. \tag{B.69}$$

Measurement Update

Sigma-Point Mapping Through the Nonlinear Measurement. Each predicted sigma point is mapped through the exact nonlinear function $h(\cdot)$:

$$\gamma_{k+1|k}^{(i)} = h\big(\chi_{k+1|k}^{(i)}\big), \quad i = 0, \ldots, 2n. \tag{B.70}$$

This yields a set of $2n + 1$ predicted measurement sigma points.

Measurement Mean and Covariance. From these the predicted measurement mean and covariance follow:

$$\bar{\mathbf{y}}_{k+1|k} = \sum_{i=0}^{2n} W_m^{(i)} \gamma_{k+1|k}^{(i)}, \qquad S_{k+1} = \sum_{i=0}^{2n} W_c^{(i)} \left[\gamma_{k+1|k}^{(i)} - \bar{\mathbf{y}}_{k+1|k}\right] \left[\gamma_{k+1|k}^{(i)} - \bar{\mathbf{y}}_{k+1|k}\right]^T + R, \tag{B.71}$$

where $R = \frac{1}{2} I$ is the measurement-noise covariance.

Cross-Covariance and Kalman Gain. We then form the cross-covariance between state and measurement:

$$P_{xy} = \sum_{i=0}^{2n} W_c^{(i)} \left[\chi_{k+1|k}^{(i)} - \hat{\mathbf{x}}_{k+1|k}\right] \left[\gamma_{k+1|k}^{(i)} - \hat{\mathbf{y}}_{k+1|k}\right]^T. \tag{B.72}$$

The Unscented Kalman gain is then given by,

$$K_{k+1} = P_{xy} S_{k+1}^{-1}. \tag{B.73}$$

State and Covariance Correction. Given the actual measurement

$$\mathbf{z}_{k+1} = (y_{opt,k+1}, y_{\perp,k+1})^T, \tag{B.74}$$

we compute the innovation

$$\mathbf{r}_{k+1} = \mathbf{z}_{k+1} - \hat{\mathbf{y}}_{k+1|k}, \tag{B.75}$$

and apply the standard UKF update:

$$\hat{\mathbf{x}}_{k+1|k+1} = \hat{\mathbf{x}}_{k+1|k} + K_{k+1}\mathbf{r}_{k+1}, \quad P_{k+1|k+1} = P_{k+1|k} - K_{k+1} S_{k+1} K_{k+1}^T. \tag{B.76}$$

Finally, we set the new measurement basis phase so that the quadrature basis for the next step remains aligned with the updated phase estimate.

Benefits of UKF

- **Second Order Effects:** By pushing the sigma points through the full nonlinear mapping, the UKF captures curvature (second-order effects) that the EKF's first-order Taylor approximation may miss. This can improve convergence when the phase error $\Delta\phi$ is larger than what EKFs can usually handle.
- **Robustness to Initialization:** The UKF's deterministic sampling often handles poor initial guesses more gracefully, since the sigma points explore the local state distribution around the mean without requiring an explicit Jacobian.
- **Computational Cost:** For our two-dimensional state, the UKF suggests propagating only five sigma points per step, which remains computationally efficient for real-time implementation.

B.9 Particle Filtering

Bayesian Recursive Filtering

In the Bayesian paradigm, we seek the posterior density

$$p(\mathbf{x}_k \mid \mathbf{y}_{1:k}) \tag{B.77}$$

of the hidden state $\mathbf{x}_k$ (here $|h|$ and ϕ) given all measurements up to time k. This is computed recursively by alternately predicting the state via

$$p(\mathbf{x}_k \mid \mathbf{y}_{1:k-1}) = \int p(\mathbf{x}_k \mid \mathbf{x}_{k-1}) p(\mathbf{x}_{k-1} \mid \mathbf{y}_{1:k-1}) d\mathbf{x}_{k-1}, \tag{B.78}$$

and then updating with the new measurement $\mathbf{y}_k$ via Bayes' rule:

$$p(\mathbf{x}_k \mid \mathbf{y}_{1:k}) \propto p(\mathbf{y}_k \mid \mathbf{x}_k) p(\mathbf{x}_k \mid \mathbf{y}_{1:k-1}). \tag{B.79}$$

Particle Filter

A particle filter approximates the posterior distribution described above by a weighted ensemble of N "particles":

$$p(\mathbf{x}_k \mid \mathbf{y}_{1:k}) \approx \sum_{i=1}^{N} w_k^{(i)} \delta\big(\mathbf{x}_k - \mathbf{x}_k^{(i)}\big), \tag{B.80}$$

where $\{\mathbf{x}_k^{(i)}, w_k^{(i)}\}_{i=1}^N$ are the particles and weights, and $\delta(\cdot)$ is the Dirac-delta. Unlike Kalman filters — which assume Gaussian posteriors — the particle filter can represent arbitrary, even multimodal, distributions.

Algorithm Steps

1. **Initialization:** We draw initial particles $\{\mathbf{x}_0^{(i)}\}$ from the prior using a heterodyne measurement and simulate particles using the variance for the measurements. All weights are initially set at $w_0^{(i)} = 1/N$.

2. **Weight Update:** Upon receiving measurement $\mathbf{y}_{k+1} = (y_{opt}, y_\perp)^T$, we compute the likelihood

$$p(\mathbf{y}_{k+1} \mid \mathbf{x}_{k+1}^{(i)}) = \frac{1}{2\pi\sqrt{\det R}} \exp\Big[-\tfrac{1}{2}\big(\mathbf{y}_{k+1} - h(\mathbf{x}_{k+1}^{(i)})\big)^T R^{-1} \big(\mathbf{y}_{k+1} - h(\mathbf{x}_{k+1}^{(i)})\big)\Big], \tag{B.81}$$

   with $R = \frac{1}{2} I$ and

$$h(\mathbf{x}_{k+1}^{(i)}) = \begin{pmatrix} \sqrt{T}|\hat{h}|_{k+1}^{(i)} R_{tot} \\ 0 \end{pmatrix}. \tag{B.82}$$

   The weights are updated as,

$$w_{k+1}^{(i)} \propto w_k^{(i)} p(\mathbf{y}_k \mid \mathbf{x}_k^{(i)}), \tag{B.83}$$

   and then normalized so that $\sum_i w_k^{(i)} = 1$.

3. **State Estimate:** The posterior mean is then given by

$$\hat{\mathbf{x}}_k = \sum_{i=1}^{N} w_k^{(i)} \mathbf{x}_k^{(i)}, \tag{B.84}$$

   and covariance as needed.

4. **Iterate:** We repeat this process by setting $k+1 \rightarrow k+2$.

The particle filter makes no Gaussian assumption, so it can capture multimodality and strong nonlinearity. It serves as an optimal filtering benchmark, i.e., if an EKF or UKF matches the particle-filter performance, the Gaussian-linear approximations are justified.

Bibliography

[1] J. Aasi *et al.* (LIGO Scientific Collaboration). Advanced Ligo. *Classical and Quantum Gravity*, 32(7):074001, Mar 2015. doi: 10.1088/0264-9381/32/7/074001.

[2] J. Hough, S. Rowan, and B. S. Sathyaprakash. The Search for Gravitational Waves. *Journal of Physics B: Atomic, Molecular and Optical Physics*, 38(9): S497, Apr 2005. doi: 10.1088/0953-4075/38/9/004.

[3] R. A. Hulse and J. H. Taylor. Discovery of a Pulsar in a Binary System. *The Astrophysical Journal Letters*, 195:L51–L53, Jan 1975. doi: 10.1086/181708.

[4] B. P. Abbott *et al.* (LIGO Scientific Collaboration and Virgo Collaboration). Observation of Gravitational Waves from a Binary Black Hole Merger. *Physical Review Letters*, 116:061102, Feb 2016. doi: 10.1103/PhysRevLett.116.061102.

[5] B. P. Abbott *et al.* (LIGO Scientific Collaboration and Virgo Collaboration). GW170817: Observation of Gravitational Waves from a Binary Neutron Star Inspiral. *Physical Review Letters*, 119:161101, Oct 2017. doi: 10.1103/PhysRevLett.119.161101.

[6] B. P. Abbott *et al.* (LIGO Scientific Collaboration and Virgo Collaboration). Search for Post-merger Gravitational Waves from the Remnant of the Binary Neutron Star Merger GW170817. *The Astrophysical Journal Letters*, 851(1): L16, Dec 2017. doi: 10.3847/2041-8213/aa9a35.

[7] B. P. Abbott *et al.* (LIGO Scientific Collaboration and Virgo Collaboration). GWTC-1: A Gravitational-Wave Transient Catalog of Compact Binary Mergers Observed by LIGO and Virgo during the First and Second Observing Runs. *Physical Review X*, 9:031040, Sep 2019. doi: 10.1103/PhysRevX.9.031040.

[8] B. P. Abbott *et al.* (LIGO Scientific Collaboration and Virgo Collaboration). Search for Gravitational Waves from a Long-lived Remnant of the Binary Neutron Star Merger GW170817. *The Astrophysical Journal*, 875(2):160, Apr 2019. doi: 10.3847/1538-4357/ab0f3d.

[9] R. Abbott *et al.* (LIGO Scientific Collaboration and Virgo Collaboration). GWTC-2: Compact Binary Coalescences Observed by LIGO and Virgo during the First Half of the Third Observing Run,. *Physical Review X*, 11:021053, Jun 2021. doi: 10.1103/PhysRevX.11.021053.

[10] F. Acernese *et al.* (Virgo Collaboration). Advanced Virgo: A Second-Generation Interferometric Gravitational Wave Detector. *Classical and Quantum Gravity*, 32(2):024001, Dec 2014. doi: 10.1088/0264-9381/32/2/024001.

[11] K. Somiya (for the KAGRA Collaboration). Detector Configuration of KAGRA–the Japanese Cryogenic Gravitational-Wave Detector. *Classical and Quantum Gravity*, 29(12):124007, Jun 2012. doi: 10.1088/0264-9381/29/12/124007.

[12] M. Pitkin, S. Reid, S. Rowan, and J. Hough. Gravitational Wave Detection by Interferometry (Ground and Space). *Living Reviews in Relativity*, 14(1), Jul 2011. doi: 10.12942/lrr-2011-5.

[13] V. Giovannetti, S. Lloyd, and L. Maccone. Quantum-Enhanced Measurements: Beating the Standard Quantum Limit. *Science*, 306(5700):1330–1336, Nov 2004. doi: 10.1126/science.1104149.

[14] C. M. Caves. Quantum-Mechanical Noise in an Interferometer. *Physical Review D*, 23:1693–1708, Apr 1981. doi: 10.1103/PhysRevD.23.1693.

[15] Stefan L. Danilishin and Farid Ya. Khalili. Quantum Measurement Theory in Gravitational-Wave Detectors. *Living Reviews in Relativity*, 15(1), Apr 2012. doi: 10.12942/lrr-2012-5.

[16] M. Tse *et al.* Quantum-Enhanced Advanced LIGO Detectors in the Era of Gravitational-Wave Astronomy. *Physical Review Letters*, 123:231107, Dec 2019. doi: 10.1103/PhysRevLett.123.231107.

[17] M. Tse *et al.* The Einstein Telescope: A Third-Generation Gravitational Wave Observatory. *Classical and Quantum Gravity*, 27(19):194002, Sep 2010. doi: 10.1088/0264-9381/27/19/194002.

[18] K. McKenzie, M. B. Gray, P. K. Lam, and D. E. McClelland. Technical Limitations to Homodyne Detection at Audio Frequencies. *Applied Optics*, 46 (17):3389–3395, Jun 2007. doi: 10.1364/AO.46.003389.

[19] Y. Levin. Internal Thermal Noise in the LIGO Test Masses: A Direct Approach. *Physical Review D*, 57:659–663, Jan 1998. doi: 10.1103/PhysRevD.57.659.

[20] P. R. Saulson. Terrestrial Gravitational Noise on a Gravitational Wave Antenna. *Physical Review D*, 30:732–736, Aug 1984. doi: 10.1103/PhysRevD.30.732.

[21] S. A. Hughes and K. S. Thorne. Seismic Gravity-Gradient Noise in Interferometric Gravitational-Wave Detectors. *Physical Review D*, 58:122002, Nov 1998. doi: 10.1103/PhysRevD.58.122002.

[22] J. Harms. Terrestrial Gravity Fluctuations. *Living Reviews in Relativity*, 18: 1–150, Dec 2015. doi: 10.1007/lrr-2015-3.

[23] J. C. Driggers, J. Harms, and R. X. Adhikari. Subtraction of Newtonian Noise using Optimized Sensor Arrays. *Physical Review D*, 86:102001, Nov 2012. doi: 10.1103/PhysRevD.86.102001.

[24] S. Kawamura and Y. Chen. Displacement-Noise-Free Gravitational-Wave Detection. *Physical Review Letters*, 93:211103, Nov 2004. doi: 10.1103/PhysRevLett.93.211103.

[25] Y. Chen, A. Pai, K. Somiya, S. Kawamura, S. Sato, K. Kokeyama, R. L. Ward, K. Goda, and E. E. Mikhailov. Interferometers for Displacement-Noise-Free Gravitational-Wave Detection. *Physical Review Letters*, 97:151103, Oct 2006. doi: 10.1103/PhysRevLett.97.151103.

[26] M. Tinto and S. V. Dhurandhar. Time-Delay Interferometry. *Living Reviews in Relativity*, 24, Dec 2020. doi: 10.1007/s41114-020-00029-6.

[27] H. J. Paik, C. E. Griggs, M. V. Moody, K. Venkateswara, H. M. Lee, A. B. Nielsen, E. Majorana, and J. Harms. Low-Frequency Terrestrial Tensor Gravitational-Wave Detector. *Classical and Quantum Gravity*, 33(7):075003, Mar 2016. doi: 10.1088/0264-9381/33/7/075003.

[28] L. S. Finn and S. Mukherjee. Data Conditioning for Gravitational Wave Detectors: A Kalman Filter for Regressing Suspension Violin Modes. *Physical Review D*, 63:062004, Feb 2001. doi: 10.1103/PhysRevD.63.062004.

[29] L. Wang, F. Xie, Y. Zhang, M. Xiao, and F. Liu. Adaptive Optical Phase Estimation for Real-Time Sensing of Fast-Varying Signals. *Scientific Reports*, 12:21745, Dec 2022. doi: 10.1038/s41598-022-26329-1.

[30] Y. Zhao, N. Aritomi, E. Capocasa, M. Leonardi, M. Eisenmann, Y. Guo, E. Polini, A. Tomura, K. Arai, Y. Aso, Y. C. Huang, R. K. Lee, H. Lück, O. Miyakawa, P. Prat, A. Shoda, M. Tacca, R. Takahashi, H. Vahlbruch, M. Vardaro, C. M. Wu, M. Barsuglia, and R. Flaminio. Frequency-Dependent Squeezed Vacuum Source for Broadband Quantum Noise Reduction in Advanced Gravitational-Wave Detectors. *Physical Review Letters*, 124:171101, Apr 2020. doi: 10.1103/PhysRevLett.124.171101.

[31] H. J. Kimble, Y. Levin, A. B. Matsko, K. S. Thorne, and S. P. Vyatchanin. Conversion of Conventional Gravitational-Wave Interferometers into Quantum Nondemolition Interferometers by Modifying their Input and/or Output Optics. *Physical Review D*, 65:022002, Dec 2001. doi: 10.1103/PhysRevD.65.022002.

[32] J. Abadie *et al.* (LIGO Scientific Collaboration). A Gravitational Wave Observatory Operating beyond the Quantum Shot-Noise Limit. *Nature Physics*, 7(12):962–965, Sep 2011. doi: 10.1038/nphys2083.

[33] M. Tsang, H. M. Wiseman, and C. M. Caves. Fundamental Quantum Limit to Waveform Estimation. *Physical Review Letters*, 106:090401, Mar 2011. doi: 10.1103/PhysRevLett.106.090401.

[34] R. Demkowicz-Dobrzański, K. Banaszek, and R. Schnabel. Fundamental Quantum Interferometry Bound for the Squeezed-Light-Enhanced Gravitational Wave Detector GEO 600. *Physical Review A*, 88:041802, Oct 2013. doi: 10.1103/PhysRevA.88.041802.

[35] M. D. Lang and C. M. Caves. Optimal Quantum-Enhanced Interferometry Using a Laser Power Source. *Physical Review Letters*, 111:173601, Oct 2013. doi: 10.1103/PhysRevLett.111.173601.

[36] H. Miao, R. X. Adhikari, Y. Ma, B. Pang, and Y. Chen. Towards the Fundamental Quantum Limit of Linear Measurements of Classical Signals. *Physical Review Letters*, 119:050801, Aug 2017. doi: 10.1103/PhysRevLett.119.050801.

[37] D. Branford, H. Miao, and A. Datta. Fundamental Quantum Limits of Multicarrier Optomechanical Sensors. *Physical Review Letters*, 121:110505, Sep 2018. doi: 10.1103/PhysRevLett.121.110505.

[38] J. B. Brask, R. Chaves, and J. Kołodyński. Improved Quantum Magnetometry beyond the Standard Quantum Limit. *Physical Review X*, 5:031010, Jul 2015. doi: 10.1103/PhysRevX.5.031010.

[39] T. Baumgratz and A. Datta. Quantum Enhanced Estimation of a Multidimensional Field. *Physical Review Letters*, 116:030801, Jan 2016. doi: 10.1103/PhysRevLett.116.030801.

[40] K. Macieszczak, M. Fraas, and R. Demkowicz-Dobrzański. Bayesian Quantum Frequency Estimation in Presence of Collective Dephasing. *New Journal of Physics*, 16(11):113002, Oct 2014. doi: 10.1088/1367-2630/16/11/113002.

[41] H. Katori. Optical Lattice Clocks and Quantum Metrology. *Nature Photonics*, 5(4):203–210, Mar 2011. doi: 10.1038/nphoton.2011.45.

[42] K. Chabuda, I. D. Leroux, and R. Demkowicz-Dobrzański. The Quantum Allan Variance. *New Journal of Physics*, 18(8):083035, Aug 2016. doi: 10.1088/1367-2630/18/8/083035.

[43] R. Kaubruegger, D. V. Vasilyev, M. Schulte, K. Hammerer, and P. Zoller. Quantum Variational Optimization of Ramsey Interferometry and Atomic Clocks. *Physical Review X*, 11:041045, Dec 2021. doi: 10.1103/PhysRevX.11.041045.

[44] S. Schmitt, T. Gefen, F. M. Stürner, T. Unden, G. Wolff, C. Müller, J. Scheuer, B. Naydenov, M. Markham, S. Pezzagna, J. Meijer, I. Schwarz, M. Plenio, A. Retzker, L. P. McGuinness, and F. Jelezko. Submillihertz Magnetic Spectroscopy Performed with a Nanoscale Quantum Sensor. *Science*, 356(6340): 832–837, May 2017. doi: 10.1126/science.aam5532.

[45] J. M. Boss, K. S. Cujia, J. Zopes, and C. L. Degen. Quantum Sensing with Arbitrary Frequency Resolution. *Science*, 356(6340):837–840, May 2017. doi: 10.1126/science.aam7009.

[46] N. Aharon, A. Rotem, L. P. McGuinness, F. Jelezko, A. Retzker, and Z. Ringel. NV Center based Nano-NMR Enhanced by Deep Learning. *Scientific Reports*, 9(1), Nov 2019. doi: 10.1038/s41598-019-54119-9.

[47] D. Cohen, T. Gefen, L. Ortiz, and A. Retzker. Achieving the Ultimate Precision Limit with a Weakly Interacting Quantum Probe. *npj Quantum Information*, 6 (1), Sep 2020. doi: 10.1038/s41534-020-00313-x.

[48] S. Schmitt, T. Gefen, D. Louzon, C. Osterkamp, N. Staudenmaier, J. Lang, M. Markham, A. Retzker, L. P. McGuinness, and F. Jelezko. Optimal Frequency Measurements with Quantum Probes. *npj Quantum Information*, 7(1): 55, Apr 2021. doi: 10.1038/s41534-021-00391-5.

[49] Virgo Collaboration R. Abbott *et al.* (LIGO Scientific Collaboration and KAGRA Collaboration). GWTC-3: Compact Binary Coalescences Observed by LIGO and Virgo during the Second Part of the Third Observing Run. *Physical Review X*, 13:041039, Dec 2023. doi: 10.1103/PhysRevX.13.041039.

[50] A. Buikema *et al.* (LIGO Scientific Collaboration). Sensitivity and Performance of the Advanced LIGO detectors in the Third Observing Run. *Physical Review D*, 102:062003, Sep 2020. doi: 10.1103/PhysRevD.102.062003.

[51] Y. Chen and S. Kawamura. Displacement- and Timing-Noise-Free Gravitational-Wave Detection. *Physical Review Letters*, 96:231102, Jun 2006. doi: 10.1103/PhysRevLett.96.231102.

[52] A. Nishizawa, S. Kawamura, and M. Sakagami. Resonant Speed Meter for Gravitational-Wave Detection. *Physical Review Letters*, 101:081101, Aug 2008. doi: 10.1103/PhysRevLett.101.081101.

[53] K. Kokeyama, S. Sato, A. Nishizawa, S. Kawamura, Y. Chen, and A. Sugamoto. Development of a Displacement- and Frequency-Noise-Free Interferometer in a 3D Configuration for Gravitational Wave Detection. *Physical Review Letters*, 103:171101, Oct 2009. doi: 10.1103/PhysRevLett.103.171101.

[54] Y. Wang, D. Keitel, S. Babak, A. Petiteau, M. Otto, S. Barke, F. Kawazoe, A. Khalaidovski, V. Müller, D. Schütze, H. Wittel, K. Danzmann, and B. F. Schutz. Octahedron Configuration for a Displacement Noise-Cancelling Gravitational Wave Detector in Space. *Physical Review D*, 88:104021, Nov 2013. doi: 10.1103/PhysRevD.88.104021.

[55] A. Nishizawa, S. Iwaguchi, Y. Chen, T. Morimoto, T. Ishikawa, B. Wu, I. Watanabe, Y. Kawasaki, R. Shimizu, H. Shimizu, M. Kitaguchi, Y. Michimura, and S. Kawamura. Neutron Displacement Noise-Free Interferometer for Gravitational-Wave Detection. *Physical Review D*, 105:124017, Jun 2022. doi: 10.1103/PhysRevD.105.124017.

[56] G. De Vine, B. Ware, K. McKenzie, R. E. Spero, W. M. Klipstein, and D. A. Shaddock. Experimental Demonstration of Time-Delay Interferometry for the Laser Interferometer Space Antenna. *Physical Review Letters*, 104:211103, May 2010. doi: 10.1103/PhysRevLett.104.211103.

[57] D. A. Shaddock, B. Ware, R. E. Spero, and M. Vallisneri. Postprocessed Time-Delay Interferometry for LISA. *Physical Review D*, 70:081101, Oct 2004. doi: 10.1103/PhysRevD.70.081101.

[58] C. M. Caves and B. L. Schumaker. New Formalism for Two-Photon Quantum Optics. I. Quadrature Phases and Squeezed States. *Physical Review A*, 31: 3068–3092, May 1985. doi: 10.1103/PhysRevA.31.3068.

[59] T. Corbitt, Y. Chen, and N. Mavalvala. Mathematical Framework for Simulation of Quantum Fields in Complex Interferometers using the Two-Photon Formalism. *Physical Review A*, 72:013818, Jul 2005. doi: 10.1103/PhysRevA.72.013818.

[60] T. M. Cover. *Elements of information theory*. John Wiley & Sons, 1999.

[61] J. Liu, H. Yuan, X. M. Lu, and X. Wang. Quantum Fisher Information Matrix and Multiparameter Estimation. *Journal of Physics A: Mathematical and Theoretical*, 53(2):023001, Dec 2019.

[62] P. Stoica and R. L. Moses. *Spectral Analysis of Signals*, volume 452. Pearson, 2005.

[63] R. Nichols, P. Liuzzo-Scorpo, P. A. Knott, and G. Adesso. Multiparameter Gaussian Quantum Metrology. *Physical Review A*, 98:012114, Jul 2018. doi: 10.1103/PhysRevA.98.012114.

[64] M. Gessner, A. Smerzi, and L. Pezzè. Multiparameter Squeezing for Optimal Quantum Enhancements in Sensor Networks. *Nature Communications*, 11(1): 1–9, Jul 2020. doi: 10.1038/s41467-020-17471-3.

[65] S. P. Vyatchanin and A. B. Matsko. Quantum Variational Measurements of Force and Compensation of the Nonlinear Backaction in an Interferometric Displacement Transducer. *Soviet Journal of Experimental and Theoretical Physics*, 83(4):690–696, 1996.

[66] P. R. Saulson. Thermal Noise in Mechanical Experiments. *Physical Review D*, 42:2437–2445, Oct 1990. doi: 10.1103/PhysRevD.42.2437.

[67] B. J. Meers. Recycling in Laser-Interferometric Gravitational-Wave Detectors. *Physical Review D*, 38:2317–2326, Oct 1988. doi: 10.1103/PhysRevD.38.2317.

[68] A. Buonanno and Y. Chen. Quantum Noise in Second Generation, Signal-Recycled Laser Interferometric Gravitational-Wave Detectors. *Physical Review D*, 64:042006, Jul 2001. doi: 10.1103/PhysRevD.64.042006.

[69] B. P. Abbott *et al.* (LIGO Scientific Collaboration and Virgo Collaboration). GW190521: A Binary Black Hole Merger with a Total Mass of 150 $M_{\odot}$. *Physical Review Letters*, 125:101102, Sep 2020. doi: 10.1103/PhysRevLett.125.101102.

[70] Tania Regimbau. The Astrophysical Gravitational Wave Stochastic Background. *Research in Astronomy and Astrophysics*, 11(4):369–390, Mar 2011. doi: 10.1088/1674-4527/11/4/001.

[71] C. W. Helstrom. *Quantum Detection and Estimation Theory*. Academic Press, 1976.

[72] A. S. Holevo. *Probabilistic and Statistical Aspects of Quantum Theory*. North-Holland, 1982.

[73] M. Hayashi. *Asymptotic Theory of Quantum Statistical Inference*. World Scientific, 2008.

[74] J. W. Gardner, T. Gefen, S. A. Haine, J. J. Hope, and Y. Chen. Achieving the Fundamental Quantum Limit of Linear Waveform Estimation. *Physical Review Letters*, 132:130801, Mar 2024. doi: 10.1103/PhysRevLett.132.130801.

[75] B. L. Schumaker and C. M. Caves. New Formalism for Two-Photon Quantum Optics. II. Mathematical Foundation and Compact Notation. *Physical Review A*, 31:3093–3111, May 1985. doi: 10.1103/PhysRevA.31.3093.

[76] A. A. Clerk, M. H. Devoret, S. M. Girvin, Florian Marquardt, and R. J. Schoelkopf. Introduction to Quantum Noise, Measurement, and Amplification. *Reviews of Modern Physics*, 82:1155–1208, Apr 2010. doi: 10.1103/RevModPhys.82.1155.

[77] S. J. Julier and J. K. Uhlmann. New Extension of the Kalman filter to Nonlinear Systems. In *Signal Processing, Sensor Fusion, and Target Recognition VI*, volume 3068, pages 182 – 193. International Society for Optics and Photonics, SPIE, 1997. doi: 10.1117/12.280797.

[78] E. Wan and R. van Der Merwe. The Unscented Kalman filter for Nonlinear Estimation. In *Proceedings of the IEEE 2000 Adaptive Systems for Signal Processing, Communications, and Control Symposium (Cat. No.00EX373)*, pages 153–158. IEEE, 2000. doi: 10.1109/ASSPCC.2000.882463.

[79] M.S. Arulampalam, S. Maskell, N. Gordon, and T. Clapp. A Tutorial on Particle Filters for Online Nonlinear/Non-Gaussian Bayesian Tracking. *IEEE Transactions on Signal Processing*, 50(2):174–188, Feb 2002. doi: 10.1109/78.978374.

[80] M. Shibata, K. Kyutoku, T. Yamamoto, and K. Taniguchi. Gravitational Waves from Black Hole-Neutron Star binaries: Classification of Waveforms. *Physical Review D*, 79:044030, Feb 2009. doi: 10.1103/PhysRevD.79.044030.

[81] Christian D Ott. The Gravitational-Wave Signature of Core-collapse Supernovae. *Classical and Quantum Gravity*, 26(6):063001, Feb 2009. doi: 10.1088/0264-9381/26/6/063001.

[82] C. Messenger, K. Takami, S. Gossan, L. Rezzolla, and B. S. Sathyaprakash. Source Redshifts from Gravitational-Wave Observations of Binary Neutron Star Mergers. *Physical Review X*, 4:041004, Oct 2014. doi: 10.1103/PhysRevX.4.041004.

[83] P. D. Lasky. Gravitational Waves from Neutron Stars: A Review. *Publications of the Astronomical Society of Australia*, 32, Sep 2015. doi: 10.1017/pasa.2015.35.

[84] L. Baiotti. Gravitational Waves from Neutron Star Mergers and their Relation to the Nuclear Equation of State. *Progress in Particle and Nuclear Physics*, 109:103714, Nov 2019. doi: 10.1016/j.ppnp.2019.103714.

[85] A. Bauswein, N. U. F. Bastian, D. B. Blaschke, K. Chatziioannou, J. A. Clark, T. Fischer, and M. Oertel. Identifying a First-Order Phase Transition in Neutron-Star Mergers through Gravitational Waves. *Physical Review Letters*, 122:061102, Feb 2019. doi: 10.1103/PhysRevLett.122.061102.

[86] N. Andersson. A Gravitational-Wave Perspective on Neutron-Star Seismology. *Universe*, 7(4), Apr 2021. doi: 10.3390/universe7040097.

[87] G. Welch and G. Bishop. *An Introduction to the Kalman filter*. University of North Carolina at Chapel Hill, 1995.